A Numerical Modelling Study of a Planar Holographic Antenna

by

Esther Ler-Yen Yu

A thesis submitted to the
Faculty of Graduate and Postdoctoral Studies
in partial fulfillment of the requirements for the degree of

Master of Applied Science
in Electrical & Computer Engineering

Ottawa-Carleton Institute for Electrical and Computer engineering
School of Information Technology and Engineering
Faculty of Engineering
University of Ottawa

April 2011

ABSTRACT

Planar holographic antennas composed of printed dipole or conducting ring elements offer the promise of both low-profile and freedom from the losses associated with conventional printed beamforming networks at Ka-band frequencies and above. While some advances have been made, the aperture efficiencies achieved thus far have been unexpectedly low. These antennas are electrically quite large and materially inhomogeneous, which has prevented their rigorous analysis using computational electromagnetic (CEM). In this thesis we use CEM to study their operation, and point to several (and possibly unavoidable) reasons for the above-mentioned low aperture efficiency.

Keywords: planar holographic antennas; computational electromagnetics

Abstract ……………………………………………………………………1

Acknowledgements………………………………………………………...6

CHAPTER 1 : INTRODUCTION …………………….……………………7

1.1 PRINTED HIGH GAIN MILLIMETREWAVE ANTENNAS
– NEEDS AND LIMITATIONS ……………………… …………………… …7

1.2 HOLOGRAPHICALLY-BASED ANTENNA DESIGNS ………………………………8

1.3 OVERVIEW OF THE THESIS ……………………………………………………..10

1.4 REFERENCES FOR CHAPTER 1 ………………………………………………...10

CHAPTER 2 : REVIEW OF HOLOGRAPHICALLY-BASED ANTENNAS ……12

2.1 INTRODUCTION ………………………………..……………………… 12

2.2 A BRIEF RE-EXAMINATION OF THE IDEALISED INTERFERENCE PATTERNS ….12

2.3 THE PLANAR HOLOGRAPHIC ANTENNA …………..……………………..16

2.4 EXISTING PLANAR HOLOGRAPHIC ANTENNAS …….………………………20

2.5 SELECTED HOLOGRAM AND YAGI-RADIATOR DESIGNS ……………………22

2.6 CONCLUDING REMARKS ……………………….………………………...28

2.7 REFERENCES FOR CHAPTER 2 ………………..…………………………..28

CHAPTER 3 : MODIFIED ARRAY THEORY MODEL OF THE PLANAR HOLOGRAPHIC ANTENNA ………………………………..… 32

3.1 INTRODUCTION ………………………………..………………………. 32

3.2 MODIFED ARRAY THEORY MODEL …………..…………………………32

3.2.1 Initial Remarks ……………………………………………………………32

3.2.2 Expressions for the Radiation Pattern ……………………………………………34

3.2.3 Expressions for the Directivity Pattern ……………………………………………35

3.3 DEFINITION OF THE NON-UNIFORMLY SPACED ARRAY OPTIMISATION PROBLEM ……………………………………………37

3.3.1 The Objective Function ……………………………………………………37

3.3.2 Starting Values of (x_n, y_n, z_n) for the Optimisation Problem ……………………37

3.3.3 Constraints for the Optimisation Problem ……………………………………38

3.3.4 Numerical Optimisation Routine ……………………………………………38

3.4 OUTCOMES OF THE ARRAY OPTIMISATION STUDY ……………………………41

3.4.1 Optimiser Starting Values ……………………………………………………41

3.4.2 Single-Layer Array ……………………………………………………………41

3.4.3 Double-Layer Array ……………………………………………………………44

3.5 CONCLUDING REMARKS ……………………………………………………49

3.6 REFERENCES FOR CHAPTER 3 ………………………………………………49

CHAPTER 4 : COMPUTATIONAL ELECTROMAGNETIC MODELLING OF THE PLANAR HOLOGRAPHIC ANTENNA ……………………50

4.1 INTRODUCTION ……………………………………………………………50

4.2 COMPUTATIONAL ELECTROMAGNETICS MODELS USED ………………………51

4.2.1 Essentials of the Method of Moments ………………………………………51

4.2.2 Essentials of the Finite-Difference Time-Domain Method ……………………55

4.3 VALIDATION OF THE MOMENT METHOD MODELLING FOR THE CLASS OF PROBLEM OF INTEREST ……………………………………………………62

4.3.1 Reasons for the Use of the Moment Method Modelling ………………………63

4.3.2 General Remarks on Modelling Using FEKO Version 5.5 ……………………63

4.3.3 Modelling of a Sectoral Horn Using FEKO ……………………………………63

4.3.4 Modelling of the Hologram Portions of the Planar Holographic Antenna ………65

4.3.5 Modelling of Yagi Feeds for the Planar Holographic Antenna …………………68

4.3.6 Modelling of Yagi-Fed Planar Holographic Antenna – No Substrate ……………72

4.3.7 Modelling of Yagi-Fed Planar Holographic Antenna – With Substrate …………75

4.4 VALIDATION OF THE FDTD MODELLING FOR THE CLASS OF PROBLEM OF INTEREST ……………………………………………………..77

4.4.1 Selection of Validation Problem ………………………………………………77

4.4.2 Details of Some EMPIRE™ (Release 5.4) Modelling Procedures………………77

4.4.3 Modelling Outcomes for the Validation Problem ………………………………79

4.4.4 Modelling Continuous Conducting Strips in EMPIRE ………………………..85

4.5 CONCLUDING REMARKS ……………………………………………………89

4.6 REFERENCES FOR CHAPTER 3 ………………………………………………90

CHAPTER 5 : NUMERICAL EXPERIMENTATION ON THE PLANAR HOLOGRAPHIC ANTENNA ……………………………………………….91

5.1 PRELIMINARY REMARKS…………………………………………………………91

5.2 *IN SITU* INTERFERENCE PATTERNS ………………………………………………91

5.2.1 Interference Patterns for Diamond Shaped Substrate …………………………91

5.2.2 Simulation Details Needed to Obtain the Interference Pattern Results …………96

5.2.3 Interference Patterns for Substrates with Different Boundary Shapes …………..97

5.3 TRANSMIT MODE ANALYSIS USING THE METHOD OF MOMENTS – THE FEED SPILLOVER PROBLEM ……………………………………………………99

5.3.1 The Feed Spillover Problem …………………………………………………99

5.3.2 Effect of the Separation Between the Hologram Layers ………………………106

5.3.3 Strip Dipoles Versus Continuous Conducting Strips …………………………107

5.4 TRANSMIT MODE ANALYSIS USING THE FDTD METHOD ……………………108

5.4.1 Immediate Goals ……………………………………………………………108

5.4.2 The Effect of the Location of the Printed Feed Relative to the Hologram………..110

5.4.3 The Effect of the Hologram Strip Width ………………………………………111

5.4.4 Utilisation of the *In Situ* Null Locations ……………………………………..111

5.4.5 The Effect of Connector and Mounting Blocks on the Radiation Pattern 112

5.5 RECEIVE MODE ANALYSIS 116

5.5.1 The Receive Mode Analysis Idea 116

5.5.2 Receive Mode Fields of a Planar Holographic Antenna 116

5.6 CONCLUSIONS 120

5.7 REFERENCES FOR CHAPTER 5 120

CHAPTER 6 : GENERAL CONCLUSIONS 122

Acknowledgements

I am very grateful for the guidance and support of my supervisor Dr. Derek McNamara, and indeed that of my fellow graduate students in the Antenna Group at the University of Ottawa, in particular Jason Desjardins, Patrick Pelland, E'qab Almajali and Hamad Alroughani. I have enjoyed working with them, and their insights and advice have been invaluable.

I would like to thank Mr. Michel Cuhaci, manager of the Advanced Antenna Technology Group at the Communications Research Centre (CRC) for the use of CRC fabrication and measurement facilities. In particular I am grateful to Mr. Soulideth Thirakoune for facilitating the fabrication and measurement of the Yagi antenna, and for his advice on the use of the FDTD simulation code. I thank Dr. Nicolas Gagnon for running some of my FDTD simulation files with increased mesh resolution.

And finally, I am thankful to my family, and my fiancé Gregory Sienkiewicz, for their words of encouragement and support over the last two years.

Publications

E.Yu et al., “Progress in Planar Holographically-Based Antenna Designs”, *URSI Radio Science Meeting Digest*, Toronto, Canada, July 2010.

CHAPTER 1

Introduction

1.1 PRINTED HIGH-GAIN MILLIMETREWAVE ANTENNAS – NEEDS AND LIMITATIONS

Antennas are required in everything that involves terrestrial or satellite wireless communications of any kind. They are ubiquitous, and are key to the quality of any wireless link, irrespective if its use. Indeed, with temporal signal processing now able to approach theoretical capacity, some see the antenna as the remaining capacity-enhancing wireless component. In order to enhance capacity, future wireless communications systems will make use of millemetrewave (mm-wave) frequencies for certain links. These systems will need relatively high-gain millimetrewave antennas [1,2] operating above 30 GHz for wireless basestations (at the macro- through pico-cell levels). Such antennas will also be needed for automotive radar, imaging security systems, and future satellite communications. In order to achieve the needed performance and yet satisfy aggressive cost constraints in commercial developments, the antennas must use printed technology that enables low-cost mass production.

Printed microstrip planar arrays appear at first to be the obvious choice, but at mm-wave frequencies the losses in printed beamforming networks (BFN) - spurious radiation loss, surface wave loss, dielectric loss, and conductor loss - is a gain-limiting factor [3]. So when moving to mm-wave frequencies simple scaling of antennas already in use at much lower frequencies is not always feasible. One alternative is to still use printed technology but to dispense with conventional feed networks. This has resulted in space fed printed lens antennas [4,5] and reflectarray antennas [6,7], and in holographic antennas [8,9,10]. One additional feature of planar holographic antennas of much interest that is not shared by reflectarrays and printed lens antennas is that the complete antenna can be made truly low profile, with the feed integrated onto the dielectric substrate(s) supporting the hologram. This is important in many commercial applications since it is also aesthetically pleasing.

The study in [3] demonstrated that the performance of microstrip arrays (which are low profile antennas) will start to be worse than that of a reflector for the same aperture size and with an aperture efficiency of 50% when the array size increases beyond roughly $10\lambda \times 10\lambda$, where λ is the free-space wavelength[1]. One of the interests in the planar holographic antenna (to be discussed in the next section) has been to produce comparable or better overall efficiency than microstrip arrays of the same aperture size.

1.2 HOLOGRAPHICALLY-BASED ANTENNA DESIGNS

A planar hologram is a recording of the interference pattern of two wavefronts on a planar surface. Once a hologram has been fabricated (conductors on a substrate) one of the wavefronts can be regenerated [11] by illuminating the hologram with the other wavefront. In antennas the wavefronts referred to are a wave from some feed (the primary wavefront) and a plane wave (the idealised radiation pattern of the antenna). An example[2] of a horn-fed planar holographic antenna is shown in Figure 1.2-1, and one of a printed antenna fed planar holographic antenna is provided in Figure 1.2-2.

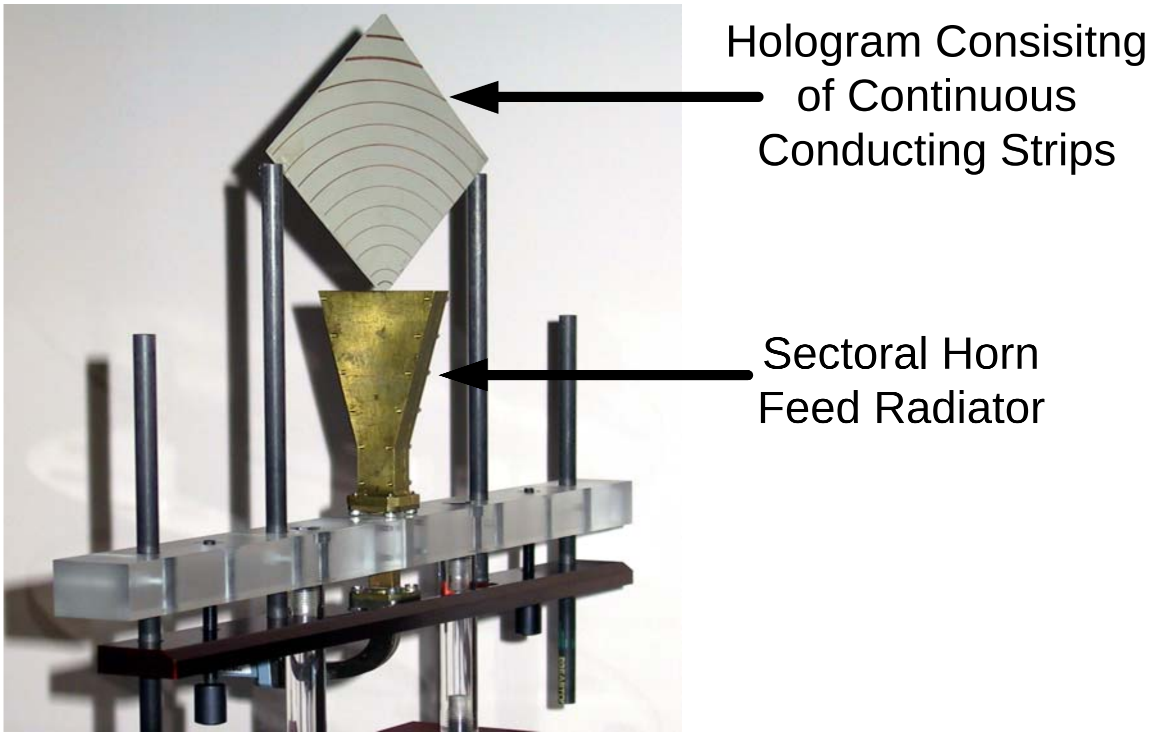

Figure 1.2-1 : Planar holographic antenna fed by a sectoral feed horn. (After [12].

---

[1] In this thesis we will use the symbol λ to denote the free space wavelength. Any other wavelength quantities will be denoted by λ with an appropriate subscript. The $10\lambda \times 10\lambda$ limitations refer to arrays operating around 30 GHz and above.

[2] A more detailed summary of planar holographic antennas will be provided in Chapter 2. However, we already emphasise here that we are in this thesis interested in holographic antennas that have main beams broadside (or very near-broadside) to the hologram, and no groundplane on the substrate that hosts the hologram.

Annotations by the Author)

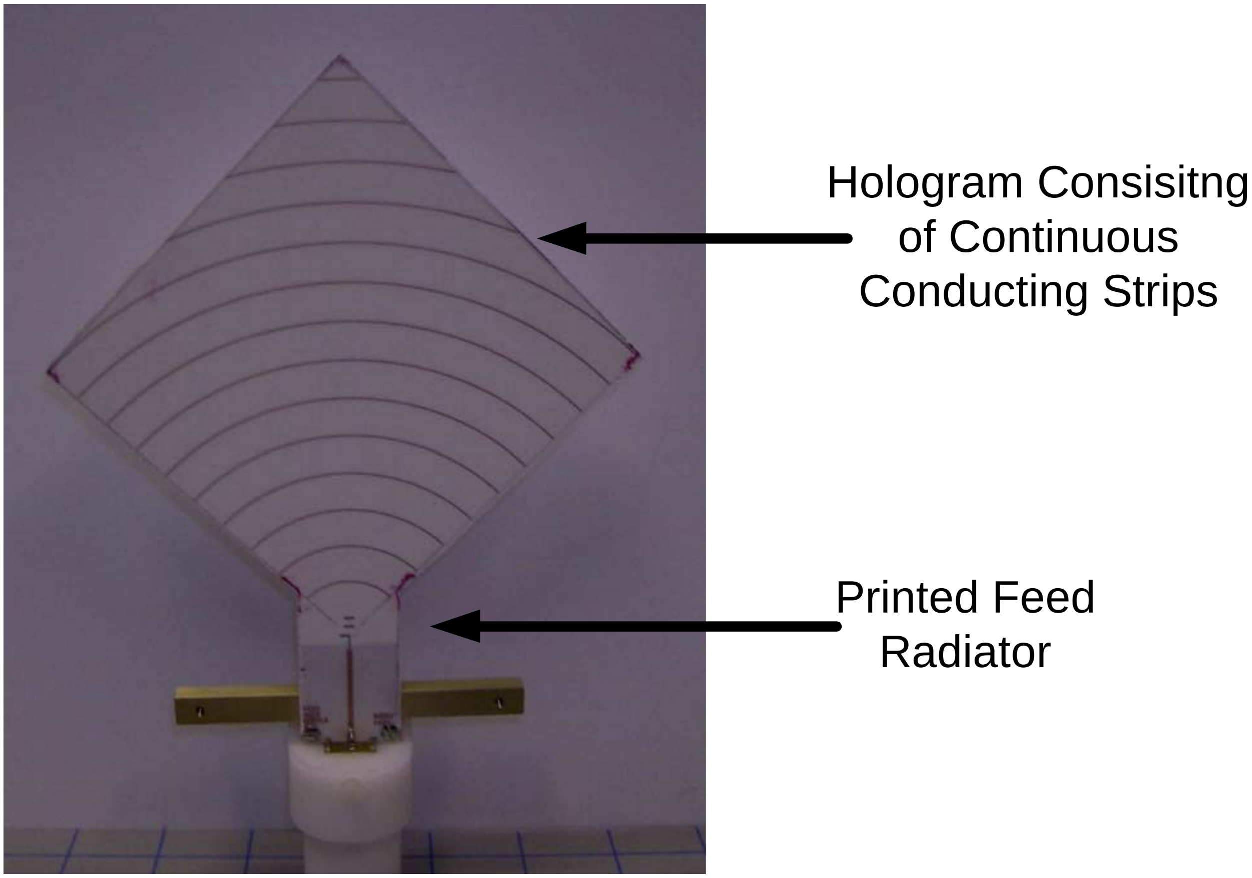

Figure 1.2-2 : Planar holographic antenna fed by a printed feed radiator. (After [13]. Annotations by the Author)

The holographic antenna concept was considered in [14,15,16] but remained largely dormant until printed planar holographic antennas were considered [8,9] for wireless applications, and more recently in groundplane-backed form [10]. However, the authors of these papers have all noted rather low overall efficiencies. A more recent design example [13] that showed some gain improvement (obtained with a completely planar structure fed by an integrated printed feed radiator) over previous cases with integrated feeds. Unfortunately, as in the above references, the overall efficiency was still lower than expected.

This thesis is concerned with research on printed planar holographic antennas such as that[3] in Figure 1.2-2. The references [8,9,14,15,16,17] did not involve detailed electromagnetic modelling. The planar holographic antenna is electrically large and dielectrically inhomogeneous, and the computational electromagnetics tools for a complete to analysis were not available at the time. A

---

[3] We will thus refer to it as *the* planar holographic antenna.

two-dimensional (2D) electromagnetic analysis was used in [12,13]; this increased the understanding of planar holographic antennas but the 2D analysis was not able to predict the directivity of true three-dimensional (3D) antennas. In spite of the analysis limitations all the above papers and theses "inched forward" the progress on planar holographic antennas. In the present thesis we will attempt to use state-of-the-art commercial electromagnetic simulation codes to perform 3D analyses of the planar holographic antennas. We will see that, in spite of major advances in CEM and its associate codes one is still limited to the analysis of planar holographic antennas of restricted electrical size, and that numerical optimisation is still not practicable due to very long simulation times. Nevertheless, we will demonstrate several aspects of holographic antenna operation not previously possible.

1.3 OVERVIEW OF THE THESIS

Chapter 2 provides a review of planar holographic antennas, and identifies a number of issues related to these antennas that are in need of investigation. Chapter 3 describes a modified array theory method which, albeit approximate and not able to model the planar holographic antenna as precisely as the numerical methods that will be the subject of subsequent chapters, will allow us to draw some important conclusions about the antenna configuration in question. There are many pitfalls and limitations in the computational electromagnetics (CEM) modelling of planar holographic antennas. Chapter 4 discusses these in some depth after reviewing the methods used in this thesis for modelling purposes. Even when one has modelling tools available, exactly what we are able to discover about the operation and characteristics of the device being modelled depends on how well we exploit these tools. Chapter 5 describes some novel ways in which we have used CEM tools to study several aspects of the operation of the planar holographic antenna. Some general conclusions are drawn in Chapter 6, which concludes the thesis.

1.4 REFERENCES FOR CHAPTER 1

[1] D.Liu, U.Pfeiffer, J.Grzyb & B.Gaucher, *Advanced Millimeter-Wave Technologies : Antennas, Packaging and Circuits* (Wiley,2009).

[2] J.F.Kiang (Edit.), *Novel Technologies for Microwave and Millimeter-Wave Applications* (Kluwer,2004).

[3] E. Levine, G.M. Malamud, S. Shtrikman and D. Treves, “ A study of microstrip array antennas with the feed network”, *IEEE Trans. Antennas Propagat.*, Vol.37, No.4, pp.426-433, April 1989.

[4] N.Gagnon, A.Petosa and D.A.McNamara, "Thin Microwave Quasi-Transparent Phase-Shifting Surface(PSS)", *IEEE Trans. Antennas Propagat.,*Vol.28,pp.1193-1201,Apr.2010.

[5] N.Gagnon, A.Petosa & D.A.McNamara, “Comparison between conventional lenses and an electrically thin lens made using a phase shifting surface (PSS) at Ka band”, *Proc. Loughborough Antennas Propagat. Conf. (LAPC 2009)*, pp.117-120, UK, Nov. 2009.

[6] J.Huang and J.A.Encinar, *Reflectarray Antennas* (Wiley, 2008).

[7] A.Roederer,"Reflectarray antennas", *Proc. 3rd European Conf. Antennas Propagat.* (EuCAP), pp.18-22, March 2009.

[8] K.Lévis, A.Ittipiboon, A.Petosa, L.Roy and P.Berini, "Ka-band dipole holographic antennas", *IEE Proc., Microw. Antennas Propagat.,* Vol.148, No.2, pp. 129-132, April 2001.

[9] A.Petosa, S.Thirakoune, K.Lévis and A.Ittipiboon, "Microwave holographic antenna with integrated printed dipole feed", *Electron. Lett.,* Vol.40, pp.1162-1163, Sept.2004.

[10] B.H.Fong J.S.Colburn, J.J.Ottusch, J.L.Visher and D.F.Sievenpiper, "Scalar and tensor holographic artificial impedance surfaces", *IEEE Trans. Antennas Propagat.,* Vol. 58, No. 10, pp. 3212 – 3221, Oct.2010

[11] J.W. Goodman, *Introduction to Fourier Optics* (McGraw-Hill, 1996).

[12] P. Sooriyadevan, “The Electromagnetic Modelling and Optimization of Planar Holographic Antennas”, *M.A.Sc Thesis*, University of Ottawa, Ottawa, ON, Canada, 2004.

[13] T.Quach, “Holographic Antennas Realized from Interference Patterns Determined in the Presence of the Dielectric Substrate”, *M.A.Sc Thesis*, University of Ottawa, Ottawa, ON, Canada, 2005.

[14] P.F.Checcacci, V.Russo and A.M.Scheggi, "Holographic antennas", *Proc. IEEE,* Vol.56, pp.2165-2167, Dec.1968.

[15] P.F.Checcacci, V.Russo and A.M.Scheggi, "Holographic antennas", *IEEE Trans. Antennas Propagat.*, Vol.18, pp.812-813, Nov.1970. (Note that this has the same title as, but is different from, [2])

[16] K. Iizuka, M. Mizusawa, S. Urasaki, and H. Ushigome, “Volume-type holographic antenna”, *IEEE Trans. Antennas Propagat.*, Vol.23, No.6, pp.807-810, Nov. 1975.

[17] K. Levis, “Ka-Band Holographic Antennas”, *M.A.Sc Thesis*, University of Ottawa, Ottawa, ON, Canada, 1999.

CHAPTER 2

Review of Holographically-Based Antennas

2.1 INTRODUCTION

The purpose of this chapter is to provide some fundamental material that will aid in the reading of Chapters 3 through 6. In Section 2.2 we provide a re-examination of the idealized interference pattern between a spherical wave and a plane wave, which forms the conceptual basis for planar holographic antennas. Not only will this clarify some minor points not usually mentioned elsewhere, but it will provide a result we will need in Chapter 5. Section 2.3 discusses how the planar holographic antenna idea arises through the use of conducting tracks to record the above interference pattern. A review of existing planar holographic antenna work is presented in Section 2.4, and some concluding remarks in Section 2.5 will lead us into the next chapter. It should be noted in this chapter we have arranged the references chronologically (since this in itself provides information on the path of development of holographic antennas over the last 40 years, and will thus not strive to refer to the references in numerical order as is customary.

2.2 A BRIEF RE-EXAMINATION OF THE IDEALISED INTERFERENCE PATTERNS

As stated in Section 1.2, a planar hologram is a recording of the interference pattern of two wavefronts on a planar surface. In antenna work the wavefronts referred to are a spherical wave from some feed (the primary wavefront) and a plane wave (the idealised radiation pattern of the antenna, which is the secondary wave). The set up is illustrated in Figure 2.2-1, where we assume that the spherical wave source is located at the coordinate origin $(x, y, z) = (0, 0, 0)$. Using an idealized scalar analysis, the standard expression for a spherical wave is

$$E_{\mathrm{p}}(x, y, z) = A_p \frac{e^{-jkr}}{r} = A_p \frac{e^{-jk\sqrt{x^2+y^2+z^2}}}{\sqrt{x^2+y^2+z^2}} \tag{2.2-1}$$

where A_p is the amplitude of the spherical wave (the primary wave) and $k = 2\pi / \lambda$. The plane wave incident along the y-axis (in the positive y-direction) is described by the expression

$$E_s(x,y,z) = A_s e^{-jky} \tag{2.2-2}$$

where A_s is the amplitude of the plane wave (the secondary wave). If the interference pattern $|E_{\text{total}}(x,y,z)|$, where

$$E_{\text{total}}(x,y,z) = E_p(x,y,z) + E_s(x,y,z) = A_p \frac{e^{-jk\sqrt{x^2+y^2+z^2}}}{\sqrt{x^2+y^2+z^2}} + A_s e^{-jky} \tag{2.2-3}$$

is computed along any radial line starting at the point the location at the point $(x,y,z)=(0,0,0)$ of the spherical wave source, we observe the interference pattern behaviour shown in Figure 2.2-2 with $A_p = 5A_s$. If we remove the distance-dependent decay term $1/r$ from the spherical wave field expression, and plot

$$|E_{\text{total}}(x,y,z)| = \left| A_p e^{-jk\sqrt{x^2+y^2+z^2}} + A_s e^{-jky} \right| \tag{2.2-4}$$

we obtain the two-dimensional colour-code plot in Figure 2.2-3 if $A_p = A_s$, which is centred at the point $(x,y,z)=(0,0,0)$. This is the familiar form shown in texts on optical holography, with concentric rings of complete destructive interferences (zero field lines). Sampled along the positive z-axis this is the form shown in Figure 2.2-4. The dips of Figure 2.2-2 are now the nulls in Figure 2.2-4, and are one wavelength apart. The depths of the dips in Figure 2.2-2 can be controlled by adjusting the relative values of A_p and A_s. The dips in Figure 2.2-2 occur at slightly different locations to the nulls in Figure 2.2-4.

The holographic concept is to record the interference pattern in some way, this recording being called the hologram. The holographic principle maintains that if the hologram is now illuminated by the primary wave the scattered field from the hologram will consist of the secondary wave (used to generate the interference pattern) plus various other terms (which are usually unwanted). In antenna work the secondary pattern is chosen to be a plane wave as representative of the high-directivity main lobe we'd like the holographic antenna to have.

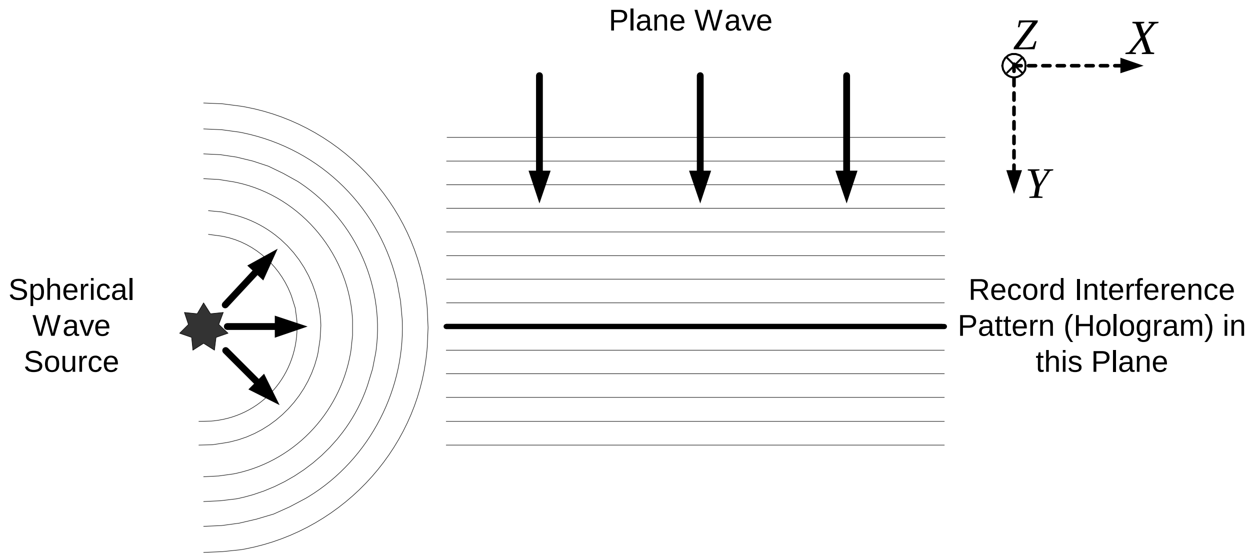

Figure 2.2-1 : Interference of a spherical wave and a plane wave.

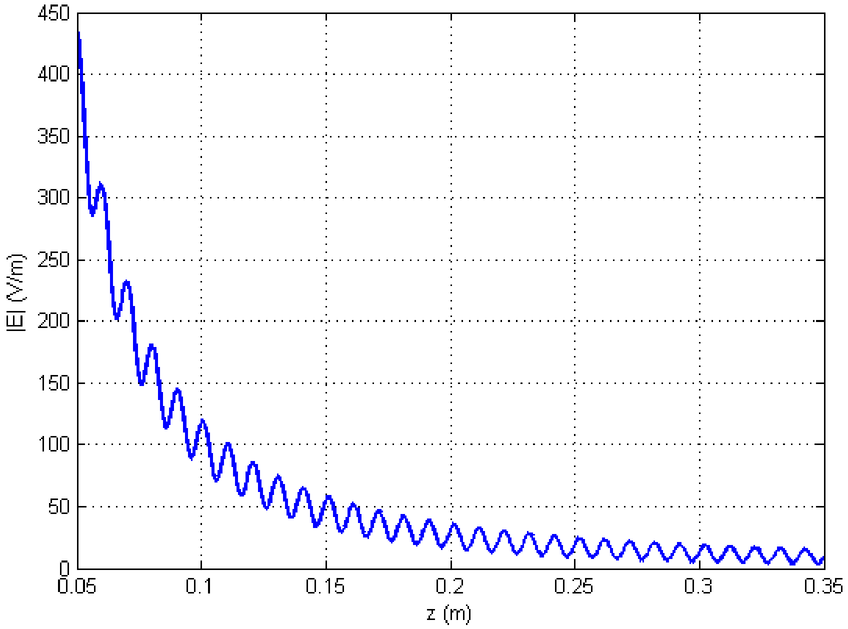

Figure 2.2-2 : Plot of the interference pattern $|E_{\text{total}}(0,0,z)|$ using expression (2.2-3)

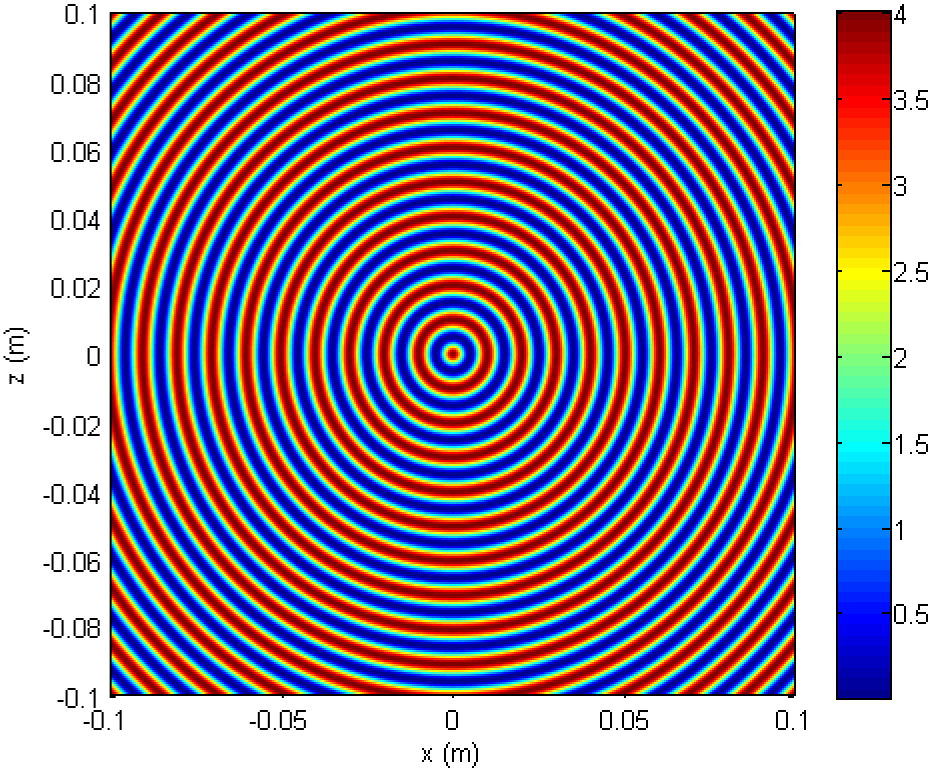

Figure 2.2-3 : Plot of the interference pattern $\left|E_{\text{total}}(x,0,z)\right|$ (V/m) at 30 GHz

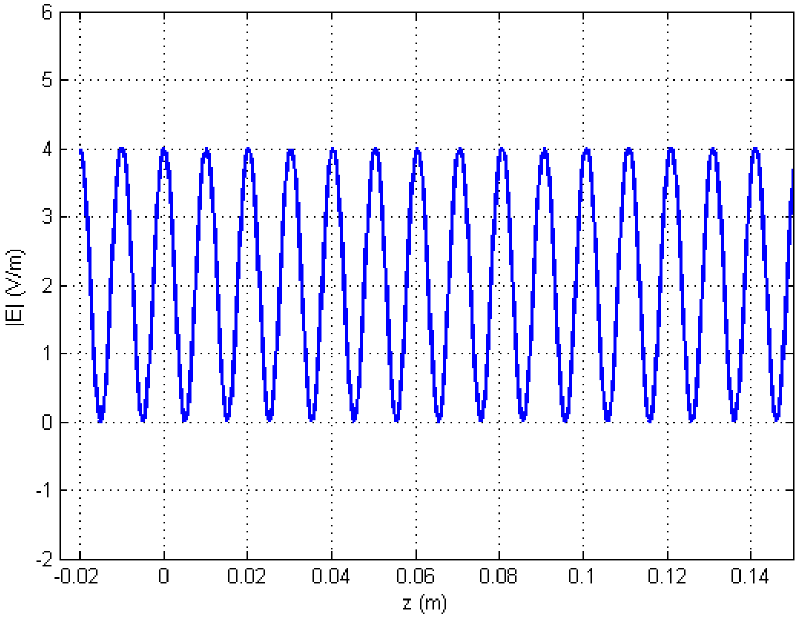

Figure 2.2-4 : Plot of the interference pattern $\left|E_{\text{total}}(0,0,z)\right|$ using expression (2.2-4). It is a "cut" through a portion of the result shown in Figure 2.2-3.

2.3 THE PLANAR HOLOGRAPHIC ANTENNA

Examination of the interference pattern in Figure 2.2-3 allows us to locate the rings along which the interference pattern is zero. The argument in holographically based antenna work [3,5,7] runs as follows : We place conducting strips along the above-mentioned arcs. If the polarisation of the primary source is such that its electric field is parallel to these conductors, then the field will indeed be zero along these arcs. The conductor pattern will thus be a recording (albeit a binary one) of the interference pattern (in other words, a hologram).

More detailed explanations are available elsewhere [9]. Here we will illustrate the process diagrammatically. Figure 2.3-1 shows a corner of the interference pattern marked off by dashed lines. A horn is indicated as being the primary radiator, but this need not be the case. Figure 2.3-2 shows the zero-field arcs replaced by conducting strips. These would be "snipped" along the dashed line to form the hologram. In practice the hologram would be etched on a dielectric substrate, as illustrated in Figure 2.3-3. It is not necessary to use continuous conducting strips. Conducting dipoles have also been used [11], as sketched in Figure 2.3-4, and in fact shown to provide greater polarisation purity. As briefly mentioned earlier, when holograms such as those mentioned above are illuminated by the primary source the wavefront reconstruction process predicts [1,2] that we should expect four beams at right angles to each other, two of which correspond to the plane wave used to generate the interference pattern and its conjugate (and which constitute the top and bottom broadside lobes – broadside to the plane of the hologram - shown in Figure 2.3-5). We emphasize that the secondary source plus the constructed hologram constitute the holographic antenna.

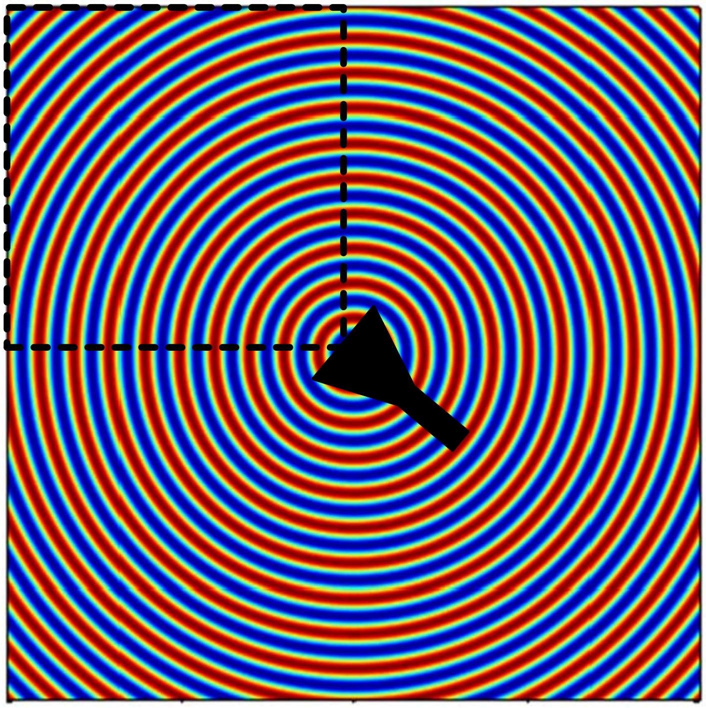

Figure 2.3-1 : Plot of the interference pattern $\left|E_{\text{total}}(x,0,z)\right|$ (V/m) at 30 GHz

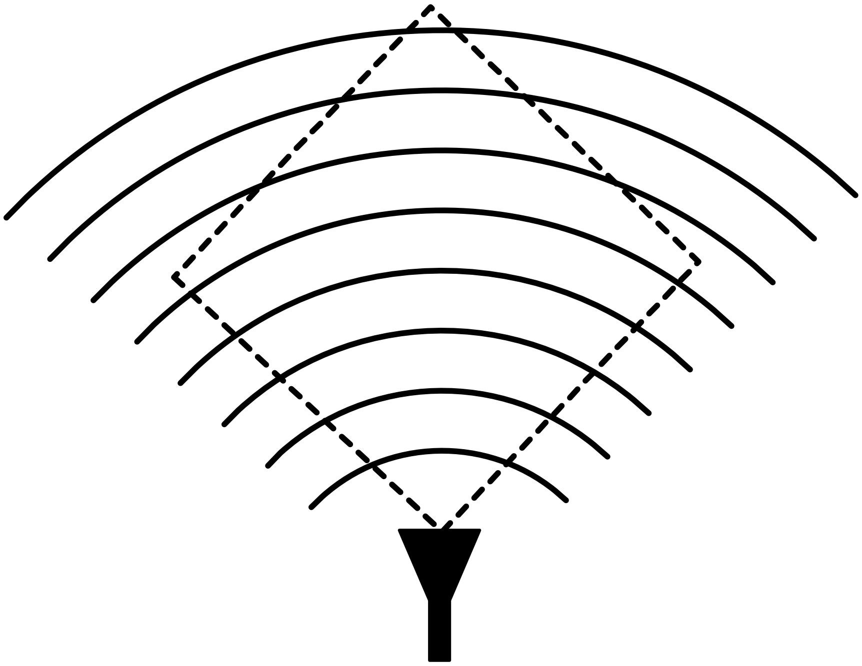

Figure 2.3-2 : Hologram recorded by placing conducting strips along the zero-field arcs of the interference pattern.

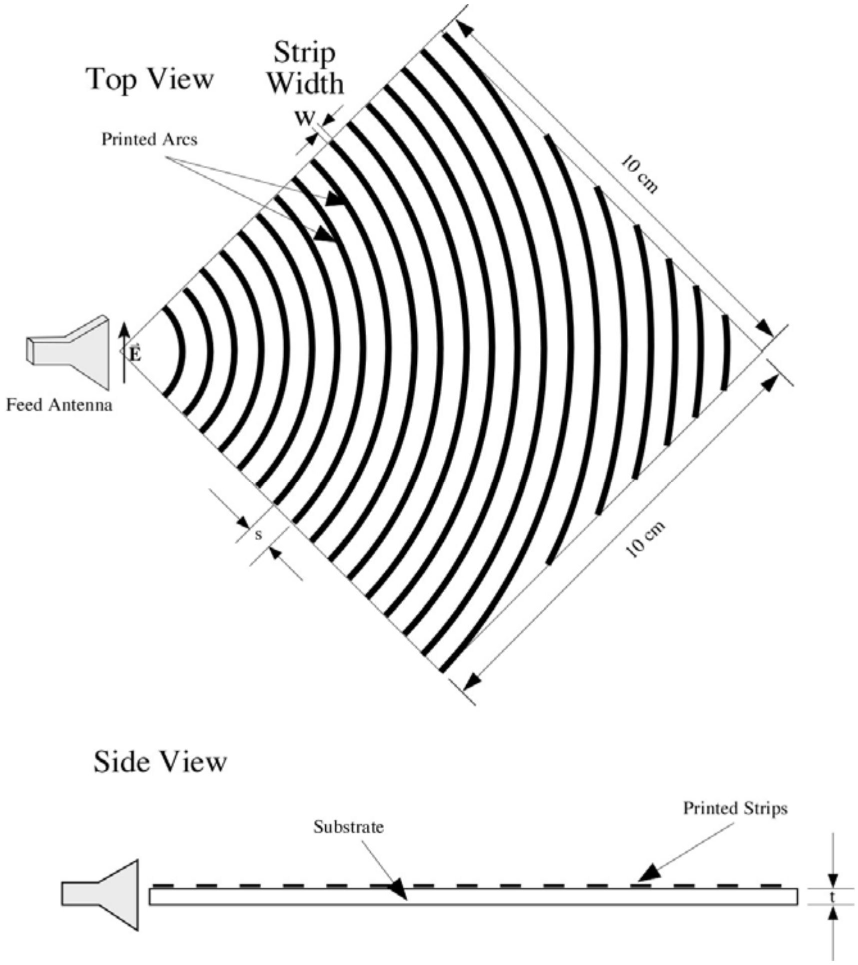

Figure 2.3-3 : Holographic antenna consisting of the hologram (the continuous conducting strips) and a horn antenna as the source of the primary wave. (Courtesy of A.Petosa)

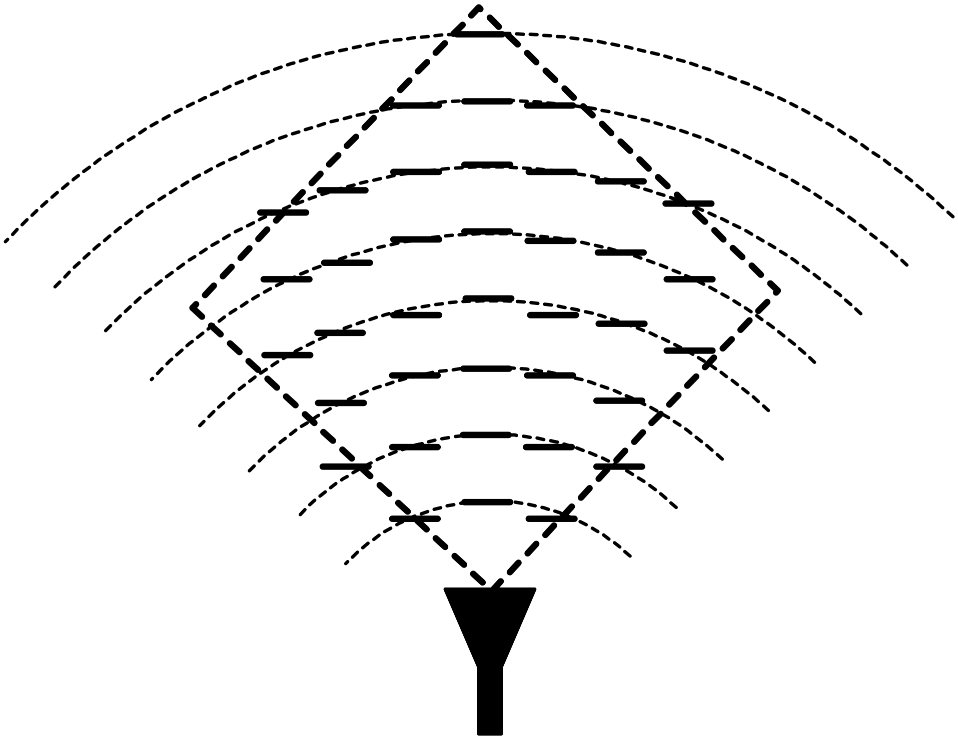

Figure 2.3-4 : Hologram recorded by placing conducting dipoles along the zero-field arcs of the interference pattern.

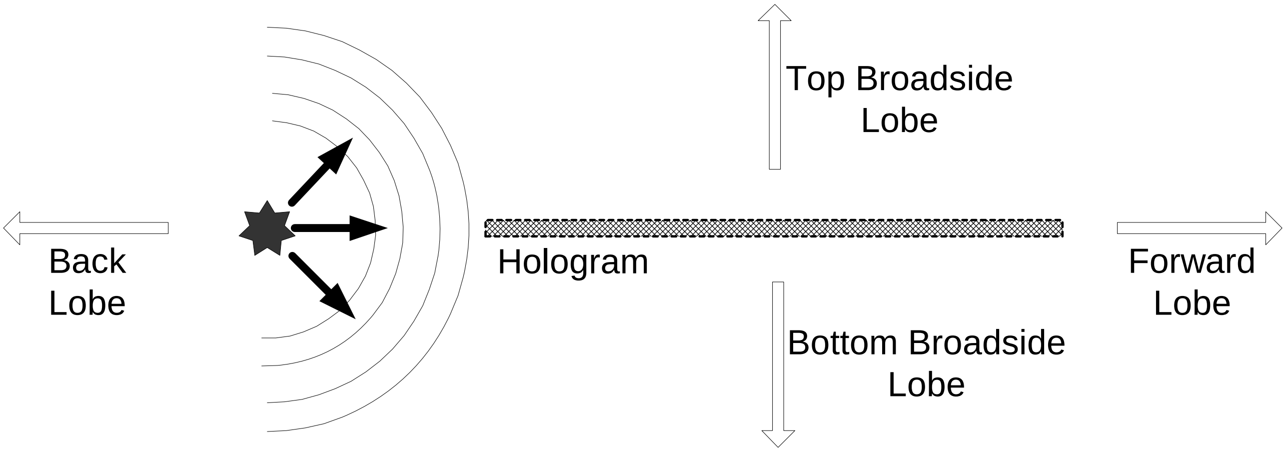

Figure 2.3-5 : The holographic (wavefront reconstruction) process produces four wavefronts when the hologram is illuminated by the secondary source.

2.4 EXISTING PLANAR HOLOGRAPHIC ANTENNAS

Planar holographically-based antennas (hereafter referred to as holographic antennas), as opposed to holographic principles used for other purposes both at optical and RF frequencies, have been the subject of research papers for about 40 years, with increased interest over the last 12 years. They can be divided into two broad categories, those that have hologram elements above a groundplane, and those without a groundplane, as shown in Figure 2.4-1.

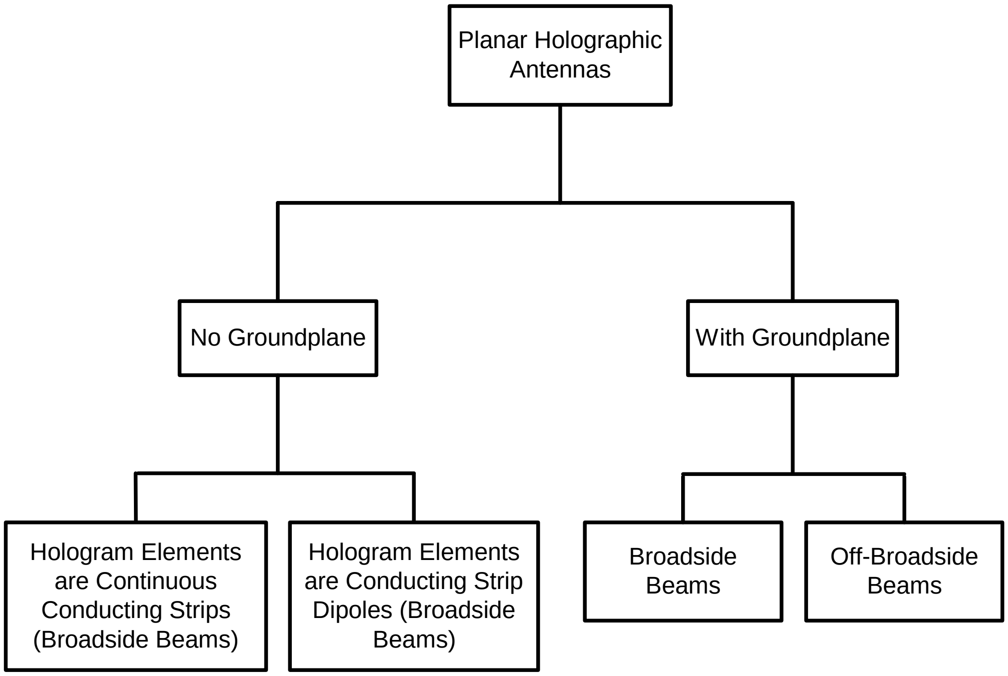

Figure 2.4-1 : Classification of planar holographic antenna types.

In this thesis we are interested in the type without the groundplane, and in particular wish to generate broadside beams. Table 2.4-1 divides up the existing literature into the various types of holographic antennas. References [8, 12, 21, 22] are concerned with the use of holograms to replace reflectors for compact antenna test ranges (in other words, to provide planes waves to illuminate antennas under test). Reference [28] shows that Fresnel zone plate antennas can be interpreted in terms of holographic principles. However, such holograms, like those for compact antenna test ranges and those in [10], are illuminated with primary waves at near normal incidence, and not at grazing incidence like the ones we are interested in here (in order to achieve low profile antennas).

The holographic antennas that use groundplanes all utilize the groundplane /substrate combination to launch surface waves that illuminate the hologram, and so in most cases these essentially leaky-wave antennas have main beams that are not close to the broadside direction, except for [15] and [39].

In this thesis we are specifically interested in the functioning of planar holographic antennas that do not use a groundplane, and so [9,11,16,17,18,19]. Both horn radiator and printed radiator excitation of the hologram have been used in the latter references. Single-layer versions give a broadside beam in two directions. Double-layer versions, with appropriate spacing and shift between the layers, is able to reduce the one broadside beam. As will be discussed in Chapter 4, the above-mentioned references did not involve detailed three-dimensional electromagnetic modelling of the complete holographic antennas (feed radiator plus hologram) due to the fact that such holographic antennas are electrically large and dielectrically inhomogeneous. In this thesis we wish to see what rigorous numerical simulation of complete holographic antennas is now possible in order to improve the overall efficiency of such antennas, which is usually much less than 20%, as reported in the above-mentioned references. Although the antennas we may wish to actually design and use might be larger than what can currently be modelled, electrically smaller cases will be modelled and their operation studied to arrive at design principles that can be applied to larger ones.

Table 2.4-1 : Summary of Planar Holographic Antenna Types

With Groundplane	No Groundplane	Broadside Beams	Off-Broadside Beams	Continuous Conducting Strip Elements	Conducting Strip Dipole Elements	Other Elements	Double Shifted Hologram Layers	References
×			×			×		20,25,26,30 38
×		×			×			14,15,31,32 33,35,39
×			×	×				23,27,29,34
	×	×		×				3,5,6,9,11,16 17,18,19,24
	×	×			×			9,11
	×	×		×			×	7,9,11
	×	×			×		×	9,11

2.5 SELECTED HOLOGRAM AND YAGI-RADIATOR DESIGNS

As stated in the previous section, it is the feasibility of using electromagnetic simulation of complete holographic antennas that is being examined here. We will therefore use some existing holographic antenna designs.

Three different feed radiators will be used to illuminate the holograms considered. Firstly, we will use the E-plane sectoral horn described in [9,17]. Its dimensions will be slightly altered, and so will be provided when required in Section 5.3. Two different Yagi radiators will be used. Much has been written on the design of Yagi antennas, both wire types [40,41,42,43,45] and printed forms [44,46,47,48,49,50,51]. One of those we will use is the 3-element design from [18], which is depicted in Figures 2.5-1 and 2.5-2, and was designed for a substrate thickness of 20 mils and relative permittivity of 3.38. We will also use the 6-element Yagi shown in Figure 2.5-3. Since it will not be used with a substrate (for reasons that will be clear later) it has been designed using tables in [45], and uses the same balun concept as the 3-element case. In both cases it is not possible to use reflector elements in the Yagi because of the presence of the groundplane of the microstrip balun.

With reference to Figure 2.3-4, once the locations of the nulls (the rings shown as dashed lines) are decided we can construct a holographic antenna in two ways. In the one type we simply place continuous conducting strips along these rings, within the diamond-shaped boundary. In the other type we place strip dipoles at points along these rings as shown in Figure 2.3-5, where only a portion of the structure is shown. For convenience we will refer to holograms that use different ring radii as holograms #1, #2 and #3, as listed in Table 2.5-1. We can then simply state whether the continuous or dipole type hologram element is used.

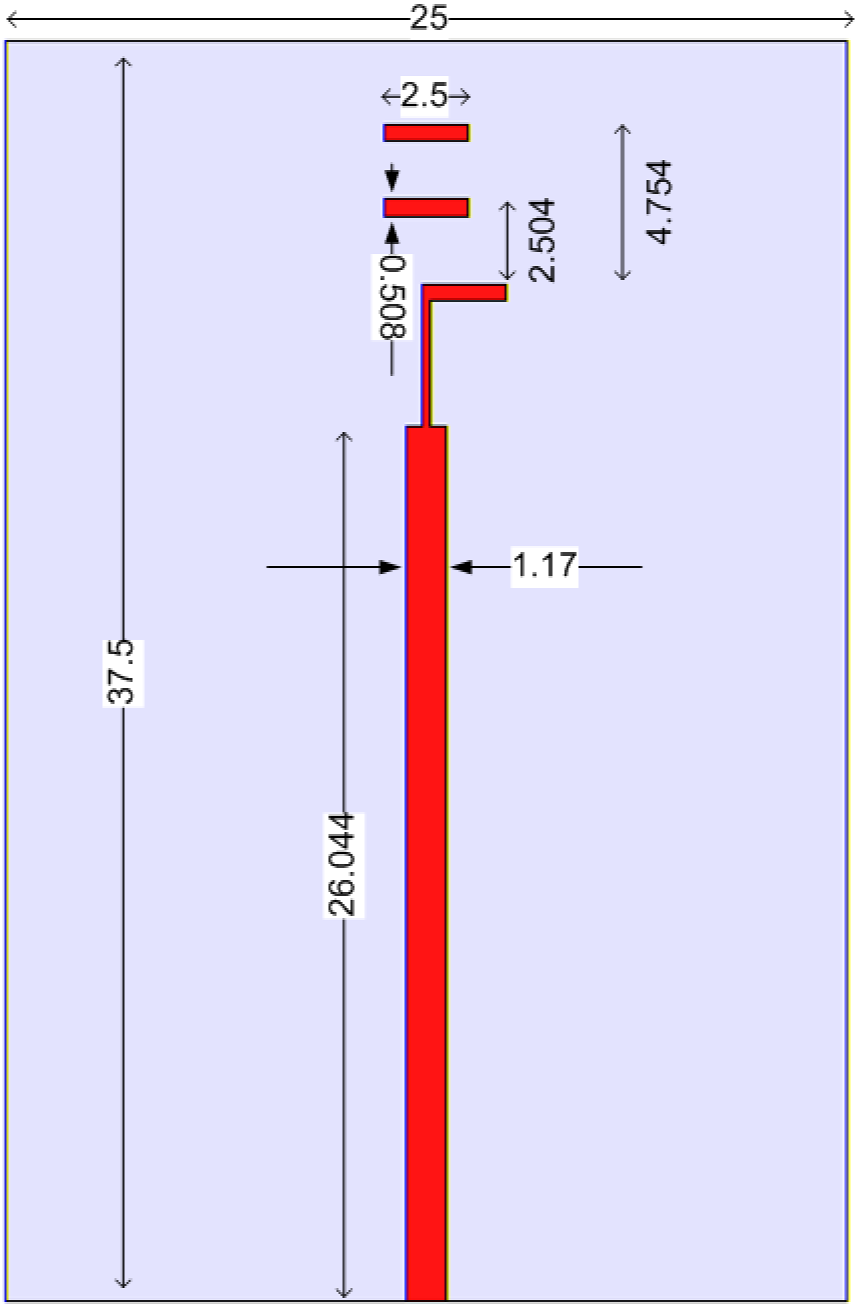

Figure 2.5-1 : Three-element Yagi conductor layout on top of substrate. Dimensions are shown in mm. (After [18])

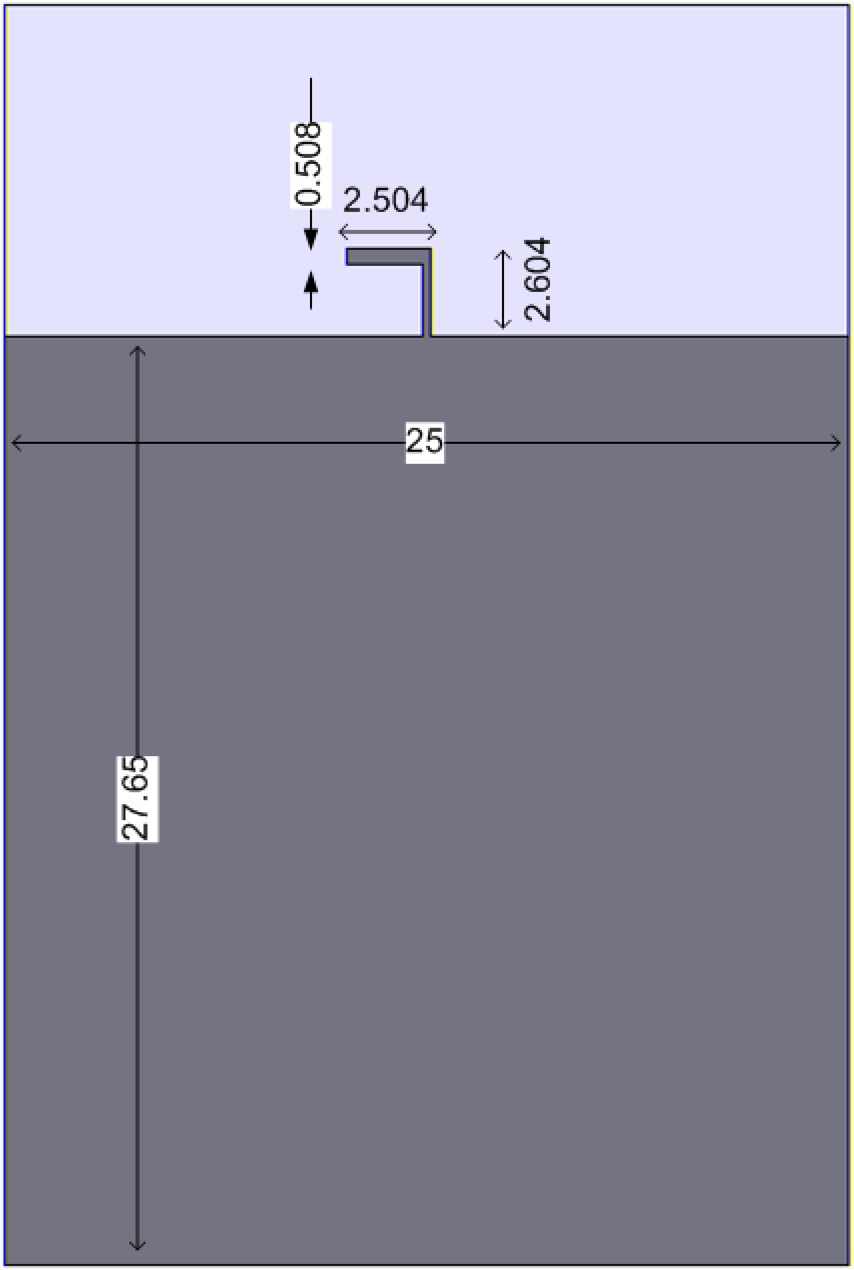

Figure 2.5-2 : Three-element Yagi conductor layout on bottom of substrate (After [18])

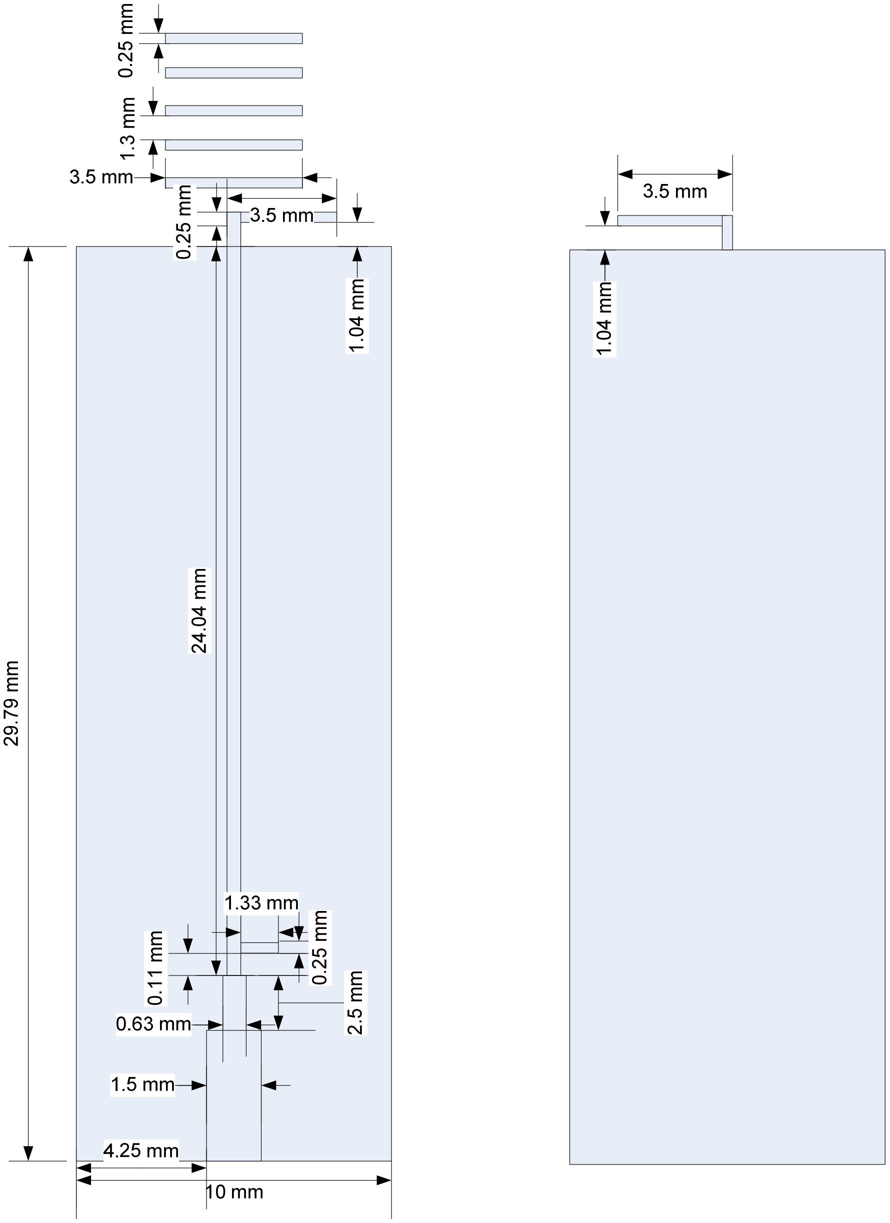

Figure 2.5-3 : Six-element Yagi layout

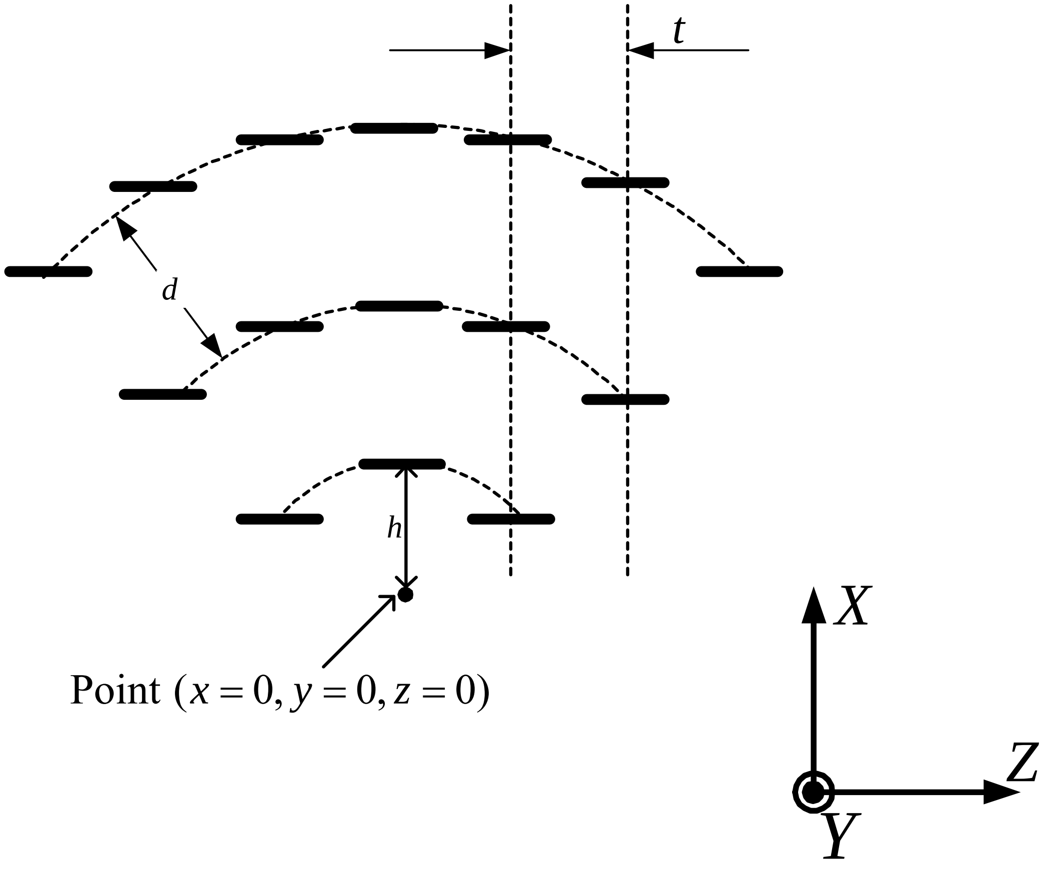

Figure 2.5-4 : Layout of dipoles in hologram. Quantity d depends on the ring radii selected, $t=\lambda/2$, and the dipole lengths are all $\lambda/2$.

Table 2.5-1 : Location of Rings (Nulls in Interference Patterns) for Various Holograms

Ring Number	Ring Radius (m) Idealised Case (Expression 2.2-3) Hologram#1	Ring Radius (m) Idealised Case (Expression 2.2-4) Hologram#2	Ring Radius (m) Ref. [18] Hologram#3[4]
1	0.0162	0.01000	0.0146
2	0.0254	0.02000	0.0240
3	0.0356	0.03000	0.0334
4	0.0456	0.04000	0.0428
5	0.0552	0.05000	0.0552
6	0.0656	0.06000	0.0615
7	0.0756	0.07000	0.0709
8	0.0856	0.08000	0.0803
9	0.0958	0.09000	0.0897
10	0.1058	0.10000	0.0991
11	0.1159	0.11000	0.1085
12	0.1260	0.12000	0.1179
13	0.1360	0.13000	0.1273
14	0.1460	0.14000	0.1367

---

[4] These are slightly altered versions of the values used for Hologram#2. They account for an effective permittivity, amongst other things. Details are given in [18].

2.6 CONCLUDING REMARKS

This chapter has described the ideas underlying the planar holographic antenna, and laid the basis for the thesis work to be described in the chapters that follow. The idealized interference patterns discussed in Section 2.2 will be compared to actual situations modelled using the FDTD method in Section 5.1. The treatment in Section 2.3 will ensure that the reader is familiar with the configurations that will be analysed in this work. We will refer back to the review of existing planar holographic performance in order to motivate what is done in later chapters.

2.7 REFERENCES FOR CHAPTER 2

[1] J.W. Goodman, *Introduction to Fourier Optics* (McGraw-Hill, 1996).

[2] S.Ramo, J.R.Whinnery and T. van Duzer, "Fields and Waves in Communication Electronics (Wiley, 1994) pp.801-805.

[3] P.F.Checcacci, V.Russo and A.M.Scheggi, "Holographic antennas", *Proc. IEEE,* Vol.56, pp.2165-2167, Dec.1968.

[4] W.E.Kock, "Microwave holography", Microwaves, pp.46-54, Nov.1968.

[5] P.F.Checcacci, V.Russo and A.M.Scheggi, "Holographic antennas", *IEEE Trans. Antennas Propagat.*, Vol.18, pp.812-813, Nov.1970. (Note that this has the same title as, but is different from, [2])

[6] P.F.Checcacci, G.Papi and V.Russo, "A holographic VHF antenna", *IEEE Trans. Antennas Propagat.*, Vol.21, No.3, pp.278-279, March 1971.

[7] K. Iizuka, M. Mizusawa, S. Urasaki, and H. Ushigome, "Volume-type holographic antenna", *IEEE Trans. Antennas Propagat.*, Vol.23, No.6, pp.807-810, Nov. 1975.

[8] T.Hirvonen, J.Ala-Laurinaho, J.Tuovinen and A.V.Räisänen, "A compact antenna test range based on a hologram", IEEE Trans. Antennas Propagat., Vol.45, No.8, pp.1270-1276, Aug.1997.

[9] K. Levis, "Ka-Band Holographic Antennas", *M.A.Sc Thesis*, University of Ottawa, Ottawa, ON, Canada, 1999.

[10] D.M.Sazanov, "Computer-aided design of holographic antennas", IEEE Int. Antennas Propagat. Symp. Digest, pp.738-741, July 1999.

[11] K.Lévis, A.Ittipiboon, A.Petosa, L.Roy and P.Berini, "Ka-band dipole holographic antennas", I*EE Proc., Microw. Antennas Propagat.,* Vol.148, No.2, pp. 129-132, April 2001.

[12] J.Salo et al., "Millimetre-wave Bessel beams using computer holograms", Electronics Letters, Vol.37, No.13, pp.834-835, June 2001.

[13] S.R. Thingvold, A. Ittipiboon, A. Sebak, and A. Petosa, “Holographic antenna efficiency”, IEEE Int. Antennas Propagat. Symp. Digest, Vol.3, pp. 721 – 724, July 2003.

[14] A.E.Fathy, M. ElSherbiny, A. Rosen, G. Ayers and S.M. Perlow, “Experimental demonstration of a 35 GHz holographic antenna", IEEE Microwave Symp. Digest, pp.1833-1836, 2003.

[15] M. ElSherbiny, A.E. Fathy, A. Rosen, G. Ayers, and S.M. Perlow, “Holographic antenna concept, analysis, and parameters”, IEEE Trans. Antennas Propagat., Vol.52, No.3, pp. 830 – 839, March 2004.

[16] A.Petosa, S.Thirakoune, K.Lévis and A.Ittipiboon, "Microwave holographic antenna with integrated printed dipole feed", *Electron. Lett.,* Vol.40, pp.1162-1163, Sept.2004.

[17] P. Sooriyadevan, “The Electromagnetic Modelling and Optimization of Planar Holographic Antennas”, *M.A.Sc Thesis*, University of Ottawa, Ottawa, ON, Canada, 2004.

[18] T.Quach, “Holographic Antennas Realized from Interference Patterns Determined in the Presence of the Dielectric Substrate”, *M.A.Sc Thesis*, University of Ottawa, Ottawa, ON, Canada, 2005.

[19] T.Quach, D.A.McNamara and A.Petosa, "Holographic antenna realized using interference patterns determined in presence of dielectric substrate", *IEE Electronics Letters.,* Vol.41, No.13, pp.724-725, June 2005.

[20] D. Sievenpiper, J. Colburn, B. Fong, J. Ottusch and J. Visher, “Holographic artificial impedance surfaces for conformal antennas”, IEEE Int. Antennas Propagat. Symp. Digest, July 2005

[21] J.Häkli et al, "Sub-mm antenna tests in a hologram–based CATR", IEEE Antennas Propagat. Magazine, Vol.47, No.4, pp.237, Aug.2005.

[22] J.Häkli et al, "Testing of a 1.5m reflector antenna at 322 GHz in a CATR based on a hologram", IEEE Trans. Antennas Propagat., Vol.53, No.10, pp.3142, Oct.2005.

[23] F.Caminita, M.Nannetti and S.Maci, "Holographic surfaces realized by curvilinear striop gratings", 2nd European Conf. Antennas Propagat. (EuCAP 2007), March 2007 (CD-ROM).

[24] P.Sooriyadevan, D.A.M^{c}Namara, A.Petosa & A.Ittipiboon, “Electromagnetic Modelling and Optimisation of a Planar Holographic Antenna”, IET Proceedings (formerly *IEE Proceedings) : Microwaves, Antennas & Propagation*, Vol.1, Issue 3, pp.693-699, June 2007.

[25] B.H.Fong J.S.Colburn, P.R.Herz, J.J.Ottusch, D.F.Sievenpiper and J.L.Visher, "Polarisation controlling holographic artificial impedance surfaces", IEEE Int. Antennas Propagat. Symp. Digest, pp.3824-3827, July 2007.

[26] J.S.Colburn, D.Sievenpiper, B.H.Fong, J.J.Ottusch and P.R.Herz, "Advances in artificial impedance surface conformal antennas", IEEE Int. Antennas Propagat. Symp. Digest, pp.3820-

3823, July 2007.

[27] M.Nannetti, F.Caminita and S.Maci, "Leaky-wave based interpretation of the radiation from holographic surfaces", IEEE Int. Antennas Propagat. Symp. Digest, pp.5813-5816, July 2007.

[28] A.Petosa and A.Ittipiboon, "Comparison of an elementary hologram and a Fresnel zone plate", URSI Radio Science Bulletin, No.324, pp.29-36, March 2008.

[29] F.Caminita, M.Nannetti and S.Maci, "A design method for curvilinear strip grating holographic antennas", IEEE Int. Antennas Propagat. Symp. Digest, July 2008. (CD-ROM)

[30] D.F.Sievenpiper, "Artificial Impedance Surfaces for Antennas", Chapter 15 in : C.A.Balanis, *Modern Antenna Handbook* (Wiley, 2008).

[31] A.Sutinjo, M.Okoniewski and R.H.Johnson, "A holographic antenna approach to improve the surface wave efficiency and gain of a microstrip patch", 13th Int. Symp. Antenna Technology & Applied Electromagnetics (ANTEM), 2009. (CD-ROM)

[32] A.Sutinjo, M.Okoniewski and R.H.Johnson, "A holographic antenna approach for surface wave control in microstrip antenna applications", *IEEE Trans. Antennas Propagat.,* Vol. 58, No.3, pp. 675-682, March 2010.

[33] A.Sutinjo and M.Okoniewski, "A broadside radiating holographic antenna excited by a travelling wave patch array", 2010 Int. Workshop Antenna Tech. (iWAT), March 2010 (CD-ROM).

[34] M.Albani, M.Bandinelli, F.Caminita, P. de Vita, A.Freni, S.Maci, A.Mazzinghi, G.Minatti and M.Sabbadini, "Holographic antennas : Principle of operation and design guiidelines", 4th European Conf. Antennas Propagat. (EuCAP 2010), April 2010 (CD-ROM).

[35] A.Sutinjo and M.Okoniewski, "A broadside radiating holographic antenna excited by a travelling wave patch array", IEEE Int. Antennas Propagat. Symp. Digest, July 2010. (CD-ROM)

[36] G.Minatti, F.Caminita and S.Maci, "A circularly polarized dielectric lens antenna designed by holographic principles", 4th European Conf. Antennas Propagat. (EuCAP 2010), April 2010 (CD-ROM).

[37] G.Minatti, F.Caminita and S.Maci, "A circularly polarized dielectric lens antenna designed by holographic principles", IEEE Int. Antennas Propagat. Symp. Digest, July 2010. (CD-ROM)

[38] B.H.Fong J.S.Colburn, J.J.Ottusch, J.L.Visher and D.F.Sievenpiper, "Scalar and tensor holographic artificial impedance surfaces", *IEEE Trans. Antennas Propagat.,* Vol. 58, No. 10, pp. 3212 – 3221, Oct.2010

[39] A.Sutinjo and M.Okoniewski, "A surface wave holographic antenna for broadside radiation excited by a travelling wave patch array", *IEEE Trans. Antennas Propagat.,* Vol. 59, No.1, pp.297-300, Jan.2011.

[40] G.A.Thiele, "Analysis of Yagi-Uda-type antennas", IEEE Trans. *Antennas Propagat.,* Vol. 17, No.1, pp.24-31, Jan.1969.

[41] D.K.Cheng and C.A.Cehn, "Optimum element spacings for Yagi-Uda arrays", IEEE Trans. *Antennas Propagat.,* Vol.21, No.5, pp.615-623, Sept.1973.

[42] D.Kajfez, "Nonlinear optimization reduces the sidelobes of Yagi antenna", IEEE Trans. *Antennas Propagat.,* Vol.21, No.5, pp.714-715, Sept.1973.

[43] C.A.Chen and D.K.Cheng, "Optimum element lengths for Yagi-Uda arrays", IEEE Trans. *Antennas Propagat.,* Vol.23, No.1, pp.8-15, Jan.1975.

[44] A.R.Perkons and T. Itoh, "Surface wave excitation of a dielectric slab by a Yagi-Uda slot array antenna", Proc. 26th European Microwave Conf., pp.625-628, Sept.1996.

[45] C. Balanis, Antenna Theory: Analysis and Design (Wiley, 1997).

[46] Y.Qian, W.R. Deal, N. Kaneda and T. Itoh, "Microstrip-fed quasi-Yagi antenna with broadband characteristics", Electronics Letters, Vol.34, No.23, pp. 2194 –2196, Nov. 1998.

[47] N.Kaneda, Y.Qian and T. Itoh, "A broad-band microstrip-to-waveguide transition using quasi-Yagi antenna", IEEE Trans. Microwave Theory Tech., Vol.47, No.12, pp.2562-2567, Dec.1999.

[48] S.Thirakoune, A.Petosa, A.Ittipiboon and K.Levis, "Broadband printed dipole antennas", IEEE Int. Antennas Propagat. Symp. Digest, pp.52-55, July 2002.

[49] G. Zheng, A.A. Kishk, A.B.Yakovlev and A.W. Glisson, "Simplified feeding for a modified printed Yagi antenna", IEEE Int. Antennas Propagat. Symp. Digest, Vol.3, p.934-937, July 2003.

[50] G. Zheng, A.A. Kishk, A.W. Glisson, and A.B. Yakovlev, "Simplified feed for modified printed Yagi antenna", Electronics Letters, Volume 40, Issue 8, April 2004, pp. 464 – 466

[51] J.M.Floc'h, J.M.Denoual and K.Sallem, "Design of Printed Dipole with Reflector and Multi Directors", Proc. Loughborough Antennas and Propagation Conference, pp. 421-424, Nov.2009.

CHAPTER 3

Modified Array Theory Model of the Planar Holographic Antenna

3.1 INTRODUCTION

An approximate model for the planar holographic antenna using classical array theory provided useful information in [1]. It was evident there that, with the separation between the conducting arcs having to be λ, there are large pattern lobes in the endfire directions that are always present. These are of course grating lobes.

In this chapter we once again use an array theory model to study this phenomenon, but modify the model to account for the fact that the elements of the array model are actually parasitically excited. This modified array theory model will enable us to alter the element positions to examine whether the use of non-uniformly spaced elements might be able to reduce the level of the unwanted grating lobes. We will use this model with an optimization algorithm to automatically adjust the element positions of the elements, and the separation between the two levels (in the case of a double layer antenna) in order to maximize the directivity in the broadside direction.

The modified array theory model is described in Section 3.2. We define the optimization problem in Section 3.3. The optimization algorithm is exercised in Section 3.4, and the outcomes discussed. Section 3.5 concludes the chapter.

3.2 MODIFED ARRAY THEORY MODEL

3.2.1 Initial Remarks

We will use, as an approximate model for determining the radiation patterns of the holographic antenna in its one principal plane, the linear array theory based model shown in Figure 3.2-1. This is possible because of the left-right symmetry of the holographic antenna. The primary Yagi radiator is replaced by an isotropic source radiatior, and the conducting strips by parasitically-excited isotropic elements. Isotropic radiators are acceptable because the portions of the actual radiating features of the holographic antenna that contribute to the pattern in the said plane have omni-directional patterns in this plane. However, while the radiation patterns will be similar, we should not expect the absolute directivity values (in dBi) to be the same as those of the actual planar holographic antenna. We wish to perform optimisation of the directivity of the representative model by altering the locations of the isotropic radiators, and so an expression for this directivity must first be developed. In the coordinate system used, the broadside direction is $(\theta = 90^\circ, \phi = 90^\circ)$.

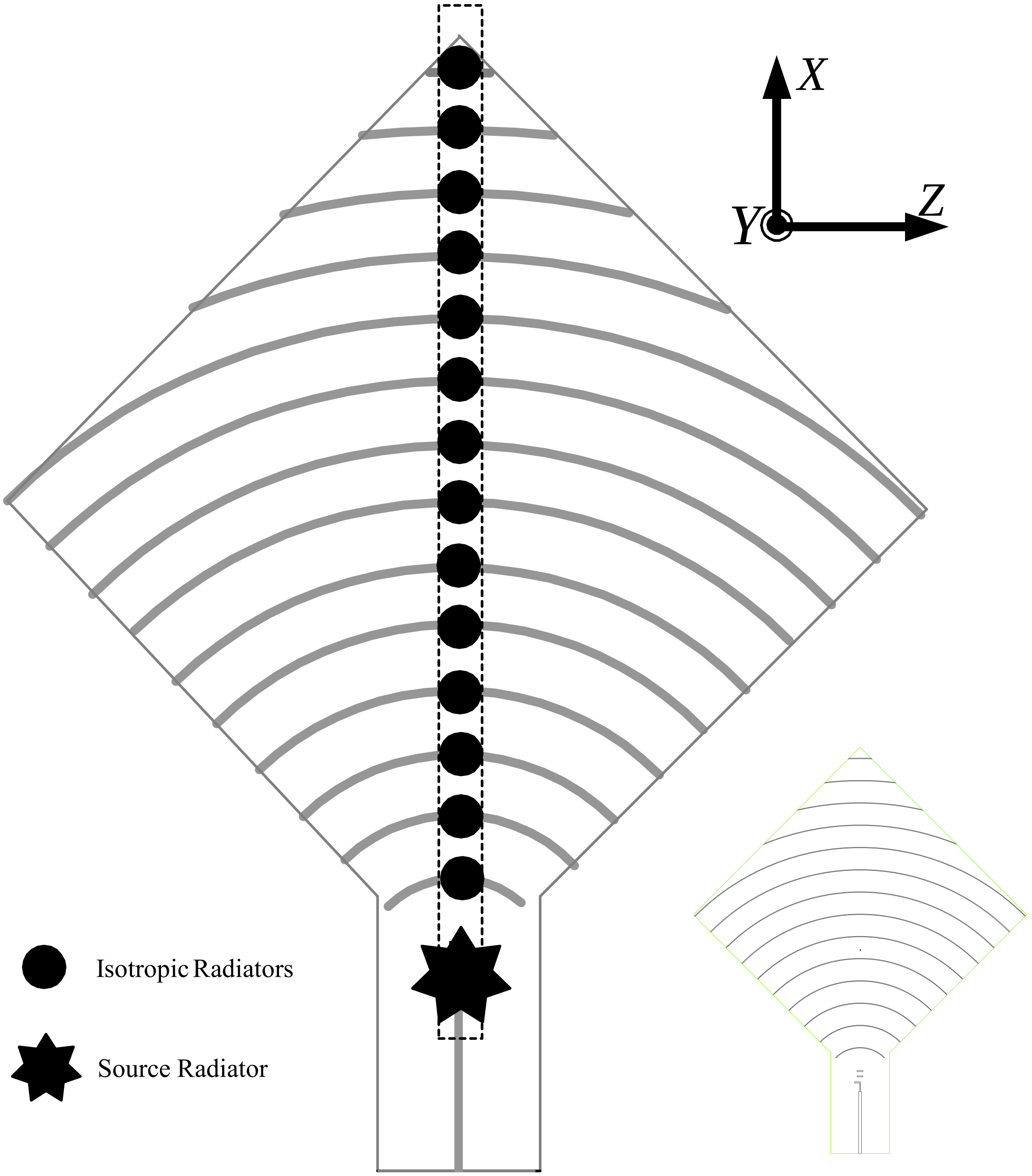

Figure 3.2-1 : Principal plane (xy-plane) approximate modelling of the Yagi-fed planar holographic antenna using a source plus isotropic radiators.

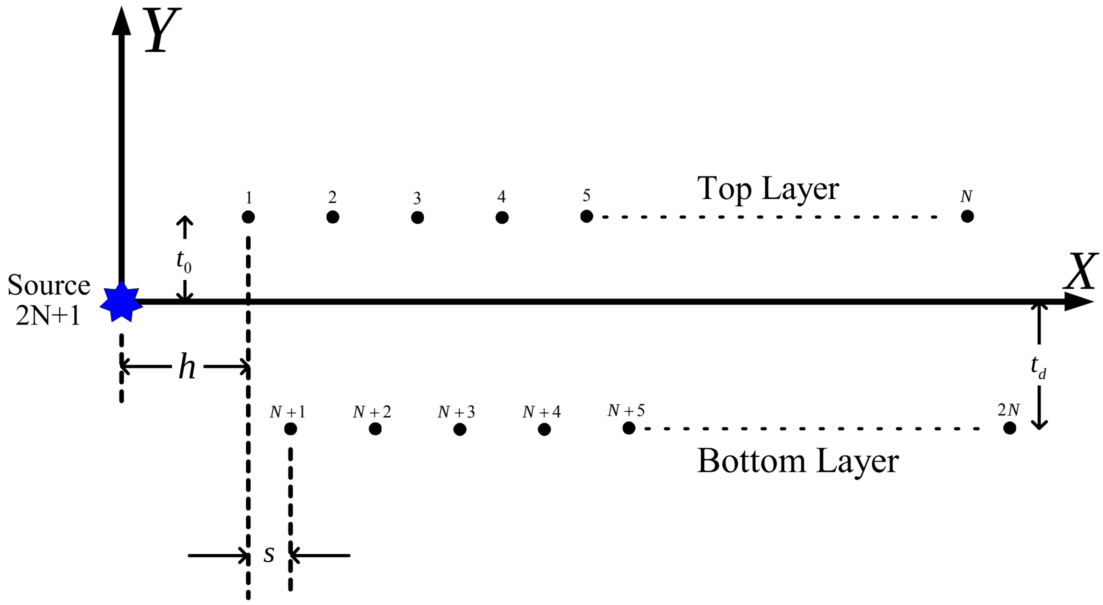

Figure 3.2-2 : Diagrammatic representation of the approximate model for the holographic antenna for principal plane (xy-plane) pattern computations.

3.2.2 Expressions for the Radiation Pattern

With reference to Figure 3.2-2, the radiation pattern of the array (including the source radiator) can be written as

$$U(\theta,\phi) = 1 + \sum_{n=1}^{2N} a_n e^{jkx_n \sin\theta\cos\phi} e^{jky_n \sin\theta\sin\phi} \tag{3.2-1}$$

which in the xy-plane cut where θ = 90° is

$$U(\phi) = 1 + \sum_{n=1}^{2N} a_n e^{jkx_n \cos\phi} e^{jky_n \sin\phi} \tag{3.2-2}$$

We now make the assumption that the amplitude and phase of the parasitically excited isotropic radiators can be found as

$$a_n = \frac{e^{-j\psi_n}}{r_n} \tag{3.2-3}$$

where

$$\psi_n = kr_n \tag{3.2-4}$$

and

$$r_n = \sqrt{x_n^2 + y_n^2 + z_n^2} \tag{3.2-5}$$

is the distance from the source radiator to the n-th parasitically excited radiator. Use of (3.2-3) represents a first order approximation in that the elements do not influence each other's excitation (which would be a second order approximation)

3.2.3 Expressions for the Directivity Pattern

An expression is given in [1,Eq.(7)] for the directivity of an array of elements (of the same orientation) located at any points $(x_n, y_n, z_n) = (r_n, \theta_n, \phi_n)$ in space. In the case of elements lying in a plane (in particular in the xy-plane) we have $\theta_n = 90^\circ$ and hence

$$x_n = r_n \cos\phi_n \tag{3.2-6}$$

and

$$y_n = r_n \sin\phi_n \tag{3.2-7}$$

The column vector $[F]$ in [1,Eq.(6)] then becomes (remembering that angles θ and ϕ are observation point angles, and are not the same as θ_n and ϕ_n)

$$[F(\theta,\phi)] = \begin{bmatrix} e^{-jkx_1 \sin\theta\cos\phi} e^{-jky_1 \sin\theta\sin\phi} \\ e^{-jkx_2 \sin\theta\cos\phi} e^{-jky_2 \sin\theta\sin\phi} \\ \bullet \\ \bullet \\ e^{-jkx_n \sin\theta\cos\phi} e^{-jky_n \sin\theta\sin\phi} \\ \bullet \\ \bullet \\ e^{-jkx_{2N} \sin\theta\cos\phi} e^{-jky_{2N} \sin\theta\sin\phi} \\ e^{-jkx_{2N+1} \sin\theta\cos\phi} e^{-jky_{2N+1} \sin\theta\sin\phi} \end{bmatrix} \tag{3.2-8}$$

We will always keep the location of the source, namely (x_{2N+1}, y_{2N+1}), fixed. In particular we will for convenience set $(x_{2N+1}, y_{2N+1}) = (0,0)$, so that $e^{-jkx_{2N+1}\sin\theta\cos\phi} e^{-jky_{2N+1}\sin\theta\sin\phi} = 1$. The expression for the elements of the $2N+1 \times 2N+1$ matrix $[B]$, whose general expression is provided in [2,Eq.(10)], becomes

$$b_{mn} = \frac{1}{4\pi} \int_0^{2\pi} \int_0^{\pi} g(\theta,\phi) e^{-jk(x_m - x_n)\sin\theta\cos\phi} e^{-jk(y_m - y_n)\sin\theta\sin\phi} \sin\theta d\theta d\phi \tag{3.2-9}$$

For the isotropic source assumption $g(\theta,\phi) = 1$, and the use of integrals given in [3] then allows (3.2-9) to be simplified to

$$b_{mn} = \begin{cases} \dfrac{\sin k\rho_{mn}}{k\rho_{mn}} & m \neq n \\ 1 & m = n \end{cases} \tag{3.2-10}$$

with

$$\rho_{mn} = \sqrt{(x_m - x_n)^2 + (y_m - y_n)^2} \tag{3.2-11}$$

The directivity in observation direction (θ,ϕ) can then be written as [2]

$$D(\theta,\phi) = \frac{[A]^T [F][F]^T [A]}{[A]^T [B][A]} \tag{3.2-12}$$

where

$$[A] = \begin{bmatrix} a_1 \\ a_2 \\ \cdot \\ \cdot \\ a_n \\ \cdot \\ \cdot \\ a_{2N} \end{bmatrix} \tag{3.2-13}$$

is a column vector of the complex excitations given in expression (3.2-3) for the modified array theory we are proposing here. Note that the order of the matrix multiplication in term $[F][F]^T$ leads to a $(2N+1)(2N+1)$ matrix. Furthermore, for observation points lying in the xy-plane we have observation angle $\theta = 90^\circ$ and this reduces further to

$$[F(90^\circ,\phi)] = \begin{bmatrix} e^{-jkx_1\cos\phi} e^{-jky_1\sin\phi} \\ e^{-jkx_2\cos\phi} e^{-jky_2\sin\phi} \\ \bullet \\ \bullet \\ e^{-jkx_n\cos\phi} e^{-jky_n\sin\phi} \\ \bullet \\ \bullet \\ e^{-jkx_{2N}\cos\phi} e^{-jky_{2N}\sin\phi} \\ e^{-jkx_{2N+1}\cos\phi} e^{-jky_{2N+1}\sin\phi} \end{bmatrix} \qquad (3.2\text{-}14)$$

3.3 DEFINITION OF THE NON-UNIFORMLY SPACED ARRAY OPTIMISATION PROBLEM

3.3.1 The Objective Function

Using optimisation variables $\{x_1, x_2, ..., x_{2N}, t_o, t_d\}$, maximize the objective function

$$F_{obj}(x_1, x_2, ..., x_{2N}, y_1, y_2, ..., y_{2N}) = D(\theta = 90^\circ, \phi = 90^\circ) \qquad (3.3\text{-}1)$$

3.3.2 Starting Values of (x_n, y_n, z_n) for the Optimisation Problem

$$x_n^{start} = \begin{cases} h + (n-1)d & n = 1, 2, ..., N \\ h + s + (n - N - 1)d & n = N+1, N+2, ..., 2N \end{cases} \qquad (3.3\text{-}2)$$

$$y_n^{start} = \begin{cases} t_0 & n = 1, 2, ..., N \\ -t_d & n = N+1, N+2, ..., 2N \end{cases} \qquad (3.3\text{-}3)$$

$$z_n = 0 \quad \forall n \qquad (3.3\text{-}4)$$

With non-uniformly spaced elements there is no fixed inter-element spacing d between adjacent elements. However, a selected value of d is assumed (eg. $d = \lambda_0$) at the start of any optimization run to provide the starting values of (x_n, y_n, z_n).

3.3.3 Constraints for the Optimisation Problem

In each of the levels of elements, each element's x-position must be greater than that to the right of it. Thus we require[5]

$$\begin{aligned} x_{n+1} &\geq x_n \qquad n = 1, 2, \ldots.., N \\ x_{n+1} &\geq x_n \qquad n = N+1, N+2, \ldots.., 2N \end{aligned} \tag{3.3-5}$$

Since the set of elements on the bottom layer are shifted slightly to the right, we need

$$x_{2N+1} \geq x_1 \tag{3.3-6}$$

We do not want any of the elements to be to the left of the source, and so we require

$$x_n \geq 10^{-3} \qquad \forall n \tag{3.3-7}$$

3.3.4 Numerical Optimisation Routine

We use the Matlab [4] routine *fmincon* which implements a constrained nonlinear programming algorithm. It allows *simple bound constraints* of the form

$$x_n^{lower} \leq x_n \leq x_n^{upper} \tag{3.3-8}$$

as well as more *complicated linear constraints* that can be expressed in the form

$$[A][X] \leq [P] \tag{3.3-9}$$

where the column vector $[X]$ is, in the present case

---

[5] Although the constraint is written to allow for each element to have the same x position, in reality each element's x-position must be greater than that to the right of it. With the use of $x_1 - x_2 \leq 10^{-3}$ one can ensure that two elements close together may be only as close as 10^{-3}. This is done to satisfy the *fmincon* function set up in Matlab.

$$[X]=\left[\begin{array}{c} x_1 \\ \bullet \\ x_n \\ \bullet \\ \bullet \\ x_{2N} \\ \hline t_o \\ t_d \end{array}\right] \qquad (3.3\text{-}10)$$

We will use both types of constraints to implement those described in expressions (3.3-8) through (3.3-9).

As regards the simple bound constraints we select

$$x_n^{start} - \tau d \le x_n \le x_n^{start} + \tau d \qquad (3.3\text{-}11)$$

with $\tau = 0.95$ for $n \le 2N$. This limits the movement of any element to within 95% of its original location in either direction. Bounds must also be placed on t_o and t_d, as we here use

$$0 \le t_o \le \lambda / 2 \qquad (3.3\text{-}12)$$

and

$$-\lambda / 2 \le t_d \le 0 \qquad (3.3\text{-}13)$$

This allows quite a large amount of change in the separation between the layers and so will not overly restrict the optimization process. The implementation of the more complicated inequality constraints is best illustrated via an example for which N = 6. Then the optimization variables are x_1, x_2, x_3, x_4, x_5, x_6, t_o and t_d. We would then require

$$
\begin{aligned}
-x_1 &\le 10^{-3} \\
-x_2 &\le 10^{-3} \\
-x_3 &\le 10^{-3} \\
-x_4 &\le 10^{-3} \\
-x_5 &\le 10^{-3} \\
-x_6 &\le 10^{-3} \\
x_1 - x_2 &\le 10^{-3} \\
x_2 - x_3 &\le 10^{-3} \\
x_1 - x_4 &\le -s \\
x_4 - x_5 &\le 10^{-3} \\
x_5 - x_6 &\le 10^{-3} \\
t_o &\le 0.03 \\
t_d &\le 0
\end{aligned}
\tag{3.3-14}
$$

In the above-mentioned matrix format this becomes

$$
\left[\begin{array}{cccccc:cc}
-1 & 0 & 0 & 0 & 0 & 0 & 0 & 0 \\
0 & -1 & 0 & 0 & 0 & 0 & 0 & 0 \\
0 & 0 & -1 & 0 & 0 & 0 & 0 & 0 \\
0 & 0 & 0 & -1 & 0 & 0 & 0 & 0 \\
0 & 0 & 0 & 0 & -1 & 0 & 0 & 0 \\
0 & 0 & 0 & 0 & 0 & -1 & 0 & 0 \\
\hdashline
1 & -1 & 0 & 0 & 0 & 0 & 0 & 0 \\
0 & 1 & -1 & 0 & 0 & 0 & 0 & 0 \\
1 & 0 & 0 & -1 & 0 & 0 & 0 & 0 \\
0 & 0 & 0 & 1 & -1 & 0 & 0 & 0 \\
0 & 0 & 0 & 0 & 1 & -1 & 0 & 0 \\
\hdashline
0 & 0 & 0 & 0 & 0 & 0 & 1 & 0 \\
0 & 0 & 0 & 0 & 0 & 0 & 0 & 1
\end{array}\right]
\begin{bmatrix} x_1 \\ x_2 \\ x_3 \\ x_4 \\ x_5 \\ x_6 \\ t_o \\ t_d \end{bmatrix}
=
\begin{bmatrix} 10^{-3} \\ 10^{-3} \\ 10^{-3} \\ 10^{-3} \\ 10^{-3} \\ 10^{-3} \\ 10^{-3} \\ 10^{-3} \\ -s \\ 10^{-3} \\ 10^{-3} \\ 0.03 \\ 0 \end{bmatrix}
\tag{3.3-15}
$$

The above bounds translate our practical requirements (namely we simply wish to adjust the element locations to see if some directivity improvement is possible) into a mathematical form that prevents the optimization algorithm from providing unintended solutions.

The stopping conditions determine whether the optimizer has found a local minimum. In order to do this a constraint and step size tolerance is set. By default the tolerance on the constraint violation is e^{-6} and the step size tolerance's default value is e^{-10}. To really be sure that the optimum value was being achieved both tolerances were set to e^{-20}.

3.4 OUTCOMES OF THE ARRAY OPTIMISATION STUDY

3.4.1 Optimiser Starting Values

We set $s = \lambda/4$ and $h = \lambda$. Quantities s and h are not in the set of optimisation variables and so are not altered by the optimisation algorithm. We have used N=14 elements in all cases illustrated; use of more or fewer elements does not reveal anything new or alter the conclusions in any way. The starting values for the optimisation variables are all determined by setting with $t_0 = \lambda/4$, $t_d = \lambda/4$ and $d = \lambda$. In all the discussion that follows when we refer to "optimized directivity" we will imply the directivity in the $(\theta = 90^\circ, \phi = 90^\circ)$ direction, unless specifically stated otherwise. Also note that when we write "optimized result" we simply mean the result that is obtruded by the optimisation algorithm. The results presented are a sampling of copious sets of optimisation runs that are representative of observed trends, and which illustrate the conclusions drawn from the aforementioned numerical experiments.

3.4.2 Single-Layer Array

We first exercised the modified array theory based optimisation procedure using a single layer of elements. Figure 3.4-1 shows the starting situation (with $s = \lambda/4$, $h = \lambda$ and $d = \lambda$) before any optimisation has been performed. It is only for an inter-element spacing $d = \lambda$ that all elements of the uniformly spaced starting array are in phase. It is also due to this large required spacing that we have the undesirable grating lobes at $\phi = 0^\circ$ and $\phi = 180^\circ$. Using these starting values, the optimisation to maximize $D(\theta = 90^\circ, \phi = 90^\circ)$ provides the solution shown in Figure 3.4-2. This directivity is now slightly higher, and was obtained by the optimisation routine by moving the source away form the parasitic elements, with the locations of the parasitic elements largely unchanged. The unwanted grating lobes are still present, although one is now slightly lower, which is what resulted in the increase in $D(\theta = 90^\circ, \phi = 90^\circ)$. If we use the starting situation $s = \lambda / 4$, $h = \lambda$ and d = 3λ/4, we obtain the optimisation result in Figure 3.4-3. The parasitic elements are no longer uniformly spaced. The grating lobe centred around $(\theta = 90^\circ, \phi = 180^\circ)$ is now considerably lower, but the broadside directivity $D(\theta = 90^\circ, \phi = 90^\circ)$ has decreased form that in previous figures. This is not what we want, and shows the hazards of using general non-linear optimisation in antenna synthesis, namely its dependence on the starting point and the possibility of being "caught in a trap" such as that in Figure 3.4-3. However, for the results present here we have experimented with very many starting situations, and the results presented (used to reach the conclusions in Section 3.5) are based on the best results so obtained. Before proceeding to Section 3.4.3, where we will study double-layer cases, we show one final single-layer result where we have maximized $D(\theta = 90^\circ, \phi = 80^\circ)$, the directivity slightly off broadside, instead of the broadside directivity $D(\theta = 90^\circ, \phi = 90^\circ)$. Using starting situation the starting situation (with $s = \lambda / 4$, $h = \lambda$ and d = λ) we obtain the optimized result in Figure 3.4-4. One grating lobe is still present, and the directivity is no higher than for the broadside case.

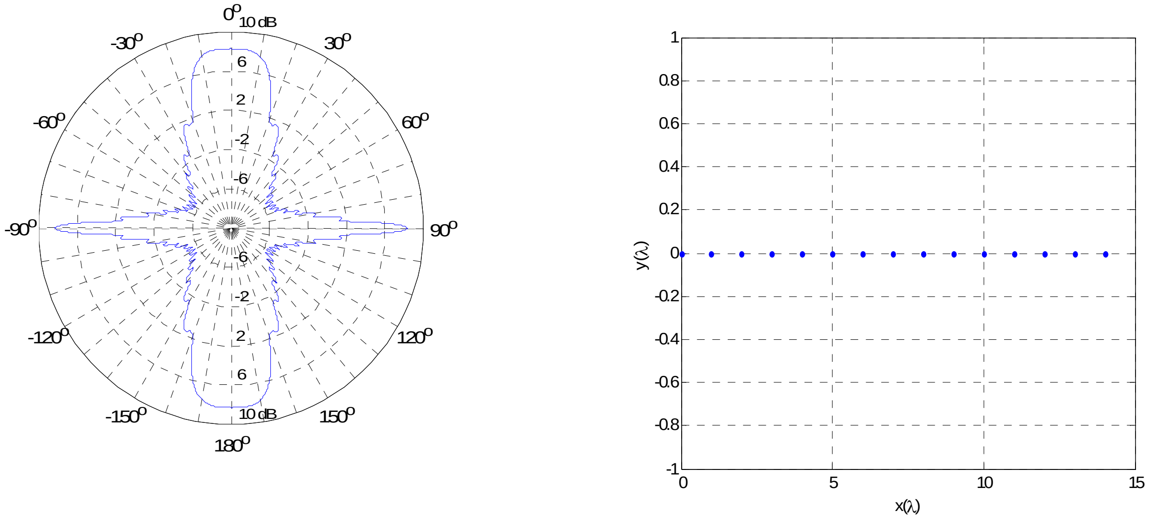

(a) **(b)**

Figure 3.4-1 : (a). Directivity pattern for an array of N=14 elements, plus the source element, with h = λ and d = λ, before optimisation, and (b). location of source element and parasitic elements.

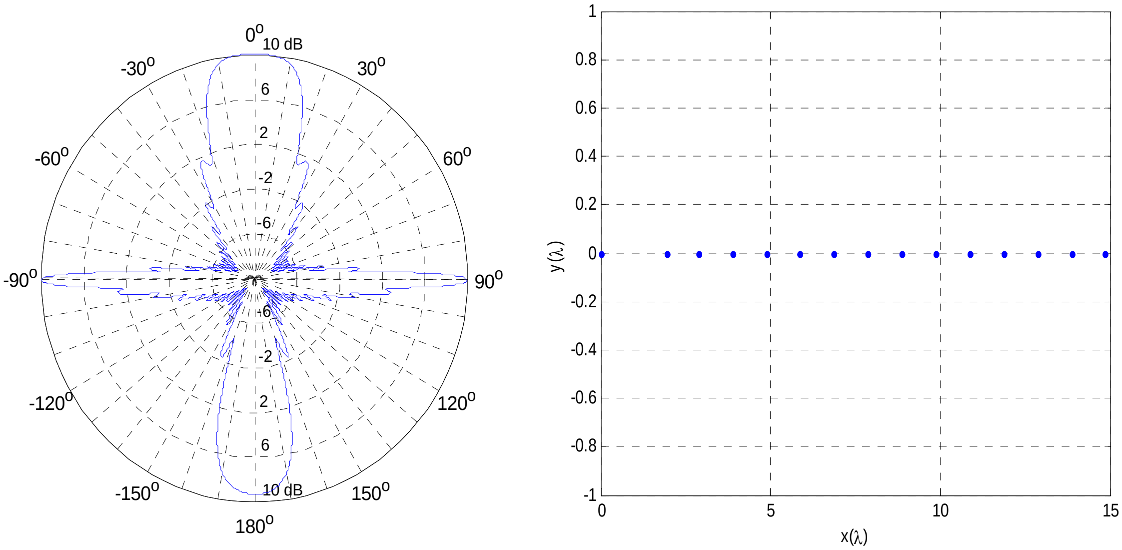

(a) **(b)**

Figure 3.4-2 : (a). Directivity pattern after optimisation for an array of N=14 elements plus the source, with starting situation $s = \lambda/4$, $h = \lambda$ and d = λ, and (b). location of source element and parasitic elements.

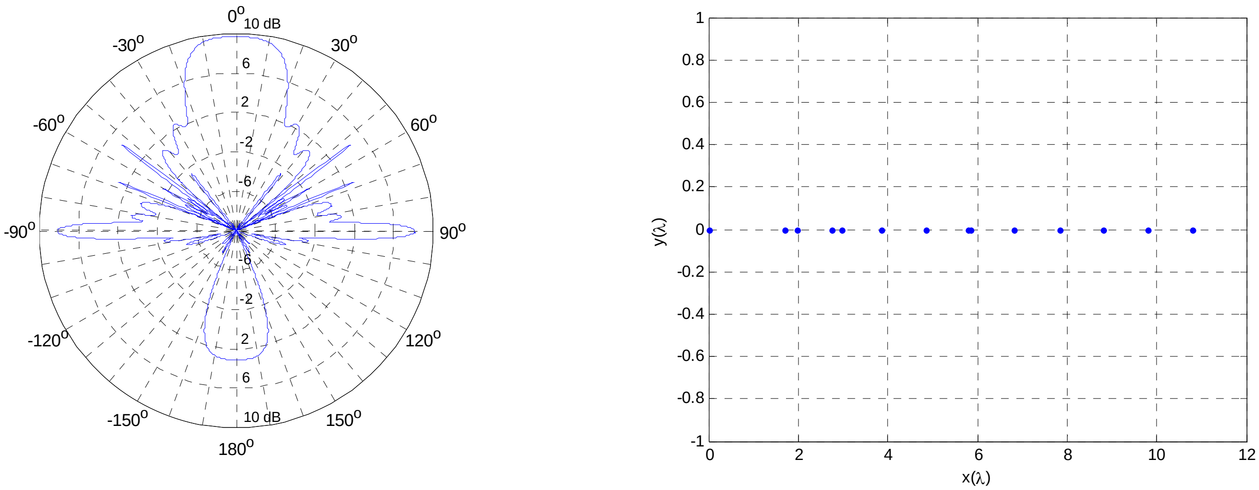

(a) **(b)**

Figure 3.4-3 : (a). Directivity pattern after optimisation for an array of N=14 elements plus the source, with starting situation $s = \lambda/4$, $h = \lambda$ and d = 3λ/4, and (b). location of source element and parasitic elements.

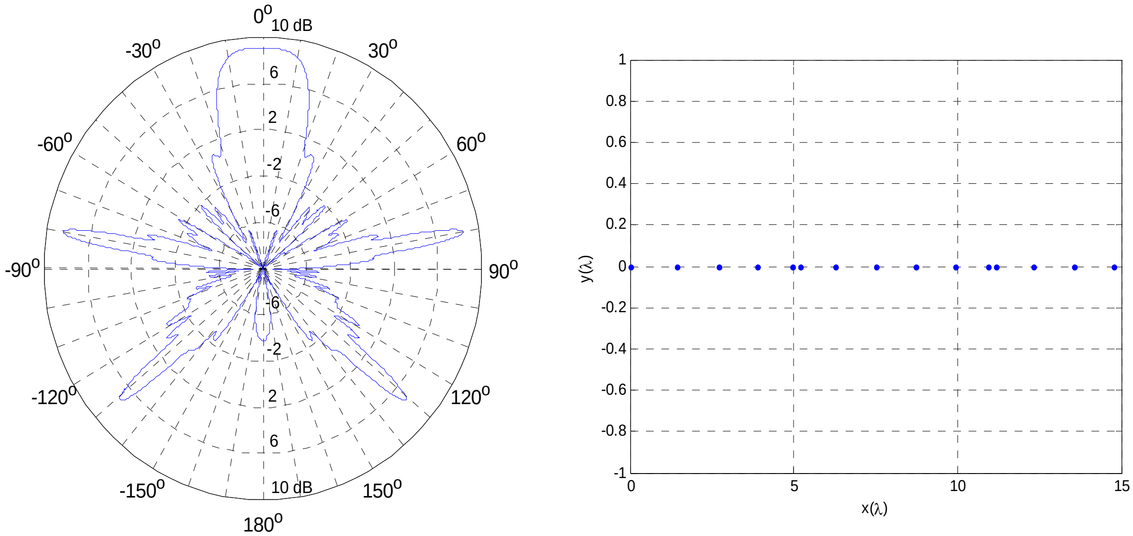

(a) **(b)**

Figure 3.4-4 : (a). Directivity pattern after optimisation for an array of N=14 elements, plus the source element, for starting situation h = λ and d = λ, and (b). location of source element and parasitic elements. In this particular case the directivity was maximized in direction $(\theta = 90^\circ, \phi = 80^\circ)$ **, which is** 10° **off broadside.**

3.4.3 Double-Layer Array

The starting situation was $s = \lambda/4$, $h = \lambda$, d = λ, $t_o = 0.125\lambda$ and $t_d = -0.125\lambda$. The elements on the bottom layer are shifted with respect to the top layer by a quarter wavelength (s = 0.25λ), and the spacing between the two arrays is quarter wavelength as well ($t_o + t_d = 0.25\lambda$). The phases of each element should be such as to contribute to a directivity maximum in the $(\theta = 90^\circ, \phi = 90^\circ)$ direction. Figure 3.4-5 shows the directivity (maximum value about 11 dBi) of this starting situation prior to optimisation. There is indeed a single broadside lobe[6], but an unwanted grating lobe is still present. The only reason that the second grating lobe centred around $(\theta = 90^\circ, \phi = 180^\circ)$ has been suppressed is the presence of the source contribution. With the above starting values the

---

[6] Here the broadside lobe is actually in the $\phi = -90^\circ$ direction and not the desired $\phi = 90^\circ$ direction. This can easily be remedied by making s = -λ/4.

optimisation procedure provides the result in Figure 3.4-6. The parasitic elements are no longer uniformly spaced. Indeed, the locations on the bottom layer are no longer simply those of the top layer shifted by a fixed amount, although the first elements on each layer are still shifted about λ/4 with respect to each other along the x-axis. The separation between the layers has been increased from the starting value of λ/4 to 1.3 λ, which would in practice be a rather thick substrate. The source is no longer located between the top and bottom layers. There is now a maximum directivity of roughly 13 dBi (a 2dB improvement on the starting value in Figure 3.4-5), but the sidelobe structure remains unattractive.

When the starting situation is changed to $s = \lambda / 4$, $h = 4.24\lambda$ (this source-to-element separation is the only change from the above case), d = λ, t_o = 0.125λ and t_d = -0.125λ, we obtain the optimised result of Figure 3.4-8. It is a geometry that is different from that in Figure 3.4-6, but the maximum value of $D(\theta = 90^\circ, \phi = 90^\circ)$ is always about 13dBi. Other starting points provide slightly altered geometries but never a value of $D(\theta = 90^\circ, \phi = 90^\circ)$ more than about 13dBi or greatly improved sidelobe structure. As a sanity check we once again requested that $D(\theta = 90^\circ, \phi = 80^\circ)$ be maximized instead of the broadside directivity, and obtained the result in Figure 3.4-9. This was repeated for several different values of ϕ. In an attempt to force the sidelobes lower we used the objective function

$$D(\theta = 90^\circ, \phi = 90^\circ) - D(\theta = 90^\circ, \phi = 180^\circ) - D(\theta = 90^\circ, \phi = 0^\circ) - D(\theta = 90^\circ, \phi = -90^\circ) \qquad (3.4\text{-}1)$$

However this caused the optimizer to give a result in Figure 3.4-10. The directivities in the directions $(\theta = 90^\circ, \phi = 180^\circ)$, $(\theta = 90^\circ, \phi = 0^\circ)$ and $(\theta = 90^\circ, \phi = -90^\circ)$ have been lowered by there being deep nulls steered to these directions. However, the sidelobe structure has not been lower overall, since there are still large lobes around these null directions, and (more importantly) the desired main lobe directivity $D(\theta = 90^\circ, \phi = 90^\circ)$ has been significantly lowered; in fact it is difficult to identify a "main" lobe.

The cases we have described are illustrative of what we have observed in copious other numerical experiments. It is clear that the physics simply does not allow the grating lobes to be suppressed in some "natural" way in the configuration chosen (which is an approximate model of the planar holographic antenna). This will always limit the directivity and sidelobe structure that can be obtained.

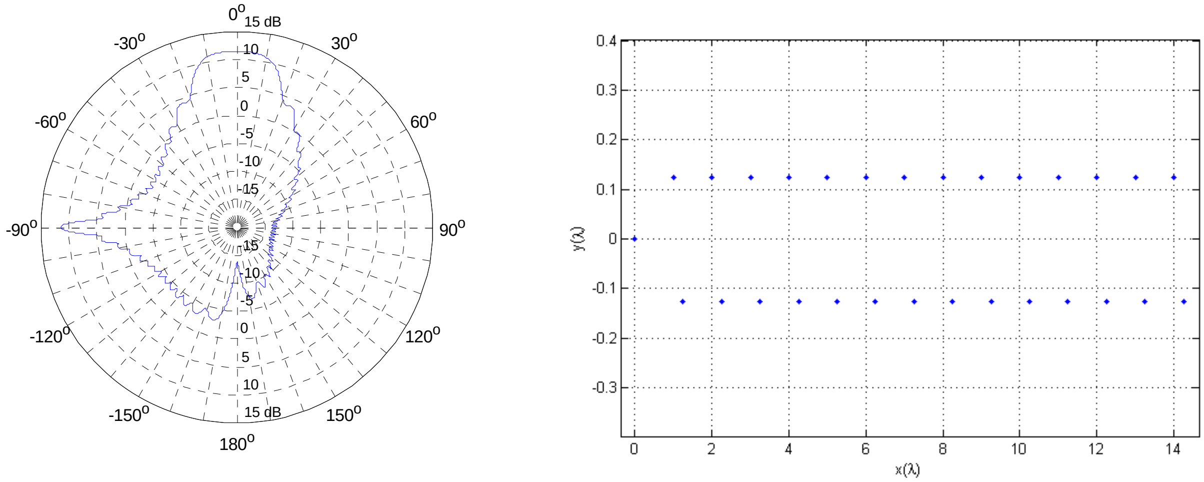

(a) **(b)**

Figure 3.4-5 : (a). Directivity pattern for a double-layer array of 28 elements, plus the source element, with $s = \lambda / 4$, $h = \lambda$, d = λ, t_o = 0.125λ and t_d = -0.125λ**, before optimisation, and (b). location of source element and parasitic elements.**

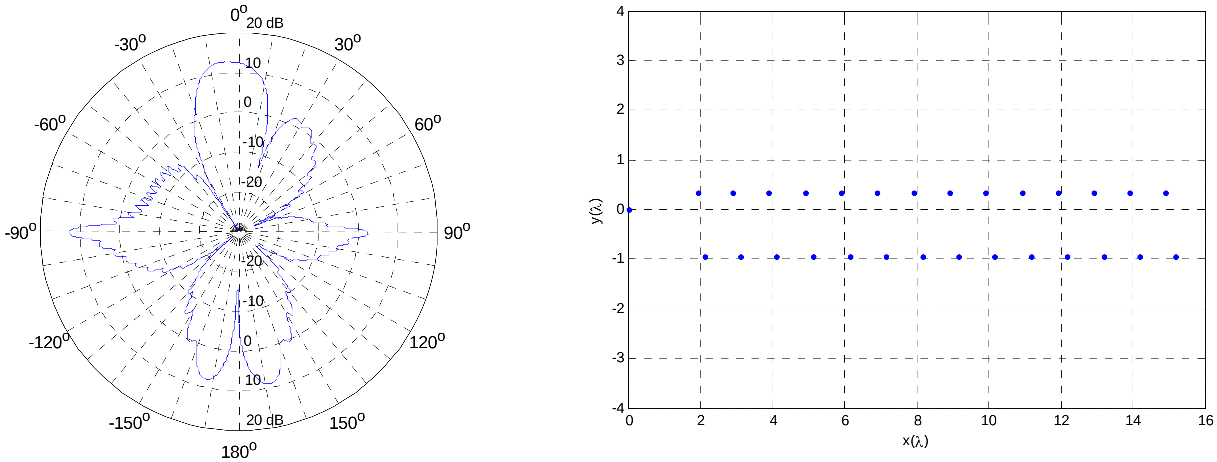

(a) **(b)**

Figure 3.4-6 : (a). Directivity pattern after maximization of D (θ = -90° ϕ = 90°) for a double-layer array of 28 elements, plus the source element, with starting situation $s = \lambda / 4$, $h = \lambda$, d = λ, t_o = 0.125λ **and** t_d = -0.125λ**, and (b). location of source element and parasitic elements.**

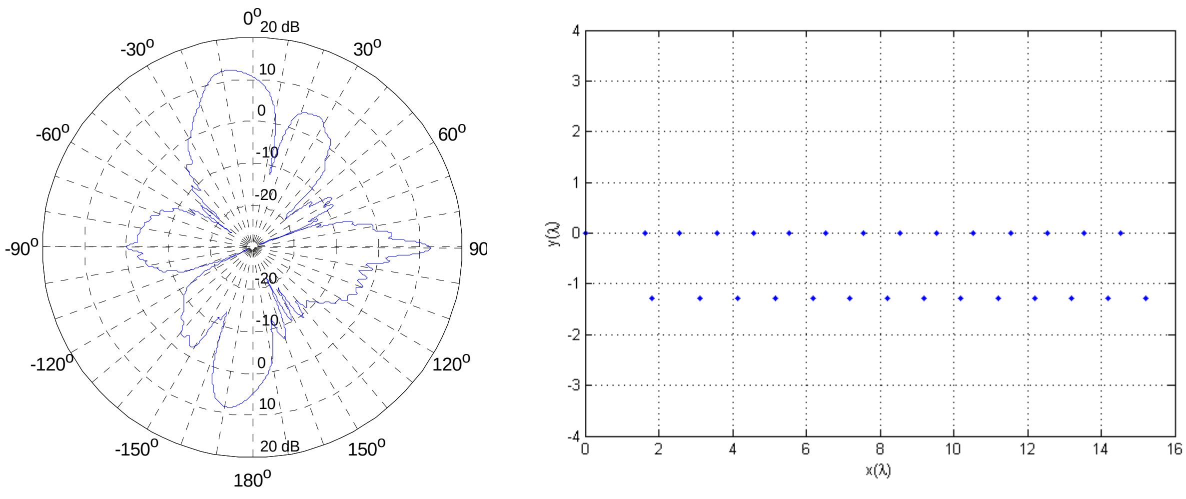

(a) **(b)**

Figure 3.4-7 : (a). Directivity pattern after maximization of D (θ = 90° ϕ = 90°) for a double-layer array of 28 elements, plus the source element, with starting situation $s = \lambda / 4$, $h = \lambda$, d = λ, $t_o = 0.125\lambda$ **and** $t_d = -0.125\lambda$**, and (b). location of source element and parasitic elements.**

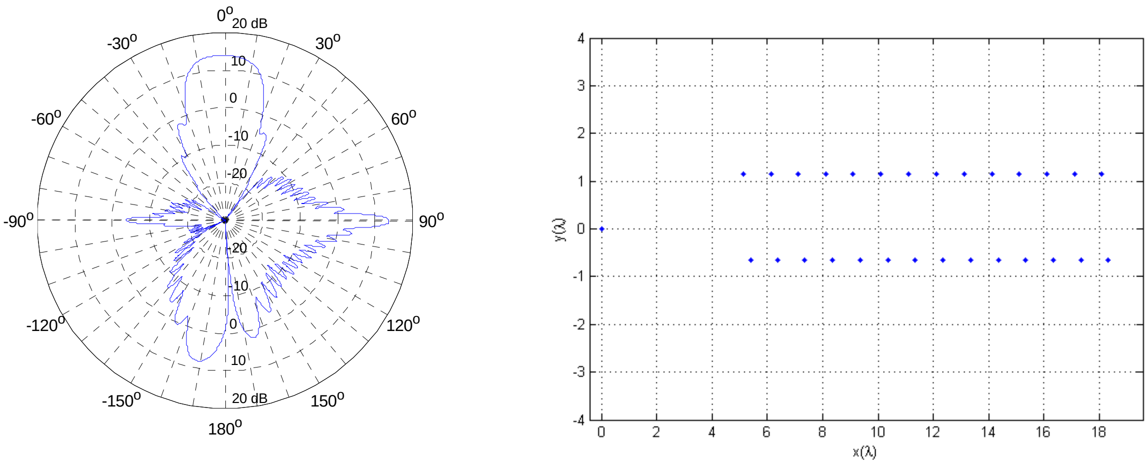

(a) **(b)**

Figure 3.4-8 : (a). Directivity pattern after optimisation for a double-layer array of 28 elements, plus the source element, with starting situation $s = \lambda / 4$, $h = 4.24\lambda$, d = λ, $t_o = 0.125\lambda$ **and** $t_d = -0.125\lambda$**, and (b). location of source element and parasitic elements.**

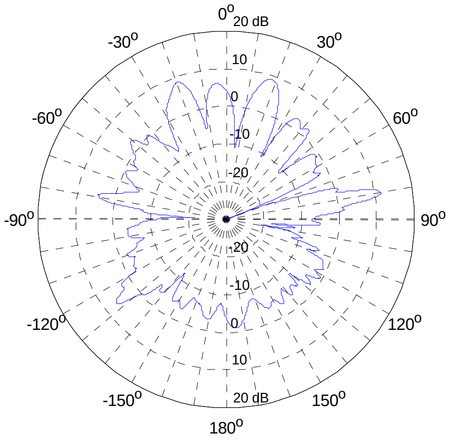

Figure 3.4-9 : Directivity pattern after optimisation for a double-layer array of 28 elements, plus the source element, with starting situation $s = \lambda / 4$, $h = \lambda$, $d = \lambda$, $t_o = 0.125\lambda$ **and** $t_d = -0.125\lambda$**. In this particular case the directivity was maximized in direction** $(\theta = 90^\circ, \phi = 80^\circ)$**, which is** 10° **off broadside.**

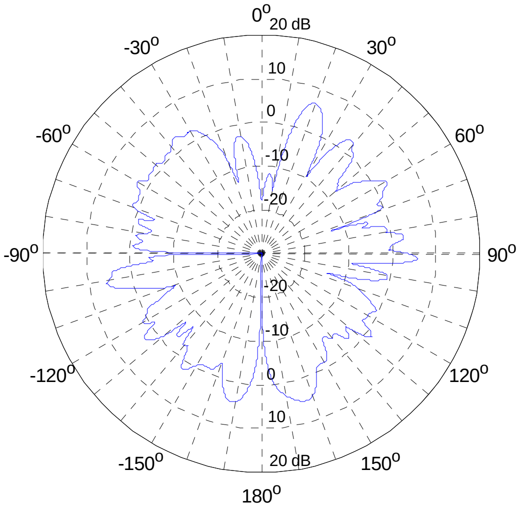

Figure 3.4-10: Directivity pattern after optimisation for a double-layer array of 28 elements, plus the source element, with starting situation $s = \lambda / 4$, $h = \lambda$, $d = \lambda$, $t_o = 0.125\lambda$ **and** $t_d = -0.125\lambda$**. In this particular case the objective function was that in expression (3.4-1).**

3.5 CONCLUDING REMARKS

Several things have been established by the work of this chapter. Most important is the fact that it is not possible, for the planar holographic antenna under consideration in this thesis, to maximize the broadside directivity *and* get rid of both of the grating (endfire) lobes at the fundamental level by destroying the periodicity of the structure. It might be possible to reduce it (that is, obtain a "partial fix") because of the presence of the substrate and other details of a particular implementation (eg. blockage by the feed radiator, as we will see in Chapter 5), but it will always be latent. It is a major stumbling block to improvement of the overall efficiency (and hence directivity) of this type of antenna.

3.6 REFERENCES FOR CHAPTER 3

[1] K.Levis, “Ka-Band Holographic Antennas”, MASc Thesis, University of Ottawa, Ottawa, ON, Canada, 1999.

[2] D.K.Cheng, "Optimization techniques for antenna arrays", Proc. IEEE, Vol.59, No.12, pp.1664-1674, Dec.1971.

[3] D.K.Cheng & F.I.Tseng, "Maximisation of directive gain for circular and elliptical arrays", Proc. IEE (London), Vol.114, No.5, pp.589-594, May 1967.

[4] *MATLAB*^{TM} is a trademark of The MathWorks Inc., USA.

CHAPTER 4

Computational Electromagnetic Modelling of the Planar Holographic Antenna

4.1 INTRODUCTION

We usually think of reflector antenna operation in terms of geometrical optics principles, but then when such antennas are to be designed it is necessary to perform a far more detailed electromagnetic analysis if high performance is to be achieved. Such analysis allows one to determine important quantities such as directivity, sidelobe levels, cross-polarisation levels, and to use such an analysis to optimize designs. The same situation can be thought to exist for the planar holographic antenna design[7]. In Chapter 2 we described how such planar holographic antennas are made by placing conducting tracks at the minima of interference patterns produced by the superposition of an ideal spherical wave source and a plane wave source. In order to improve the performance of planar holographic antennas a more detailed electromagnetic analysis is needed. Up to the present time a comprehensive study using full three-dimensional electromagnetic analysis has not been done. In this thesis we will use both the method of moments (MoM) as implemented in the code FEKO [1], and the finite-difference time-domain (FDTD) technique as implemented in the software package EMPIRE™ [2], to electromagnetically model aspects of the planar holographic antenna. Although the MoM and FDTD are probably well-known to the reader it will be worthwhile describing some specific features of each that will be important to their use for the problem at hand and which may differ from one implementation to another of the same technique. Section 4.2 describes the essentials of the two methods. The use of FEKO is the subject of Section 4.3. The code EMPIRE's utilisation is discussed in Section 4.4. The chapter is concluded by Section 4.5. Unless otherwise stated, all the work is done on planar holographic antennas designed for a centre frequency of 30 GHz. Implementation details of the above-mentioned commercial codes are such that we will not be able to use precisely the same coordinate system orientation throughout the thesis; we will of course always indicate which specific orientation is being used.

---

[7] Recall that we are interested in the type without a groundplane present, as explained in Sections 2.3 and 2.4.

4.2 COMPUTATIONAL ELECTROMAGNETICS MODELS USED

4.2.1 Essentials of the Method of Moments

There are two important equivalence theorems used in electromagnetic theory, namely the surface equivalence principle and the volume equivalence principle. If we want to solve (that is, finds the fields due to) a problem that consists of conducting and dielectric objects illuminated by some impressed source which generates some known incident field $\bar{E}_{inc}$, then [3]

- The surface equivalence principle enables us to replace perfectly conducting surfaces by equivalent electric surface current densities $\bar{J}_s^{eq}$ on these surfaces (with the actual conductors removed).
- The volume equivalence principle allows us to replace the volumetric dielectric objects by equivalent volume current densities $\bar{J}_v^{eq}$ in these volumes (with the actual dielectric material removed).

The equivalent current densities $\bar{J}_s^{eq}$ and $\bar{J}_v^{eq}$ are not yet known. However, knowledge of the free space Green's function allows us to write down expressions for the fields (call these the scattered fields $\bar{E}_{scat}$) due to these unknown current densities in the form of integrals taken over the above-mentioned surfaces and volumes, with the unknown current densities and the Green's function inside the integral. The total field everywhere $\bar{E}_{total}$ is the sum of the incident and scattered fields $\bar{E}_{total} = \bar{E}_{inc} + \bar{E}_{scat}$. We know that on the surfaces originally occupied by the conductors the tangential component of the total field must be zero. If we enforce this the previously mentioned integrals become integral equations for the unknown current densities $\bar{J}_s^{eq}$ and $\bar{J}_v^{eq}$.

The method of moments is used to solve such integral equations numerically. It is best illustrated using a one-dimensional case [4]. Suppose we have an unknown function $f(z)$ of a real spatial variable z, which would correspond to the above $\bar{J}_s^{eq}$ and $\bar{J}_v^{eq}$. The function $f(z)$ exists only for those values of z in the interval $z_L \le z \le z_U$, a region that would correspond to the surfaces and volumes originally occupied by the conducting and dielectric material above. Also suppose we have a known function $g(z)$, corresponding to the known $\bar{E}_{inc}$ above. Now consider the problem of finding an *unknown* function $f(z)$ defined over the interval $z_L \le z \le z_U$, and which must satisfy the equation

$$\int_{z_L}^{z_U} f(z')\,G(z,z')\,dz' = g(z) \qquad z_L \le z \le z_U \tag{4.2-1}$$

This corresponds to the integral equations mentioned above, and the qualifier $z_L \le z \le z_U$ is necessary since the integral equation applies only at points originally occupied by the conducting material surface where it was possible to enforce the boundary condition on the tangential electric field. The function $G(z,z')$ corresponds to the Green's function in the electromagnetics problem. In such equations we need to be able to evaluate $f(z)$ and $g(z)$ at different z values in the same equation. Thus we need to use the primed and unprimed notation, with $z_L \le z' \le z_U$ also. Note that the integration is with respect to z'.

In order to find an approximate solution for $f(z)$ we first expand $f(z)$ in terms of some selected (and hence *known*) *expansion functions* $f_n(z)$, N of them in total, as

$$f(z) \approx \sum_{n=1}^{N} a_n\, f_n(z) \tag{4.2-2}$$

Since $f(z)$ is the unknown, the coefficients a_n, n = 1,2,....,N are of course unknown at this stage. The “unknown-ness” has been transferred to these coefficients. The aim is to utilise the method of moments to determine them.

If we substitute the series (4.2-2) into the original integral equation (4.2-1) we get

$$\int_{z_L}^{z_U} \left(\sum_{n=1}^{N} a_n\, f_n(z') \right) G(z,z')\,dz' \approx g(z) \tag{4.2-3}$$

The linearity of the integral operation next allows us to move the summation from under the integral sign, giving

$$\sum_{n=1}^{N} a_n \left(\int_{z_L}^{z_U} f_n(z')\,G(z,z')\,dz' \right) = g(z) \tag{4.2-4}$$

which we can write as

$$\sum_{n=1}^{N} a_n \Psi_n(z) = g(z) \tag{4.2-5}$$

if we define

$$\Psi_n(z) = \int_{z_L}^{z_U} f_n(z') G(z,z')\, dz' \tag{4.2-6}$$

Since the $f_n(z')$ are known expansion functions, the integrals for the z-dependent function $\Psi_n(z)$ can be evaluated numerically for any value of z.

We next select a second set of N functions $\{g_1(z), g_2(z), ..., g_m(z), ..., g_N(z)\}$. We need to select them and thus they are *known*. These are conventionally called the *weighting* or *testing* functions. We can then multiply both sides of (4.2-5) by *each* of these weighting functions *in turn*, each time integrating the products on the left and right hand sides with respect to z (as opposed to with respect to z') over the interval $z_L \le z \le z_U$. This process yields

$$\sum_{n=1}^{N} a_n \left(\int_{z_L}^{z_U} \Psi_n(z)\, g_m(z)\, dz \right) = \int_{z_L}^{z_U} g(z)\, g_m(z)\, dz \qquad m = 1, 2, ..., N \tag{4.2-7}$$

where $m = 1, 2, ..., N$ indicates that (4.2-7) holds for each m in turn.

We can tidy up our notation so as not to obscure the essentials by letting (note the order of the subscripts carefully)

$$Z_{mn} = \int_{z_L}^{z_U} \Psi_n(z)\, g_m(z)\, dz \tag{4.2-8}$$

and

$$b_m = \int_{z_L}^{z_U} g(z)\, g_m(z)\, dz \tag{4.2-9}$$

so that the set of linear equations represented by (4.2-7) can be written in matrix notation as

$$[Z]\,[I]=[V] \tag{4.2-10}$$

where the *known* moment method matrix (usually called the impedance matrix when applying the method of moments to electromagnetics problems, since it has the units of impedance)

$$[Z]=\begin{bmatrix} Z_{11} & Z_{12} & \cdot & \cdot & Z_{1N} \\ Z_{21} & Z_{22} & \cdot & \cdot & Z_{2N} \\ \cdot & \cdot & \cdot & \cdot & \cdot \\ \cdot & \cdot & \cdot & \cdot & \cdot \\ Z_{N1} & Z_{N2} & \cdot & \cdot & Z_{NN} \end{bmatrix} \tag{4.2-11}$$

The *known* column matrix (also referred to as the excitation matrix)

$$[V]=\begin{bmatrix} b_1 \\ b_2 \\ \cdot \\ \cdot \\ b_N \end{bmatrix} \tag{4.2-12}$$

while the column matrix

$$[I]=\begin{bmatrix} a_1 \\ a_2 \\ \cdot \\ \cdot \\ a_N \end{bmatrix} \tag{4.2-13}$$

is the matrix of *unknown* coefficients. Solution of the matrix equation (4.2-10) then yields [I], and the approximate solution is known through (4.2-2).

The procedure just described is known as the *method of moments*. The principle of the method remains the same always. It is the detail that changes with the type of problem being considered, detail that is by no means trivial.

4.2.2 Essentials of the Finite-Difference Time-Domain Method

A. The Updating Equations

The FDTD algorithm is used to solve the time-dependent Maxwell's curl equations using second-order central difference approximations to sample the continuous electromagnetic fields in space and time steps. The algorithm staggers the electric and magnetic fields in both time and space, using the one to compute the other as time progresses by applying a so-called updating equation, which is thus referred to as a leap-frog algorithm. In the case of non-conducting dielectric materials whose properties are frequency independent and whose permeability is assumed to be μ_0 we can use the constitutive relations to rewrite Maxwell's curl equations as

$$\begin{aligned} \nabla\times\bar{E} &= -\mu_0\frac{\partial\bar{H}}{\partial t} \\ \nabla\times\bar{H} &= \frac{\partial\left\{\varepsilon\,\bar{E}\right\}}{\partial t}+\bar{J}^{source} \end{aligned} \tag{4.2-14}$$

In a rectangular coordinate system equations (4.2-14) can be written as six scalar partial differential equations

$$\begin{aligned} \frac{\partial H_x}{\partial t} &= \frac{1}{\mu_0}\left(\frac{\partial E_y}{\partial z}-\frac{\partial E_z}{\partial y}\right) \\ \frac{\partial H_y}{\partial t} &= \frac{1}{\mu_0}\left(\frac{\partial E_z}{\partial x}-\frac{\partial E_x}{\partial z}\right) \\ \frac{\partial H_z}{\partial t} &= \frac{1}{\mu_0}\left(\frac{\partial E_x}{\partial y}-\frac{\partial E_y}{\partial x}\right) \end{aligned} \tag{4.2-15}$$

$$
\begin{aligned}
\frac{\partial(\varepsilon E_x)}{\partial t} &= \frac{\partial H_z}{\partial y} - \frac{\partial H_y}{\partial z} + J_x^{source} \\
\frac{\partial(\varepsilon E_y)}{\partial t} &= \frac{\partial H_x}{\partial y} - \frac{\partial H_z}{\partial x} + J_y^{source} \\
\frac{\partial(\varepsilon E_z)}{\partial t} &= \frac{\partial H_y}{\partial x} - \frac{\partial H_x}{\partial y} + J_z^{source}
\end{aligned}
\qquad (4.2\text{-}16)
$$

In order to discretize the problem, the region in which the field exists is divided into electrically small rectangular cells (now called “Yee cells”). Figure 4.2-1 shows the spatial positions of the electric and magnetic field components within each Yee cell of the FDTD lattice. The three electric field components are computed at the midpoints of the edges of the cell, while the three magnetic field components are computed at the midpoints of the faces of the same cell.

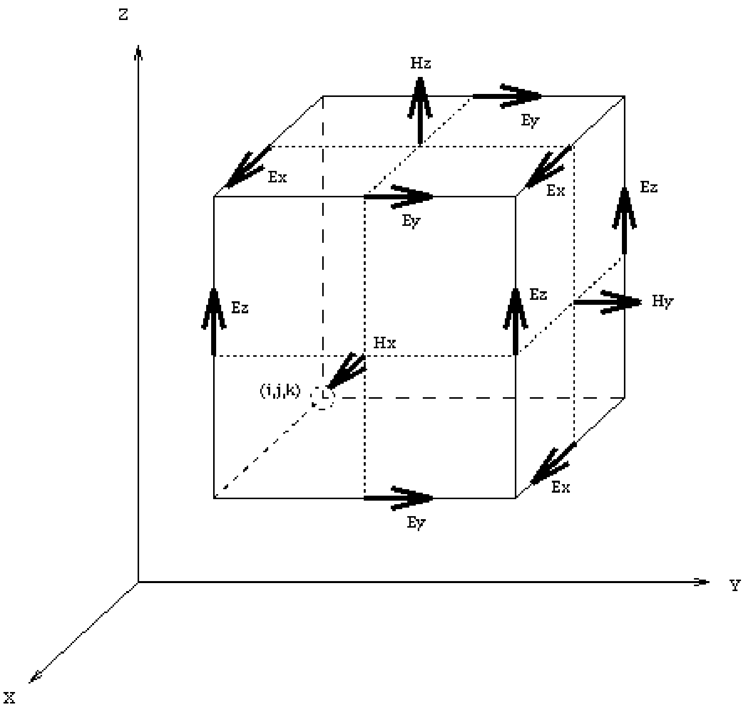

Figure 4.2-1 : Standard Yee Cell (After [5])

The FDTD algorithm approximates the derivatives in the six differential equations using finite differences, and obtains the updating equations for the six field components as

$$H_x^{n+\frac{1}{2}}(i,j,k) = H_x^{n-\frac{1}{2}}(i,j,k) - \frac{\Delta t}{\mu_o}\left[\frac{E_z^n(i,j,k) - E_z^n(i,j-1,k)}{\Delta y} - \frac{E_y^n(i,j,k) - E_y^n(i,j,k-1)}{\Delta z}\right]$$

$$H_y^{n+\frac{1}{2}}(i,j,k) = H_y^{n-\frac{1}{2}}(i,j,k) - \frac{\Delta t}{\mu_o}\left[\frac{E_x^n(i,j,k) - E_x^n(i,j-1,k-1)}{\Delta z} - \frac{E_z^n(i,j,k) - E_z^n(i-1,j,k)}{\Delta x}\right]$$

$$H_z^{n+\frac{1}{2}}(i,j,k) = H_z^{n-\frac{1}{2}}(i,j,k) - \frac{\Delta t}{\mu_o}\left[\frac{E_y^n(i,j,k) - E_y^n(i-1,j,k)}{\Delta x} - \frac{E_x^n(i,j,k) - E_x^n(i,j-1,k)}{\Delta y}\right]$$

$$E_x^{n+1}(i,j,k) = \frac{\varepsilon^n(i,j,k)}{\varepsilon^{n+1}(i,j,k)}E_x^n(i,j,k)$$

(4.1-17)

$$+\frac{\Delta t}{\varepsilon^{n+1}(i,j,k)}\left[\frac{H_z^{n+\frac{1}{2}}(i,j+1,k) - H_z^{n+\frac{1}{2}}(i,j,k)}{\Delta y} - \frac{H_y^{n+\frac{1}{2}}(i,j,k+1) - H_y^{n+\frac{1}{2}}(i,j,k)}{\Delta z}\right]$$

$$E_y^{n+1}(i,j,k) = \frac{\varepsilon^n(i,j,k)}{\varepsilon^{n+1}(i,j,k)}E_x^n(i,j,k)$$

$$+\frac{\Delta t}{\varepsilon^{n+1}(i,j,k)}\left[\frac{H_x^{n+\frac{1}{2}}(i,j,k+1) - H_z^{n+\frac{1}{2}}(i,j,k)}{\Delta z} - \frac{H_y^{n+\frac{1}{2}}(i+1,j,k) - H_y^{n+\frac{1}{2}}(i,j,k)}{\Delta x}\right]$$

$$E_z^{n+1}(i,j,k) = \frac{\varepsilon^n(i,j,k)}{\varepsilon^{n+1}(i,j,k)}E_z^n(i,j,k)$$

$$+\frac{\Delta t}{\varepsilon^{n+1}(i,j,k)}\left[\frac{H_y^{n+\frac{1}{2}}(i+1,j,k) - H_y^{n+\frac{1}{2}}(i,j,k)}{\Delta x} - \frac{H_x^{n+\frac{1}{2}}(i,j+1,k) - H_x^{n+\frac{1}{2}}(i,j,k)}{\Delta y}\right]$$

The (i,j,k) denote spatial points in the cell, while the superscripts in terms of n denote points in time.

B. Stability Issues

The electric and magnetic field components are computed at different times. The time difference is $\Delta t/2$, where Δt is the time step. The quantities $\Delta x, \Delta y$ and Δz are the cell dimensions along the x,y and z axes. If values of Δx, Δy or Δz are too large, the algorithm will not reproduce the wave movement with sufficient accuracy, and the simulation will fail. The choice of Δx, Δy or Δz is related to the value chosen for Δt. Thus the Δt value chosen for the model cannot be too large either. In order to ensure numerical stability the Δx, Δy and Δz, and the Δt, must be chosen so that the Courant stability criterion [5,6]

$$\Delta t \le \frac{1/c}{\sqrt{\left(\frac{1}{\Delta x}\right)^2 + \left(\frac{1}{\Delta y}\right)^2 + \left(\frac{1}{\Delta z}\right)^2}} \tag{4.2-18}$$

is satisfied.

C. The FDTD Implementation of Boundary Conditions

Boundary Conditions at Perfectly Conducting Surfaces

At points on a perfect electrically conducting surface the tangential component of $\bar{E}$ is zero, and the FDTD updating equation changes for such points, consisting of the setting of certain components to zero. For example, if the top surface of the Yee cell in Figure 4.2-1 is tangential to a perfect conductor then the FDTD updating equation there becomes

$$E_y(i,j,k-1) = E_y(i,j,k) = E_z(i,j-1,k) = E_z(i,j,k) = H_x(i,j,k) = 0 \tag{4.2-19}$$

Boundary Conditions at Points on the Interface Between Materials of Different Permittivities

At points that lie on the interface between different dielectric materials (of permittivities ε_1 and ε_2 say) the permittivity is actually not uniquely defined, and a problem arises as to which of the two permittivities should be used in the updating equations at such points. Usually [5] the average value of the two permittivities is used, namely $(\varepsilon_1 + \varepsilon_2)/2$, and is sometimes loosely referred to as “media averaging”.

Absorbing Boundary Conditions / Perfectly Matched Layers

Absorbing boundary conditions (ABCs) are used to truncate the solution region over which the

FDTD is applied in such a way that the FDTD method is “not aware” that this truncation has been done [5]. The FDTD implements these ABCs by providing special updating equations for points lying on the truncation boundary on which the ABC is enforced. An alternative is to use perfectly matched layers (PMLs) [5] to truncate the solution region[8]. At any rate, one encloses the complete specified geometry in a computational "box".

D. Source Types, and the Time-Dependence of Sources

A source is called *hard* if the total field at a source point is forced to have specified impressed values, irrespective of what is going on around it. A hard source is usually set up by simply assigning a desired time function to the total electric field at specific points in the FDTD spatial grid. It is independent of the fields at neighbouring points. A *soft* source is one that does not impress the value of the total electric field at any point. It can be implemented in many ways.

Irrespective of whether a hard or soft source is used the specific time-variation of the chosen source must be selected. In many cases where the FDTD method is used one desires to exploit one of its definite advantages over frequency-domain methods – namely the ability to so specify the time-variation of the source that a single simulation provides the system response over a band of frequencies rather than a single frequency. Thus baseband Gaussian pulse or sinusoidally modulated Gaussian pulse waveforms are often used [6]. Alternatively, a sinusoidal excitation can be used when just a single frequency is of interest.

---

[8] In simulations done using the code *EMPIRE* we will use PMLs.

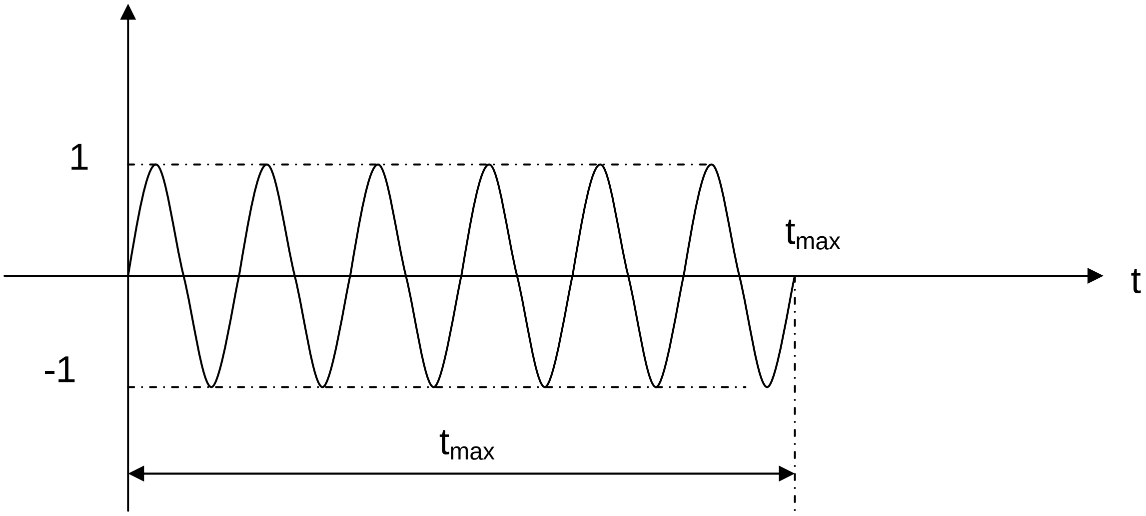

Figure 4.2-2 : Causal "Single-Frequency" FDTD Source

A closer examination of the spectrum of a "single-frequency" source as used in the FDTD method is useful [7]. In FDTD simulations only causal sources should be used. This means that the source signal, be it an electric current density acting as a source (and exciting a resultant incident field) or a directly specified field, the source will be zero for t < 0. Thus a "single-frequency" source (of frequency f_s, so that $\omega_s = 2\pi f_s$) will be as sketched in Figure 4.2-2. It turns on at t = 0 and lasts for a duration t_{max}, after which it is once more zero. If we represent this source signal by

$$f(t) = \begin{cases} \sin \omega_s t & 0 \le t \le t_{\max} \\ 0 & t < 0 \end{cases} \qquad (4.2\text{-}20)$$

then we can view this as the multiplication of a rectangular pulse existing between t = 0 and $t = t_{max}$ with the sinusoid. In other words,

$$f(t) = f_1(t) \cdot f_2(t)$$

$$f_1(t) = \begin{cases} 1 & 0 \le t \le t_{\max} \\ 0 & t < 0 \end{cases} \qquad (4.2\text{-}21)$$

$$f_2(t) = \sin \omega_s t \qquad -\infty < t < +\infty \qquad (4.2\text{-}22)$$

The spectrum (in other words, Fourier transform) of the source signal is then the convolution of the transforms of the above shifted pulse and sinusoid. The individual Fourier transforms are

$$F_1(\omega) = 2e^{-j\omega t_{\max}/2} \cdot \sin c(\frac{\omega t_{\max}}{2\pi}) \qquad (4.2\text{-}23)$$

and

$$F_2(\omega) = (-j\omega) \cdot \left[\pi\delta(\omega - \omega_0) + \pi\delta(\omega + \omega_0)\right] \qquad (4.2\text{-}24)$$

The convolution of the above separate transforms leads to

$$F(\omega) = e^{-j(\omega-\omega_s)t_{\max}/2} \cdot \{\sin c[\frac{(\omega - \omega_s)t_{\max}}{2\pi}] + \sin c[\frac{(\omega + \omega_s)t_{\max}}{2\pi}]\} \qquad (4.2\text{-}25)$$

Its amplitude is

$$\left|F(\omega)\right| = \left|\sin c[\frac{(\omega - \omega_s)t_{\max}}{2\pi}] + \sin c[\frac{(\omega + \omega_s)t_{\max}}{2\pi}]\right| \qquad (4.2\text{-}26)$$

and is plotted in Figure 4.2-3 for two different values of $t_{\max}$ and f_s = 10 GHz. We observe that while a true (infinite duration) sinusoid of frequency f_s would have a spectrum consisting of a single spectral line at f = f_s, this is not the case for the finite duration signal. There is a maximum at f = f_s, but additional frequency components are present. The longer the duration of the source signal the more it "looks" like a single-frequency sinusoid with an increasingly sharp "spectral line" at f = f_s.

The modulated Gaussian pulse type excitation mentioned at the beginning of this section are of the form[9]

$$f(t) = e^{[(t-t_o)/\tau]^2} \sin\omega_s(t - t_o) \qquad (4.2\text{-}27)$$

The Fourier transform operation shows that such a waveform contains a spectrum of frequencies centred around the frequency ω_s, the width of the spectrum being determined by the value of the

---

[9] In simulations done using the code *EMPIRE* this is the source type that will be used in this thesis.

parameter τ . The FDTD simulation output for such a source can provide the response for several frequencies.

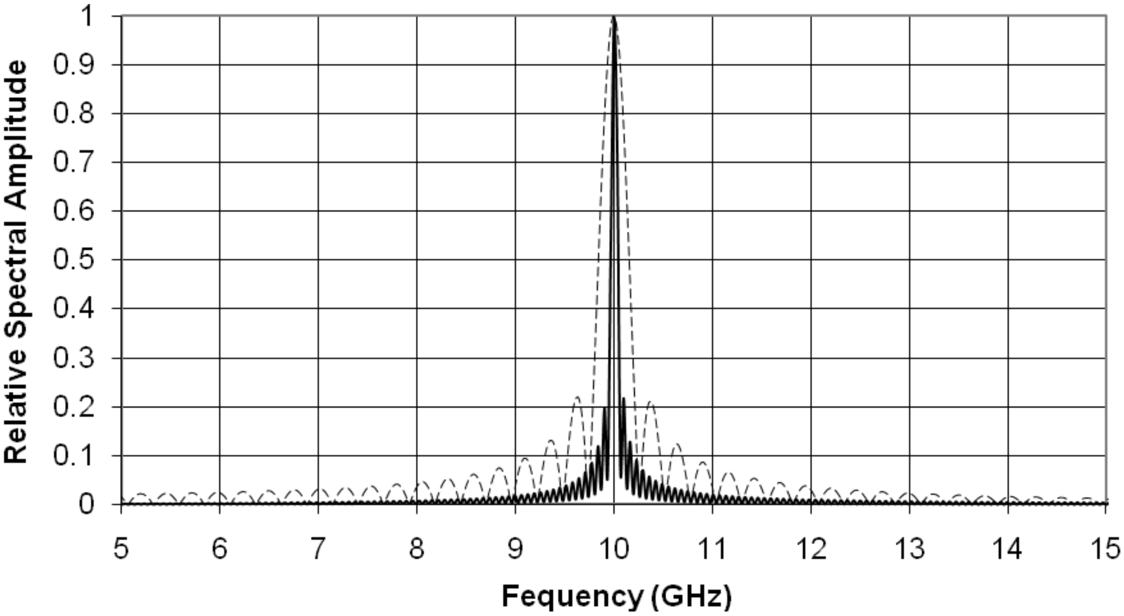

Figure 4.2-3 : Fourier Transform of the Finite Duration “Single-Frequency” Source (f_s = 10 GHz) for t_{max} = 3.856ns (- - - -) and t_{max} = 15.424 ns (——).

4.3 VALIDATION OF THE MOMENT METHOD MODELLING FOR THE CLASS OF PROBLEM OF INTEREST

4.3.1 Reasons for the Use of the Moment Method Modelling

There are at least two reasons that the method of moments was used in this work. Firstly, a moment-method based code FEKO [1], which can deal with both volumetric and planar geometries, is widely used in antenna engineering. Secondly, as will be seen in Section 5.3, we wished to model a planar holographic antenna with a sectoral horn feed, so that we could carefully control the feed radiator beamwidth and observe this effect on the holographic antenna directivity. The analysis of such a geometry is not well-suited to an FDTD analysis (where the complete solution region has to be discretised).

4.3.2 General Remarks on Modelling Using FEKO Version 5.5

The remarks in some of these sub-sections might be considered somewhat less than archival. However, since they refer to aspects that are not initially obvious it was thought worth mentioning them. The code FEKO has three main elements. CADFEKO is used for drawing (and viewing) the model and to specify the output requirements (eg. far-zone fields). POSTFEKO is used to view the model geometry and to view the output data once a simulation is complete. EDITFEKO allows one to write scripts for generating complicated geometries whose point-by-point manual specification would be prohibitively laborious, as will be discussed in Section 4.3.5. Geometries generated in this way can unfortunately not be viewed using CADFEKO. One has to actually first run the simulation and view the model geometry as part of the output in POSTFEKO. Furthermore, FEKO does not automatically store all output data from a particular run. The user has to be specific about what needs to be stored for later use. This can be laborious, and can result in many time-consuming re-runs if one is not aware of it!

4.3.3 Modelling of a Sectoral Horn Using FEKO

We refer to Figure 4.3-1. In FEKO a waveguide excitation can be used to excite a horn through the waveguide input section of the horn. In order to specify such an excitation one defines a face at the desired location in the waveguide section. The red box in Figure 4.3-1 shows the outline of the port. Having done this, FEKO has a special "waveguide excitation" feature where one is able define the relative magnitudes, phases (and rotations in the case of a non-rectangular waveguide shape) of the required modes. In this case, we wish only to excite the fundamental TE_{10} mode of a rectangular waveguide.

FEKO uses triangular surface meshing on conductors over which to define the expansion functions referred to in Section 4.2.1. It is recommended that each triangular element have an area smaller than $\lambda^2/70$, and for triangles that are approximately equilateral this means the length of any side should be shorter than about $\lambda/6$. The precise form of the expansion functions is proprietary information. However the fact that meshing is controlled by the lengths of the common line between two adjacent triangles (the "edges") hints that so-called RWG expansion functions are being used, possibly of higher than zero order. A meshed version of the horn of Figure 4.2-1 is shown in Figure 4.2-2. Simulation produces the current density shown in Figure 4.3-3, which can be used to establish if the modelling is being done correctly[10].

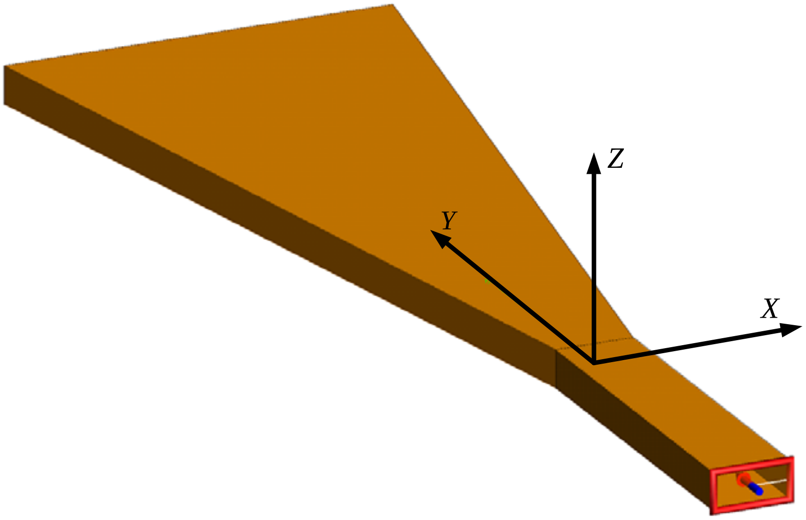

Figure 4.3-1 : Sectoral horn radiator geometry

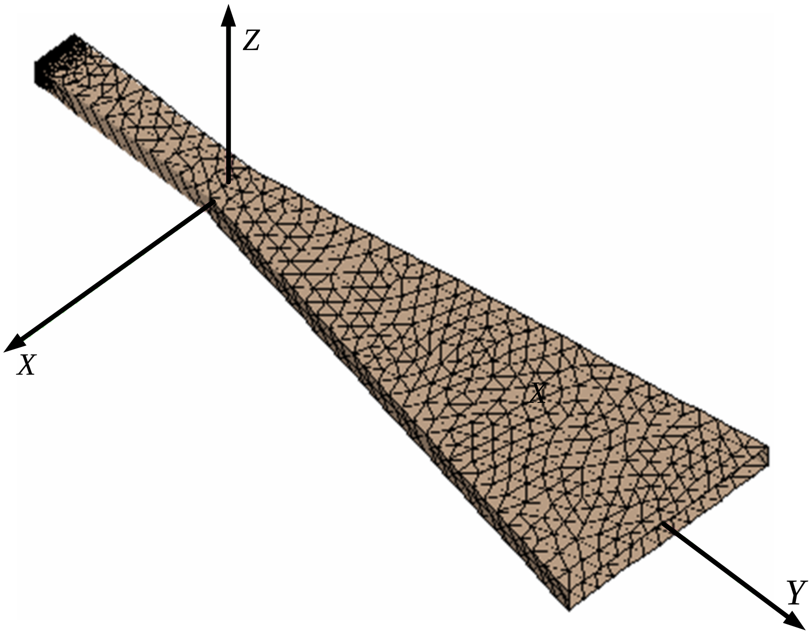

Figure 4.3-2 : Conducting surface of the sectoral horn in Figure 4.2-1 after meshing

---

[10] Radiation patterns will be shown in Section 5.3.

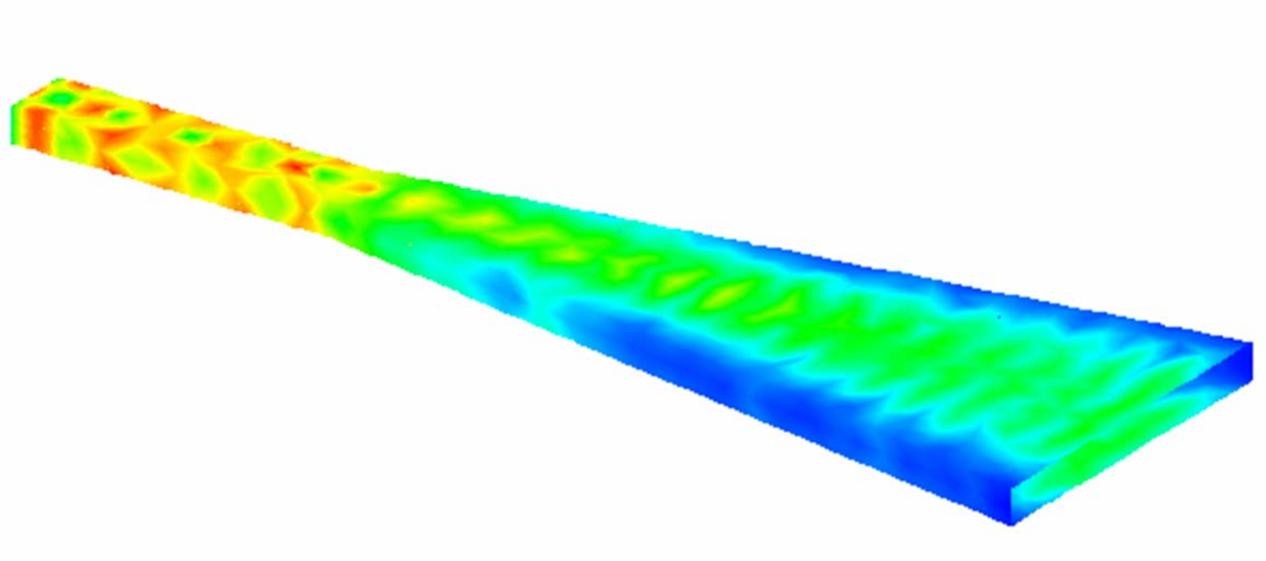

Figure 4.3-3 : Three-dimensional colour representation of the current density on the conducting walls of the sectoral horn in Figure 4.3-1 after FEKO simulation.

4.3.4 Modelling of the Hologram Portions of the Planar Holographic Antenna

If the dipole hologram is of interest the dipoles can be modelled as thin conducting wires or as zero-thickness conducting strips. Only the latter type is feasible of the dielectric substrate is to be included in the model.

A. Conducting Wire Dipoles

The segment lengths (that is, regions over which an expansion function is defined) on each dipole must less than $\lambda/6$, and for the thin-wire assumption to be valid the radius has to one-twelfth of a segment length. In order to define a dipole the (x, y, z) coordinates of the two endpoints of each individual dipole has to be specified. One advantage of using wire dipoles is that numerical values of the currents can be extracted from FEKO, but colour depictions of the current magnitudes over the hologram is difficult to interpret.

B. Conducting Strip Dipoles

If the hologram dipoles are modelled as zero-thickness conducting strips they are treated as surfaces by FEKO. They are defined by specifying the (x, y, z) coordinates of the four corners of each individual strip. One disadvantage of using strip dipoles is that actual numerical values of the currents cannot be extracted from FEKO, but colour depictions of the current magnitudes over the hologram are insightful, and allows one to immediately grasp the strip current distributions.

C. Algorithm for Dipole Hologram Generation

It would be prohibitively laborious to have to specify each hologram dipole manually, especially remembering that the whole idea of modelling the holographic antenna is to determine how its performance is affected by changes in dimensions, amongst other things. An algorithm was therefore developed and scripted to do this set-up automatically. It can be used for both wire dipole elements and conducting strip elements. The algorithm will next be described, with reference to Figure 4.3-4, and for the 14-ring hologram. Taking advantage of the symmetry command in FEKO, only half the dipoles[11] will need to be generated by the script. Therefore only elements in the region $z \leq 0$ (the left hand side) are needed. Once we can locate (x_n, z_n) for a given *n* on a given row *m*, the coordinates of the ends of each wire dipole, or the corners of each strip dipole, are easily determined. The elements lying on the centerline (the x-axis) are generated first. Since only the elements located in the region z < 0 elements need to be specified, the algorithm must only draw half dipoles for the centre elements.

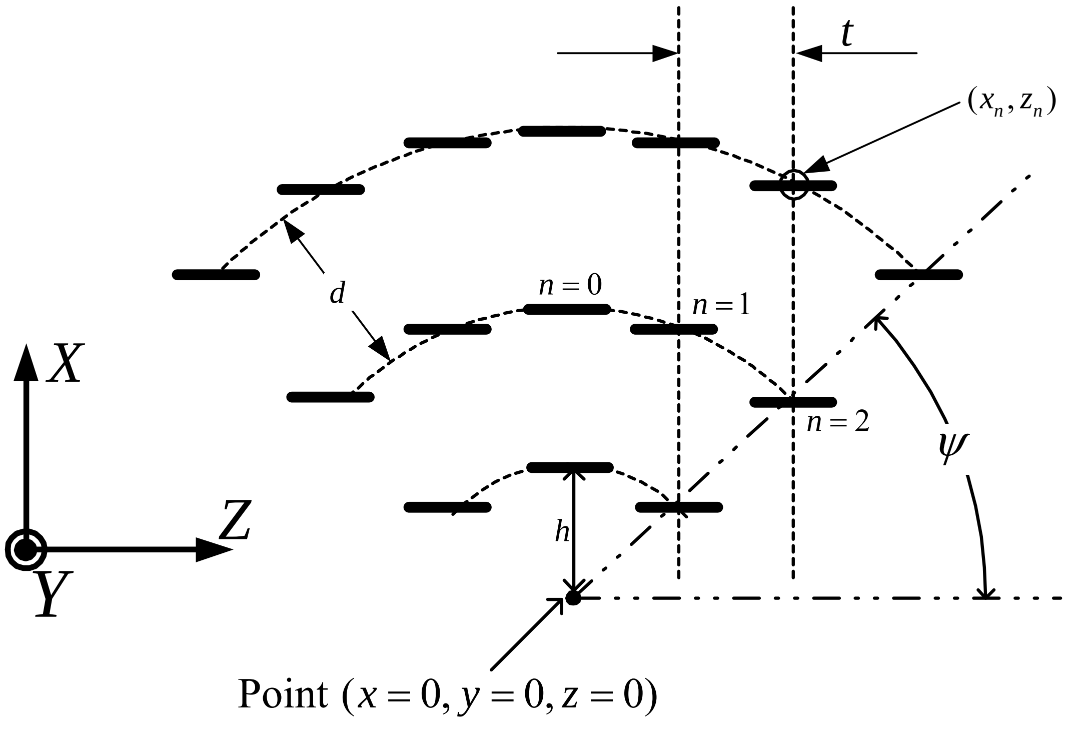

---

[11] The dipole elements of the hologram are $\lambda/2$ in length, as indicated in Section 2.4.

Figure 4.3-4 : Representative dipole elements in the hologram. (Not all the rings of elements are shown. Note that the ring radii ρ_m are known for a given design).

The next step is to determine how many dipoles need to be generated for each arc. This will be found algorithmically using a stopping variable ξ_m. For example, in the second row, only three elements are required and the stopping variable is therefore $\xi_m = 2$. Angle ψ_m on the diagram is 45° for the first 10 rows, and has a different value for subsequent rows to give the diamond boundary of the hologram. The values of this angle for the 14-ring hologram are summarised in Table 4.3-1.

Table 4.3-1 : Values of ψ_m for each row in the 14-ring hologram

Row Number (m)	**Radius ρ_m**	**Angle ψ_m**
1 -10	1 mm -10 mm	45°
11	11 mm	69.62°
12	12 mm	78.55°
13	13 mm	84.71°
14	14 mm	89.4°

Using these angles, and the

$$\xi_m = \frac{\rho_m \cos\psi_m}{\lambda / 2} \tag{4.3-1}$$

gives the value of the stopping variable for each row. The centre coordinates (x_n, z_n) of the *n*-th dipole on the *m*-th row are calculated for each element until the subscript *n* is equal to value of the stopping variable ξ_m. The right hand side is then mirrored in the x-axis, and the specification of all dipoles, in the hologram is complete.

In the above explanation we assumed a single-layer hologram with the elements lying in the $y = 0$ plane. With a two layer system this can easily be modified by running the algorithm twice, and adding $y = -g/2$ for the dipoles on the bottom layer and $y = g/2$ for the dipoles on the top layer.

D. Incorporation of Dielectric Substrate Using FEKO

FEKO has a number of set geometrical shapes one can use to describe a geometry that contains volumetric dielectric material. In Section 4.3.7 we will model a dielectric substrate. In order to do this one can select a so-called cuboid shape (actually a box whose sides are not all of equal length). The quantitative details can be established by specifying the (x, y, z) coordinates of each of the eight vertices of the cuboid. Alternatively, one can specify the coordinates of the corners of one face of the cuboid and then give the height. In order to place a zero-thickness conductor on a portion of the dielectric object the (x, y, z) coordinates of the conductor are declared (these will coincide with points on the dielectric object, albeit not necessarily its vertices), and a 'union' operation is declared so that the code is "aware" of the fact that the conductor touches the surface of the dielectric object. Specification of the properties of the dielectric object completes the model.

4.3.5 Modelling of Yagi Feeds for the Planar Holographic Antenna

In the modeling of the holographic antenna using a Yagi feed radiator it is essential that we be able to model the groundplane needed for the microstrip feedline as a finite size groundplane. Use of an infinite groundplane would mean the hologram would be above a groundplane. This is not the antenna we have in mind. The FEKO code unfortunately does not have a specific microstrip port model that can be used with a finite sized conducting groundplane. One therefore has to use the objects available to piece together a model of the Yagi microstrip feedline. This can be done by modelling the microstrip track and the groundplane as separate planar conducting objects. The only possible excitation available in such instances is the use of a short conducting wire connected between the track and the groundplane, with a port defined at the centre of this short wire, as we try to illustrate in Figure 4.3-5.

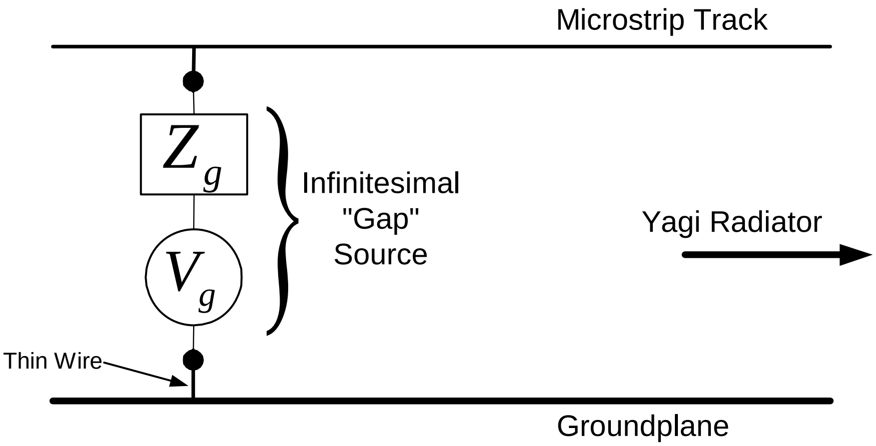

Figure 4.3-5 : Side view of microstrip track and groundplane with connecting wire that has a

lumped Thevenin source (shown here enlarged for clarity).

The generator impedance/load Z_g can be complex, and is by default set to zero in FEKO. When one thinks in circuit terms this appears to be an acceptable thing to do. We at first used this arrangement with the 6-element Yagi mentioned in Section 2.4. However, it was discovered that the computed reflection coefficient (say $|S_{11}|$) of the Yagi was dependent on the length of microstrip line connected to it, which was clearly in error. Further observation of the current distribution on the microstrip balun revealed that the generator was acting as a short to signals reflected at the balun/Yagi interface, creating a resonator effect between the generator and the Yagi. We solved this problem by separately computing the characteristic impedance Z_o of the microstrip line[12], and then setting $Z_g = Z_o$. Signals reflected at the balun/Yagi interface which travel back towards the generator along the microstrip line in question are then absorbed by (are matched to) the Z_g. Actual maximum and minimum current standing wave values were used to calculate the VSWR and hence $|S_{11}|$. These correct predictions of $|S_{11}|$ are then also forthcoming from POSTFEKO and independent of the microstrip line length, as required[13].

Further convergence tests revealed that accurate modelling can only be done with a very dense mesh used on the microstrip track and on the portion of the groundplane immediately below the track. It would be computationally inefficient to use such a dense mesh over the entire groundplane. Thus the groundplane was declared to be three separate conducting planes that are 'unioned' to form a single object, so that a shaded mesh (that is, non-uniform mesh density) could be used as shown in Figure 4.3-6.

The computed directivity patterns of the complete 6-element Yagi model (by complete we mean the microstrip balun plus the radiating elements) are shown in Figures 4.3-7 and 4.3-8. The asymmetries in the patterns are expected due to the fact that the driven element arms are not coplanar and the balun is not symmetrical, and so the structure itself is asymmetrical.

---

[12] This was done using the software TX-Line of Applied Wave Research (www.awrcorp.com). A line with $Z_o = 75\Omega$ was used.

[13] The complication is that this value of Z_g must subsequently be subtracted before using POSTFEKO to provide the correct values of $|S_{11}|$.

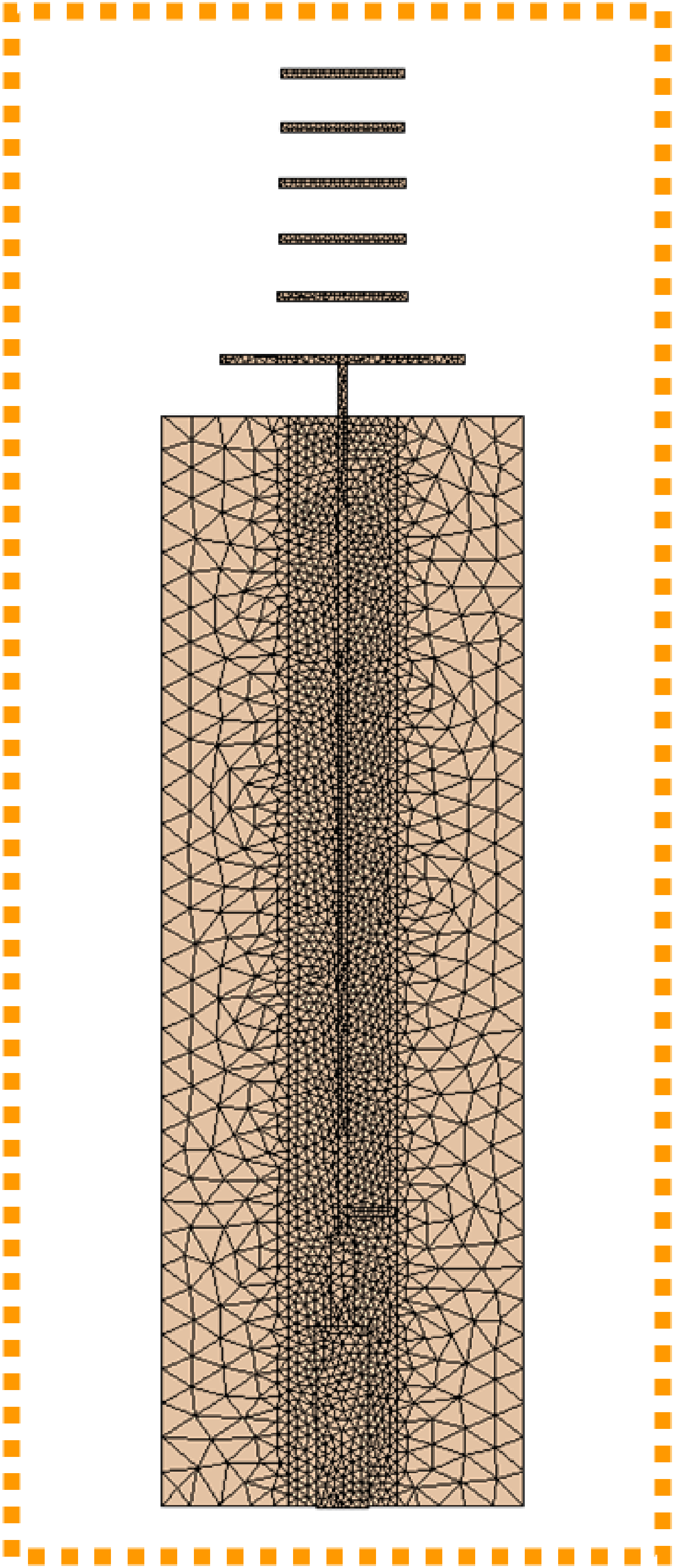

Figure 4.3-6 : Meshing of the microstrip track and groundplane (together forming a balun) used to feeding the 6-element Yagi

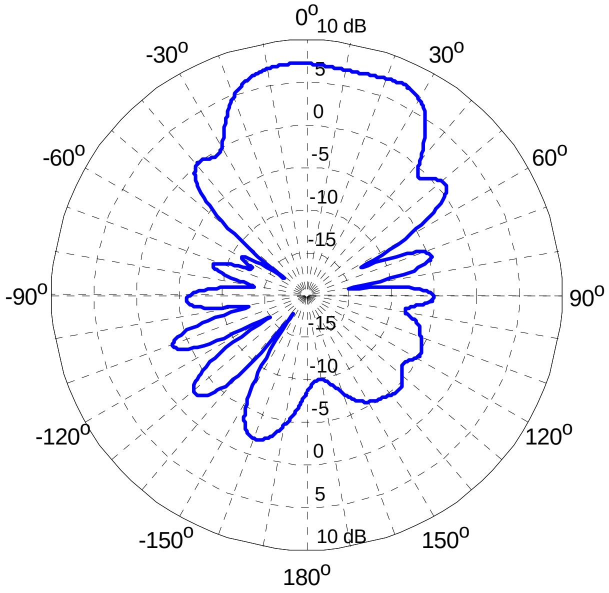

Figure 4.3-7 : Directivity pattern (dBi) of the 6-element Yagi in the E-plane.

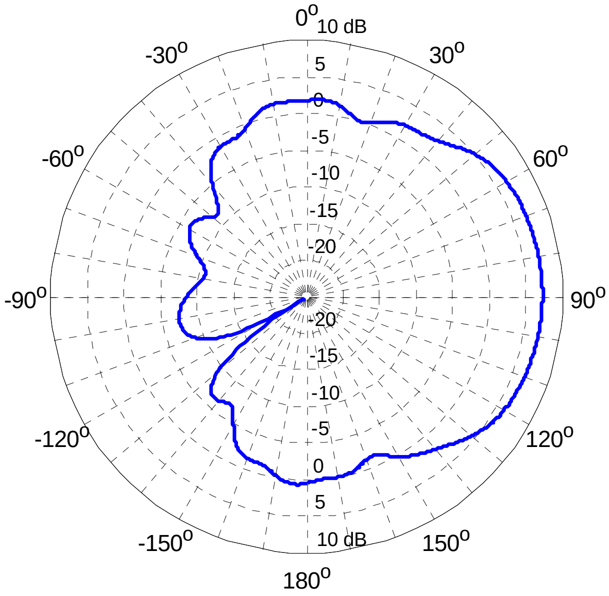

Figure 4.3-8 : Directivity pattern (dBi) of the 6-element Yagi in the H-plane.

4.3.6 Modelling of Yagi-Fed Planar Holographic Antenna – No Substrate

Hologram #2 of Table 2.5-1 was used with conducting strip dipoles. The algorithm described in Part C of Section 4.3.4 was used to generate the hologram geometry for simulation in FEKO. Manual experimentation revealed that removal of the first dipole improved the maximum broadside directivity slightly. The layout of the computational model, which includes that of Figure 4.3-6, is depicted in Figure 4.3-9. The predicted directivity patterns are shown in Figures 4.3-10 and 4.3-11. These are similar to what has been obtained experimentally by others for holographic antennas of this type. Observe the presence of the grating lobes (mentioned in Chapter 3) in the forward direction. The presence of the Yagi has caused this lobe to be "split", and has contributed to a substantial lowering of the grating lobe in the reverse direction due to its blockage effect.

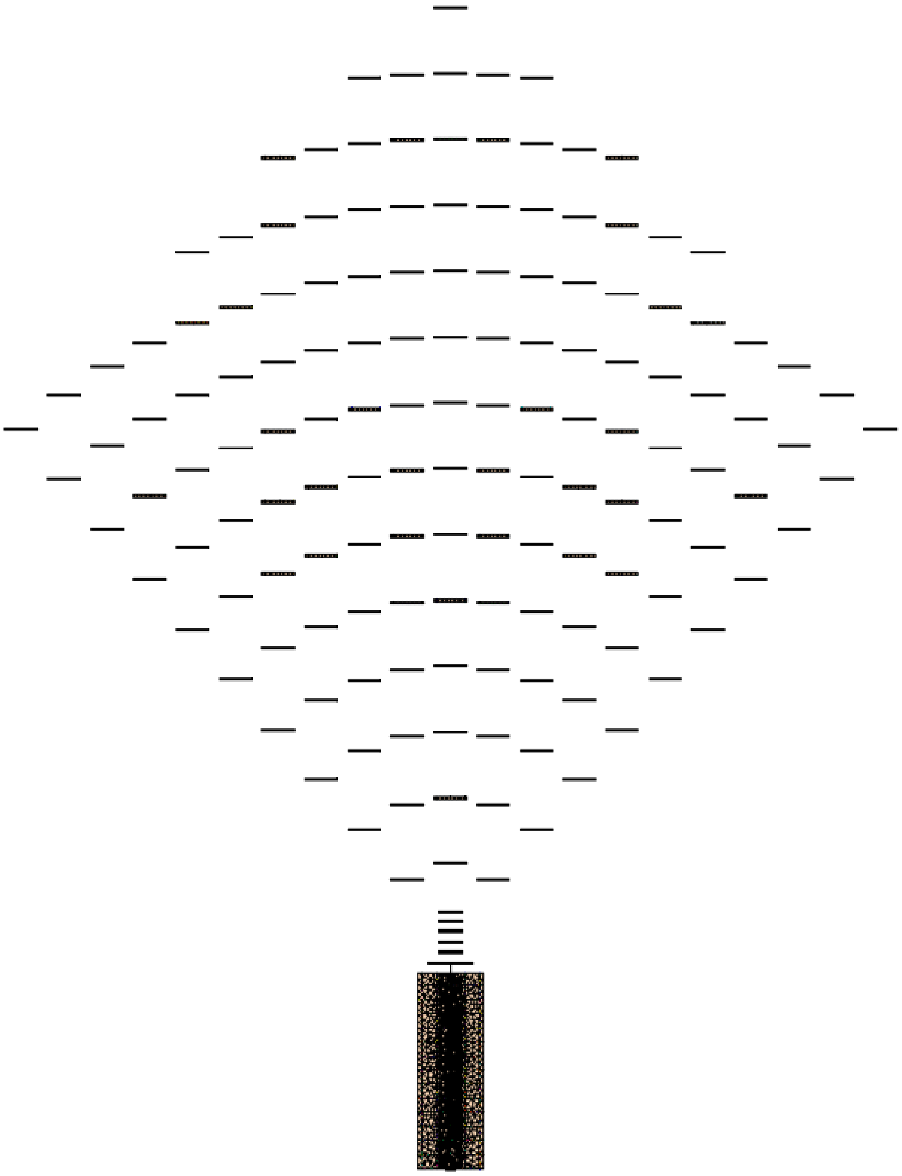

Figure 4.3-9 : Model of the complete single-layer holographic antenna (6-element Yagi radiator and strip dipoles).

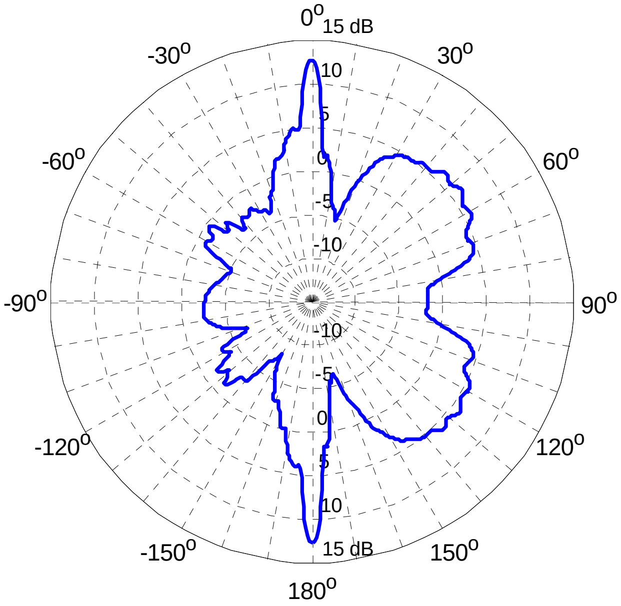

Figure 4.3-10 : Directivity pattern (dBi) of the complete single-layer holographic antenna (6-element Yagi radiator and strip dipoles) the H-plane at 30 GHz.

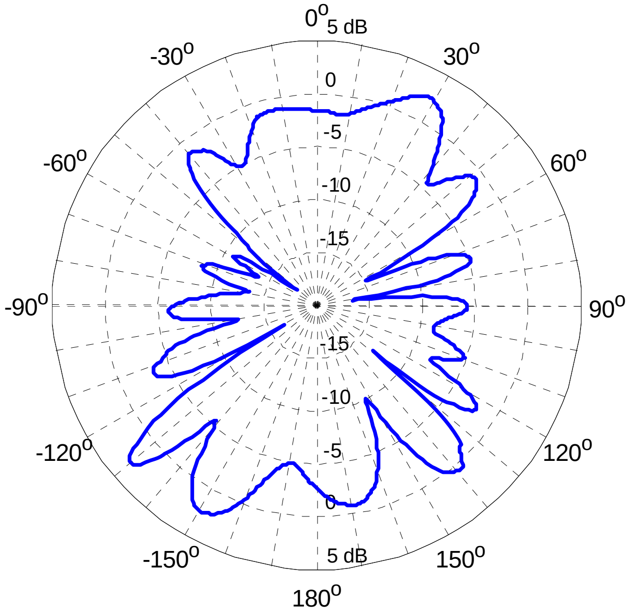

Figure 4.3-11 : Directivity pattern (dBi) of the complete single-layer holographic antenna (6-element Yagi radiator and strip dipoles) the E-plane at 30 GHz.

4.3.7 Modelling of Yagi-Fed Planar Holographic Antenna – With Substrate

In the previous section we considered the Yagi-fed hologram with a free-space substrate (eg. as if the complete antenna had been laid out on low permittivity foam). As a next step we included a substrate. It is important to realize that for the antenna configurations of interest here the substrate, like the groundplane, needs to be modelled with a finite size. The situation is different from what could be used when modelling an array of microstrip patches, for instance, where acceptable pattern results in the broadside directions (and even input impedances) can be obtained using the assumption of an infinite substrate and groundplane. In the latter case the Green's functions appropriate for layered media can be used, and the unknowns needed in the moment method procedure do not include groundplane conduction currents or polarisation currents (or their equivalent surface currents) in the substrate. In the present situation unknowns include the said currents on the groundplane and substrate. The substrate has to be considered as a volumetric dielectric object, as noted in Part D of Section 4.3-4. This severely increases the computational burden. The 3-element Yagi design of Section 2.4 was modelled in FEKO, with a substrate of thickness 0.508 mm (20 mils) and relative permittivity 3.38, as illustrated in Figure 4.3-12. The predicted radiation pattern in the E-plane is shown in Figure 4.3-13 as the number of expansion functions in the substrate is increased by substantial amounts. Each different curve is for a different number of expansion functions. The convergence is very slow, especially as far as absolute directivity values are concerned. It is for this reason that FEKO will not be used in Chapter 5 for those cases where we wish to specifically include substrate effects. The FDTD method used by the commercial code EMPIRE will be used in such cases instead. Indeed, this same 3-element Yagi radiator will be modelled using EMPIRE in Section 4.4 and the outcome compared to measurements.

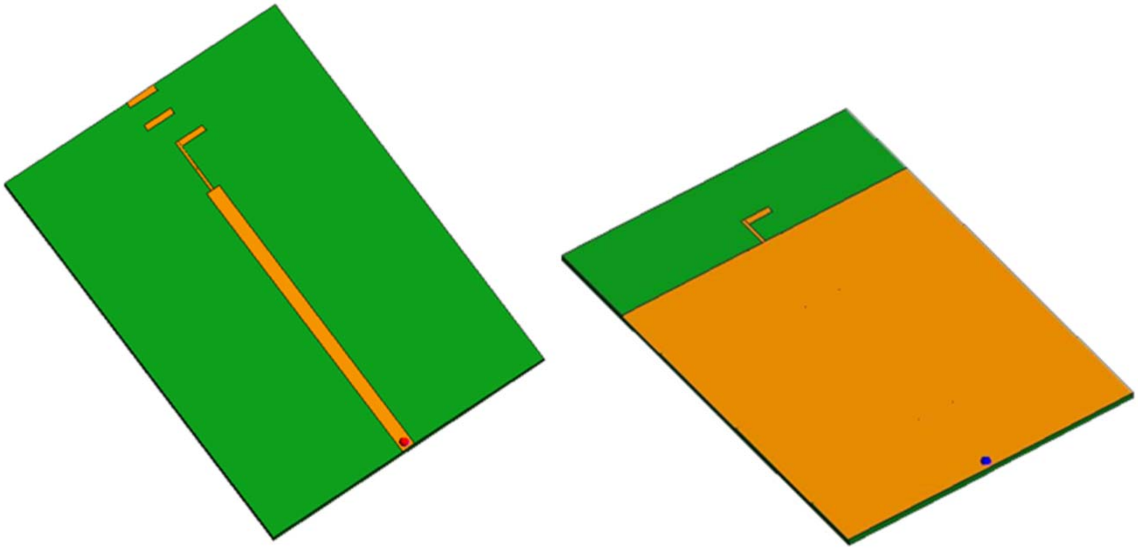

Figure 4.3-12 : Illustrative views of the FEKO model of a three-element Yagi on a substrate

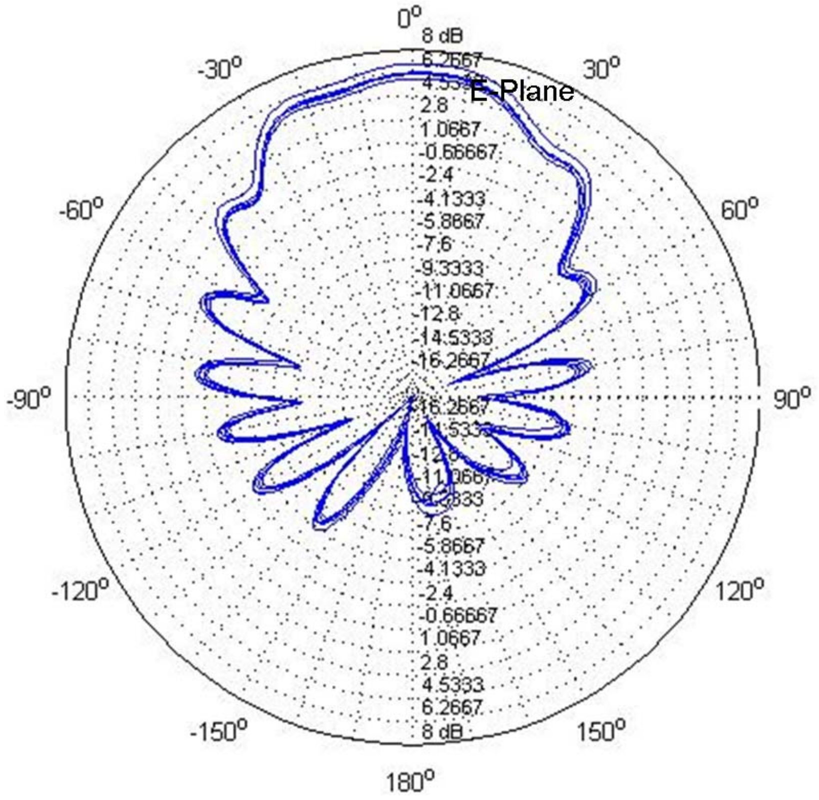

Figure 4.3-13 : Computed E-plane directivity patterns of the 3-element Yagi shown in Figure 4.3-12

4.4 VALIDATION OF THE FDTD MODELLING FOR THE CLASS OF PROBLEM OF INTEREST

4.4.1 Selection of Validation Problem

As commented previously the difficulty of modeling the complete holographic antenna is its electrically large size. As with the FEKO modelling, we will first consider a smaller problem, namely the feed radiator portion of the holographic antenna, in this instance the 3-element Yagi design. The predicted patterns will be compared to measurement on such a Yagi radiator (that was fabricated) and provide some validation of the modelling process for the class of problem of interest in this thesis. This problem is electrically significantly smaller than when the hologram is included, allowing for a shorter run time to perfect the modeling process (in EMPIRE) before proceeding to the complete holographic antenna.

4.4.2 Details of Some EMPIRE™ (Release 5.4) Modelling Procedures

Before a simulation can take place, some parameters need to be declared under the "Simulation Setup" menu. A frequency is required for simulation, but a range should be selected unless resources are severely limited. The meshing in EMPIRE uses a grid system, and the grid is defined by cell size based on highest frequency wavelength. The accuracy of the results will depend highly on the mesh density. Meshing is done automatically in EMPIRE, or can adjusted by the user. For the cases in this thesis the meshing was left to EMPIRE to do but the mesh resolution had to be defined.

EMPIRE allows a very coarse mesh, coarse mesh, medium mesh, fine mesh and very fine mesh options. Once one selects one of these the meshing is done automatically. We have only been able to use the "very coarse (8/3)" mesh option for the complete holographic antenna of interest in this thesis. The "(8/3)" is defined as (cells/wavelength, cells/object). The EMPIRE literature suggests use of mesh of medium resolution, "medium (15/4)". However, the final structure of interest in this thesis is so electrically large that the medium mesh was not possible using available resources. Fortunately the mesh used provides almost identical far-field pattern results compared to that when the medium mesh option[14] is used, and good agreement of the near-fields (except for some minor differences in detail, as will be noted in Section 5.5).

---

[14] The medium mesh option using one of the model input files used in this thesis was run on a more powerful computer at the Communications Research Centre Ottawa, but took considerable time to run. The "coarse (10/3)" mesh was the only one found to run in a reasonable amount of time (several hours) on the latter computer. The fine option was also tried there, but eventually terminated after several days.

EMPIRE works on a layering system. If we have a dielectric substrate and conducting shapes on both sides we have a three layer system. Each of the layers is defined and then these are placed together. We refer the reader to Figure 4.4-1. We will use a coordinate system in which the z-axis is normal to the layers. The top layer is metal ("Metal 200" is copper), and we specify this to be 20μm thick. The substrate is specified as having a thickness of 508 μm thick and relative permittivity of 3.38. Lastly the lower conducting layer (also "Metal 200") has a thickness of 20 μm too. Hence the arrangement shown in Figure 4.4-1, which we will use everywhere in this thesis that EMPIRE simulations are described.

EMPIRE essentially stores all key information that it has computed after a specific run. If one then needs additional output quantities at a later stage it is possible to obtain this without having to re-run the simulation. This makes it most convenient for the user.

EMPIRE is preferable to FEKO for the modelling of the Yagi-fed planar holographic antenna with a substrate because it has a microstrip port option. This removes the problems encountered with FEKO modelling of the Yagi that were described in Section 4.3.5.

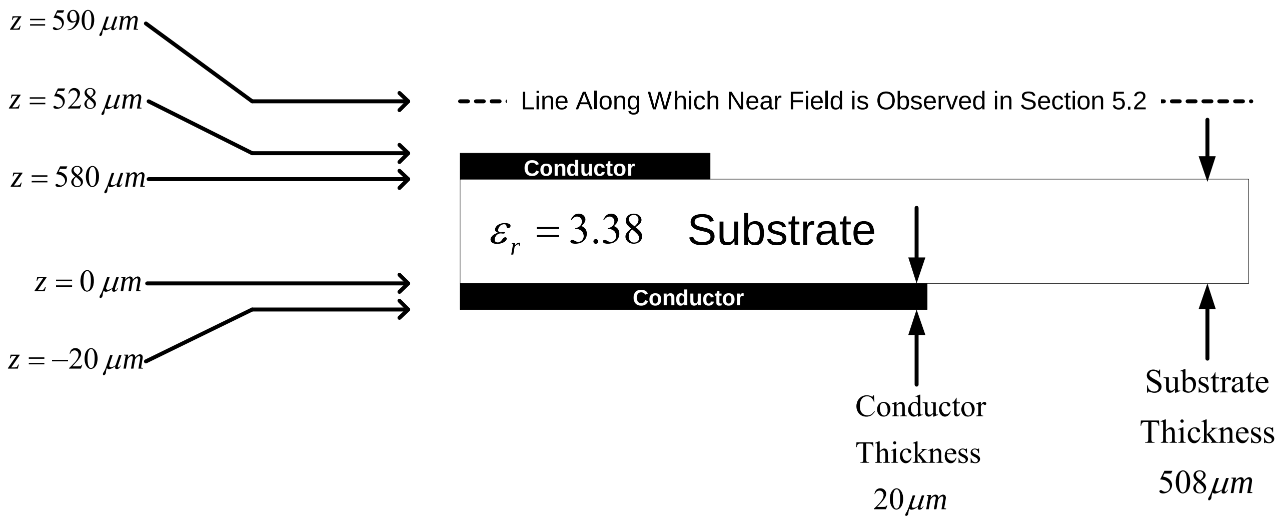

Figure 4.4-1 : Details of the substrate and conductor layering used.

4.4.3 Modelling Outcomes for the Validation Problem

The fabricated 3-element Yagi is shown in Figures 4.4-2 and 4.4-3, and in its measurement jig in Figure 4.4-4. Computed and measured directivity patterns in the two principal planes are compared in Figures 4.4-5 and 4.4-6. With coordinate axes orientated as we have them in the EMPIRE model, we obtain the E-plane pattern by setting $\theta = 90^\circ$ and sweeping angle ϕ, and $|E_{co}| = |E_\phi|$ whereas $|E_{cross}| = |E_\theta|$. The H-plane pattern by setting $\phi = 90^\circ$ and sweeping angle θ, and now $|E_{co}| = |E_\theta|$ and whereas $|E_{cross}| = |E_\phi|$.

Practicalities required that metal connector blocks be used, as shown in the photos. The nice thing about the electromagnetic simulation methods is that such objects can be included in the model. This was done for the EMPIRE model under discussion here. The measured directivity patterns in the two principal planes are compared to this enhanced model that includes the connector blocks in Figures 4.4-7 through 4.4-10, this time for both the co- and cross-polar cases. The connector boxes, in spite of their relative size, have surprisingly little effect on the patterns. Nevertheless, we do observe in Figure 4.4-8 that there is better agreement between the measured and computed cross-polar patterns when the connector blocks are included in the model. In this case the electric field is perpendicular to the mounting jig during measurement. The same cannot be said for the H-plane cross-polar patterns in Figure 4.4-10. This is attributed to the influence of the mounting jig, since for the H-plane measurement the jig is parallel to the electric field.

Finally, the computed and measured return loss are shown side by side in Figure 4.4-11. While the computed return loss is best at the design frequency of 30 GHz, the most favourable return loss occurs for the fabricated antenna at 26 GHz. Nevertheless, between 26 GHz and 33GHz, the return loss is still better than -10 dB.

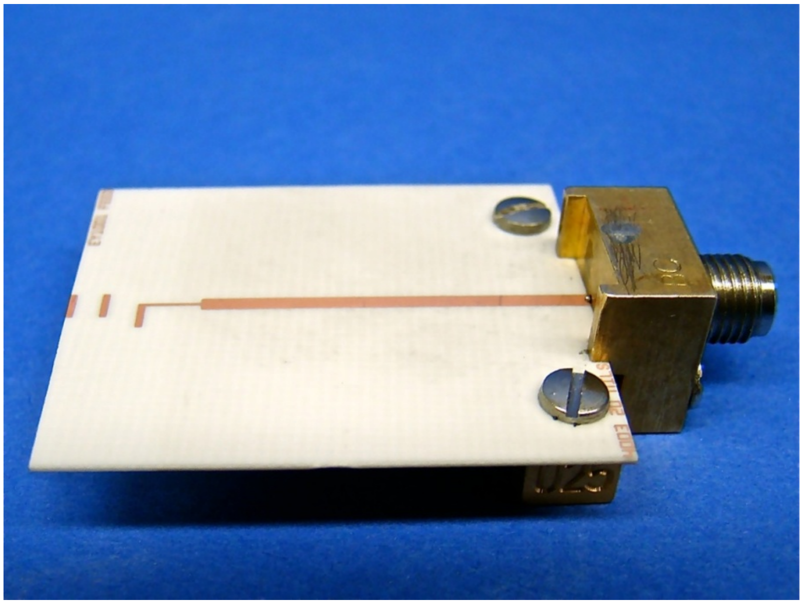

Figure 4.4-2 : Top view photograph of the fabricated 3-element Yagi antenna with connector boxes.

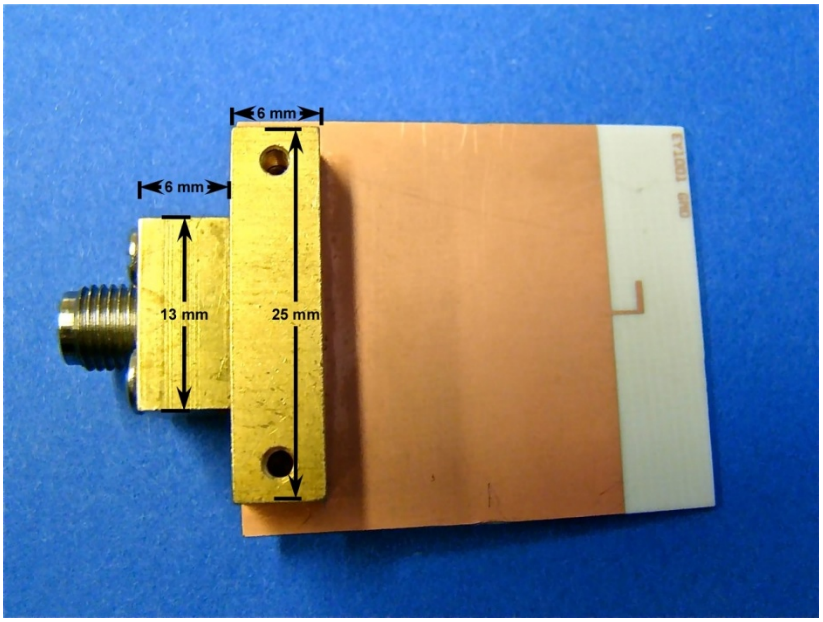

Figure 4.4-3 : Bottom view photograph of the fabricated 3-element Yagi antenna with connector boxes.

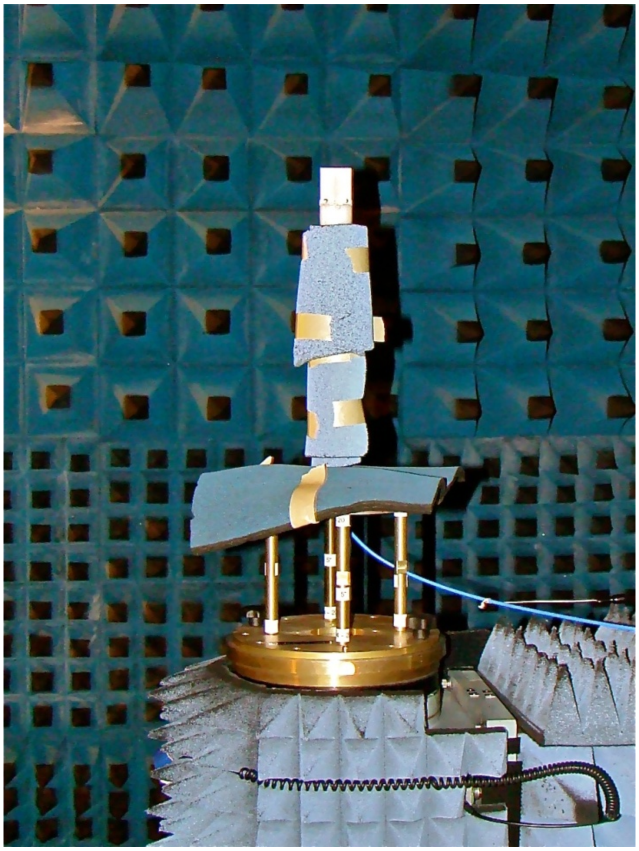

Figure 4.4-4 : 3-Element Yagi antenna and measurement mounting jig.

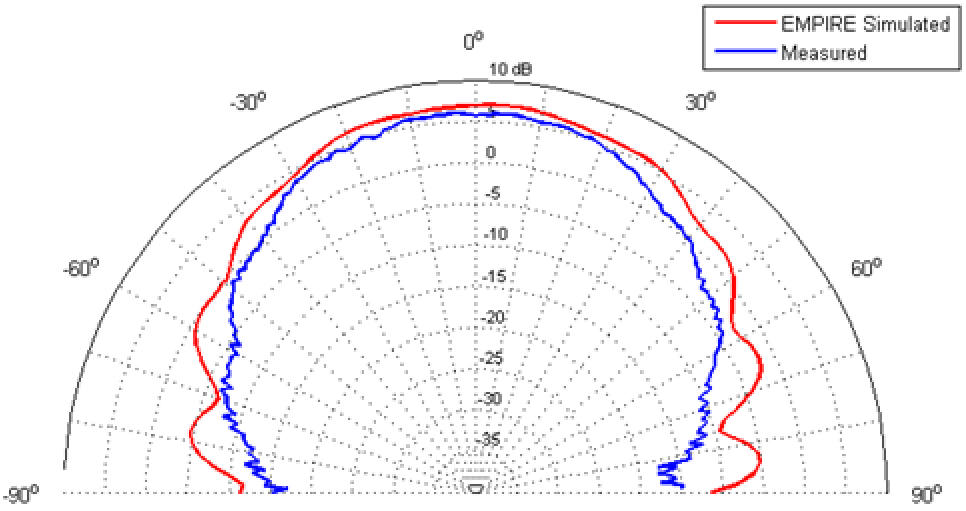

Figure 4.4-5 : Co-polarised computed and measured directivity patterns (dBi) of the 3-element Yagi in the E-plane

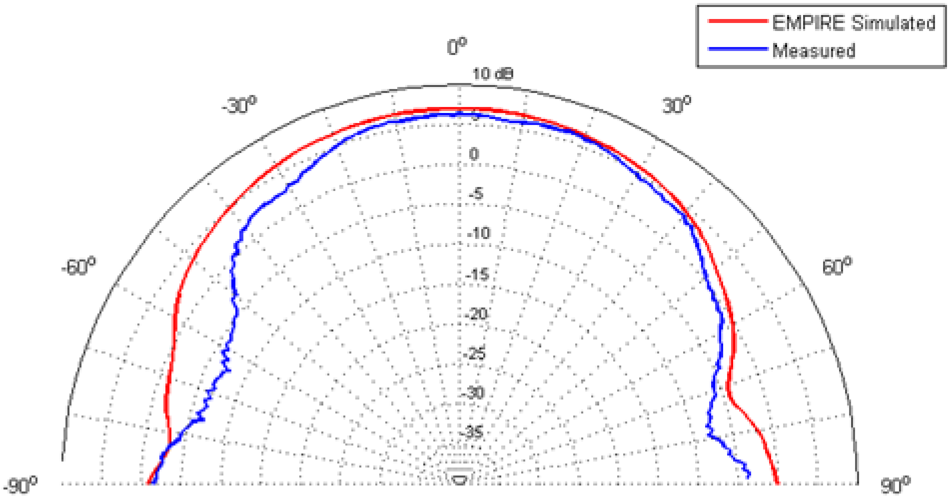

Figure 4.4-6 : Co-polarised computed and measured directivity patterns (dBi) of the 3-element Yagi in the H-plane

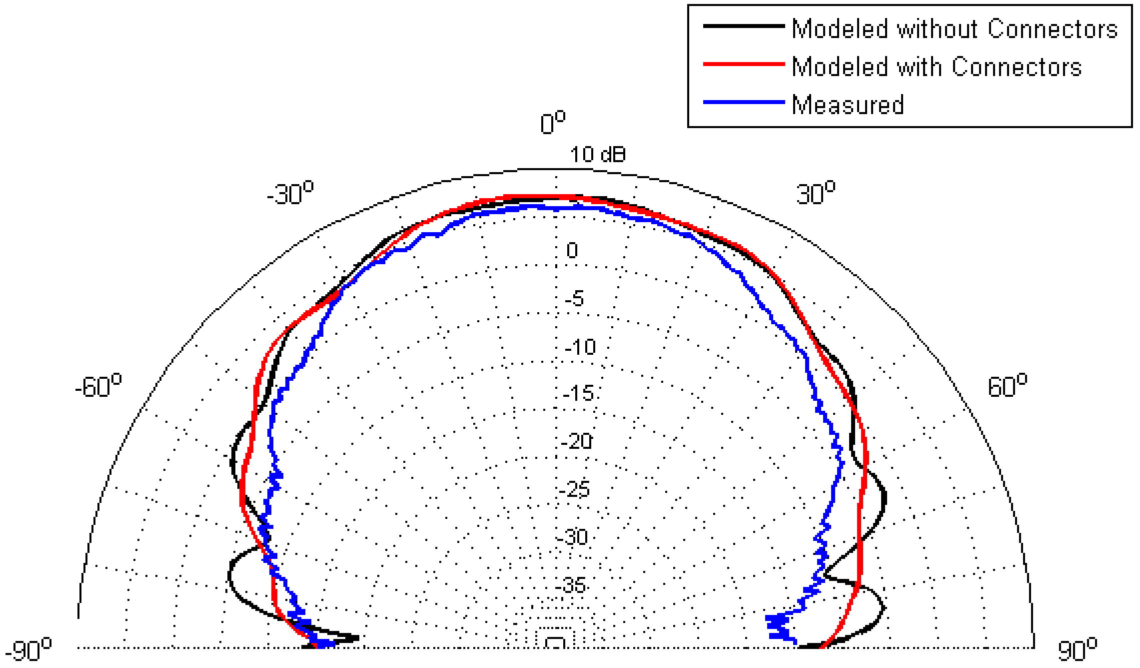

Figure 4.4-7 : Co-polarised computed (with and without connector boxes) and measured directivity patterns (dBi) of the 3-element Yagi in the E-plane at 30GHz.

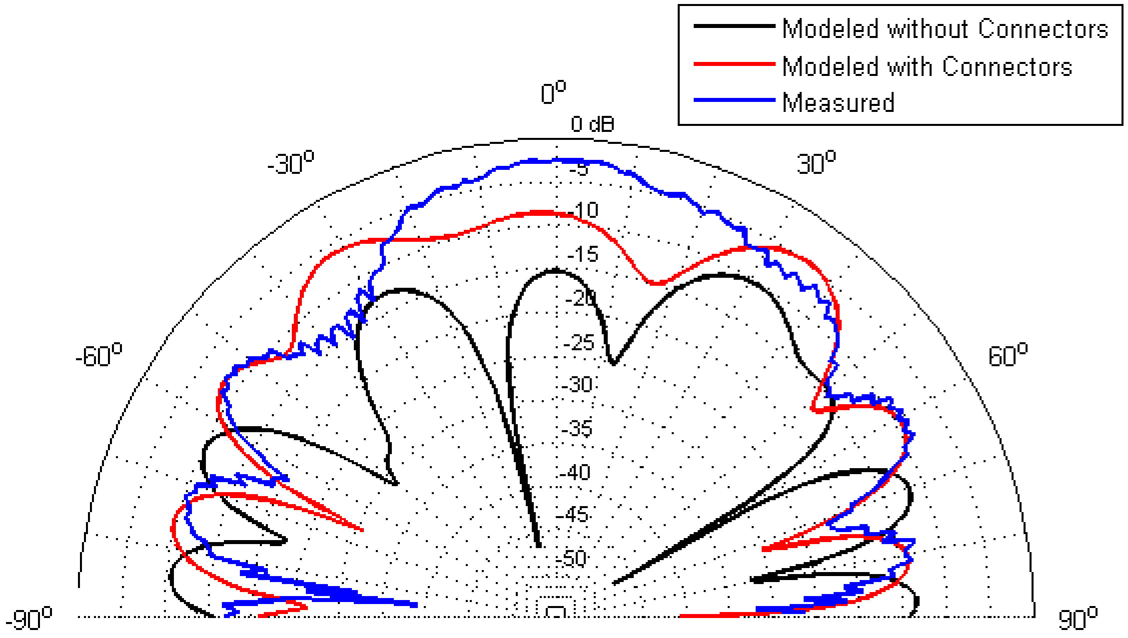

Figure 4.4-8 : Cross-polarised computed (with and without connector boxes) and measured directivity patterns (dBi) of the 3-element Yagi in the E-plane at 30GHz.

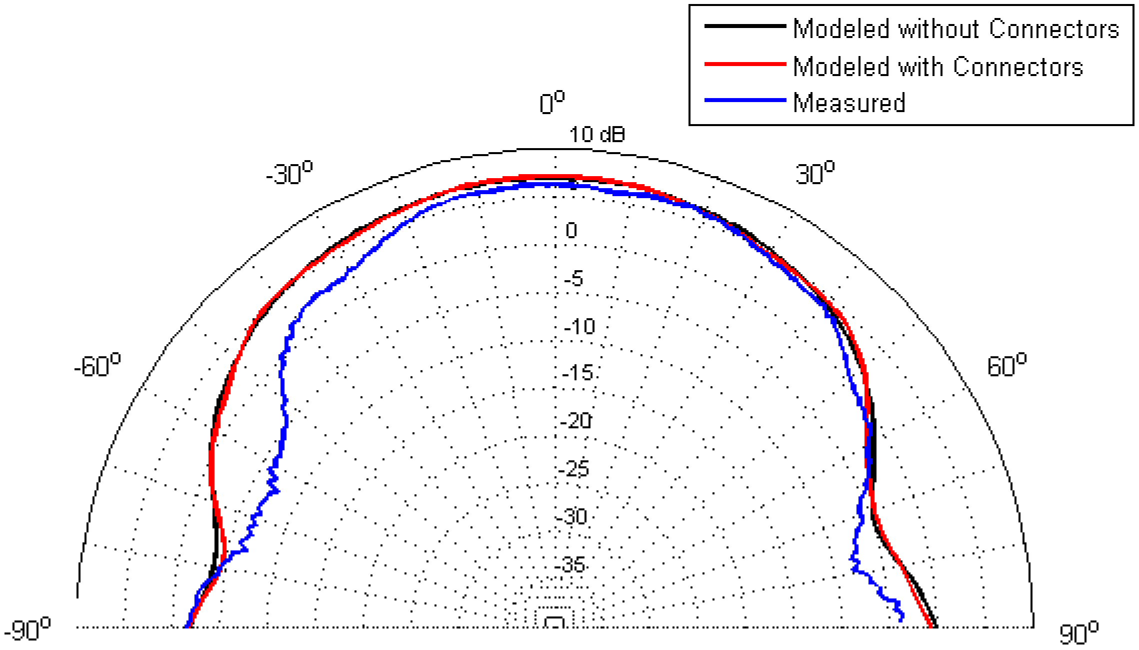

Figure 4.4-9 : Co-polarised computed (with and without connector boxes) and measured directivity patterns (dBi) of the 3-element Yagi in the H-plane at 30GHz.

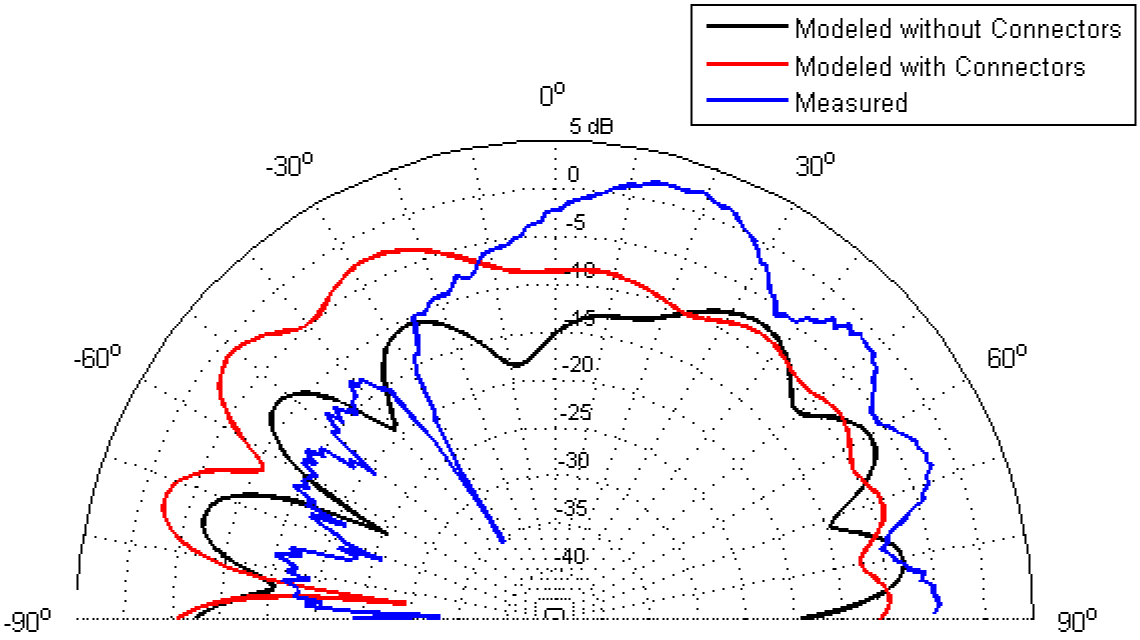

Figure 4.4-10 : Cross-polarised computed (with and without connector boxes) and measured directivity patterns (dBi) of the 3-element Yagi in the H-plane at 30GHz.

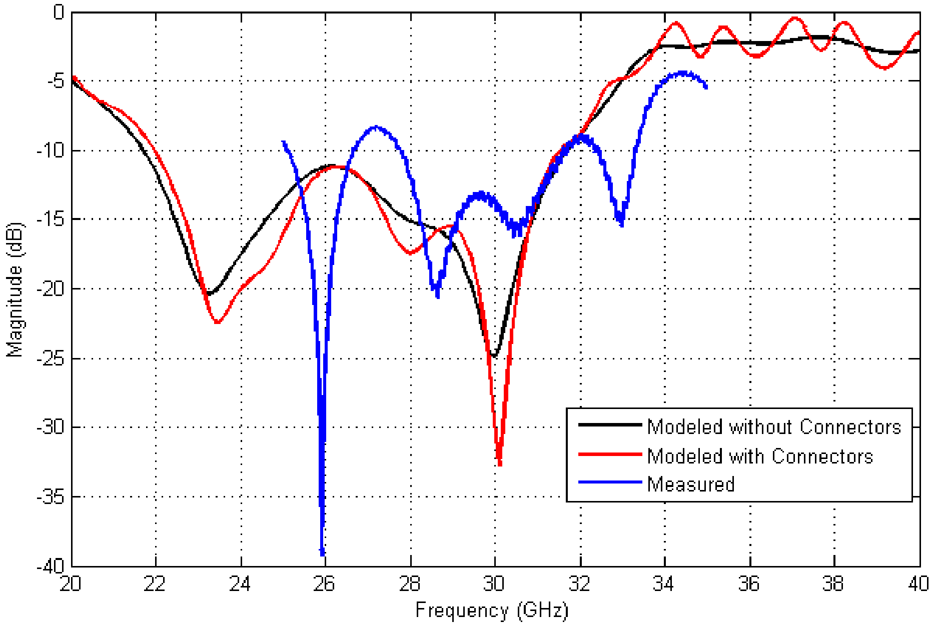

Figure 4.4-11 : Return Loss Comparison with Empire Modeling Results and Measured

4.4.4 Modelling Continuous Conducting Strips in EMPIRE

Two methods can be used in EMPIRE to generate continuous conducting strip holograms. In the first approach several points for each arc can be input essentially by hand, but many points are needed along each arc for good resolution (we will later refer to this as the point-by-point approach). This is accurate but laborious, and does not lend itself to numerical experiments where we wish to move the Yagi feed with respect to the hologram. The second approach is more convenient in such cases. A quicker way to draw these conductors is to use the "Arc" object available in EMPIRE. However, using the "Arc" object poses a problem. The reason is that these "Arcs" are defined by specifying their start angle and end angle, as illustrated in Figure 4.4-12.

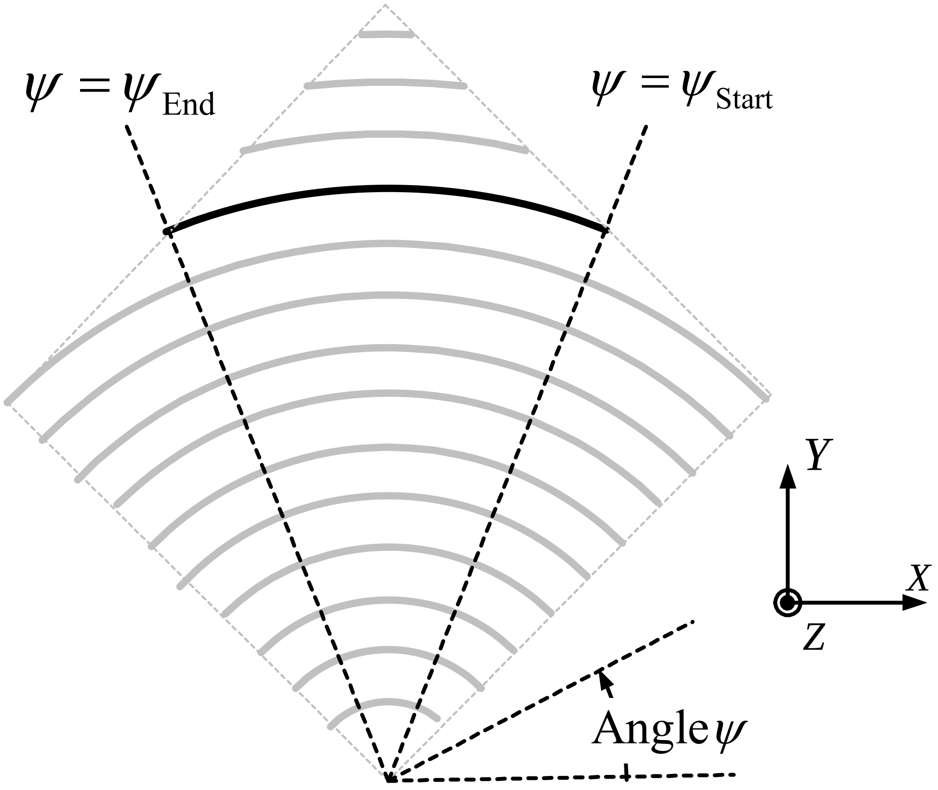

Figure 4.4-12 : Specification of "arc" conducting objects in EMPIRE

The procedure thus works well for the first few conducting rings. However, as one can see, the starting angle and ending angle will never end perpendicular to the edge of the substrate on the top portion of its diamond shaped boundary, and there might be a small piece of conductor hanging over the edge of the substrate. To determine whether this effect is significant we compared two sets of simulations, one where the very short pieces of conductor were left hanging off the dielectric substrate, and one where the conductors were individually clipped to fit the dielectric. The next few plots (refer to Figure 4.4-12 for coordinate axis definitions) will show that there is very little difference between the predicted far-field pattern using the point-by-point approach and the two "arc" approaches mentioned immediately above. The holographic antenna modelled was Hologram#3 of Table 2.5-1 with continuous conducting elements and the 3-element Yagi feed. As Figures 4.4-13 through 4.4-16 show, the "Arc" approach models the conductors as effectively as the point-by-point approach, and it will be used in the remainder of this thesis.

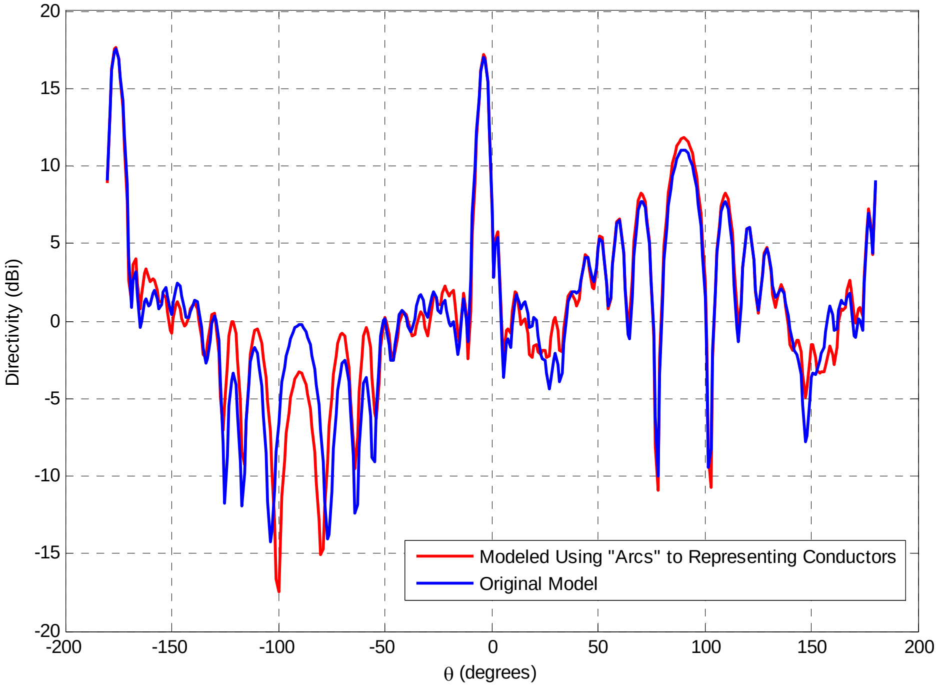

Figure 4.4-13 : Directivity pattern in the $\phi = 90^\circ$ cut at 29 GHz. The "original model" refers to the point-by-point method of generating the continuous circular strips.

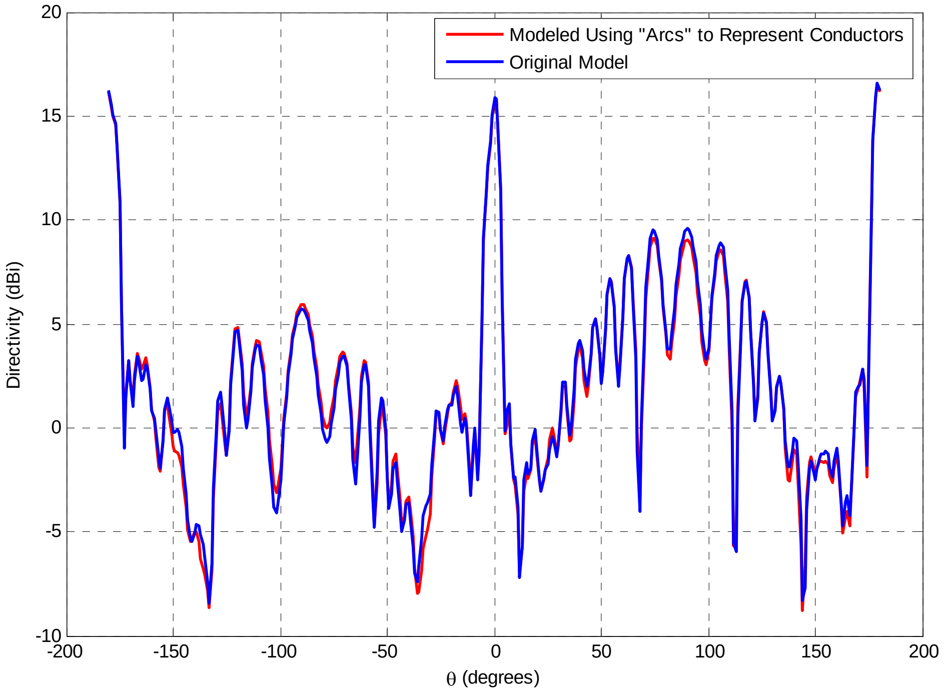

Figure 4.4-14 : Directivity pattern in the $\phi = 90^{\circ}$ cut at 30GHz. The "original model" refers to the point-by-point method of generating the continuous circular strips.

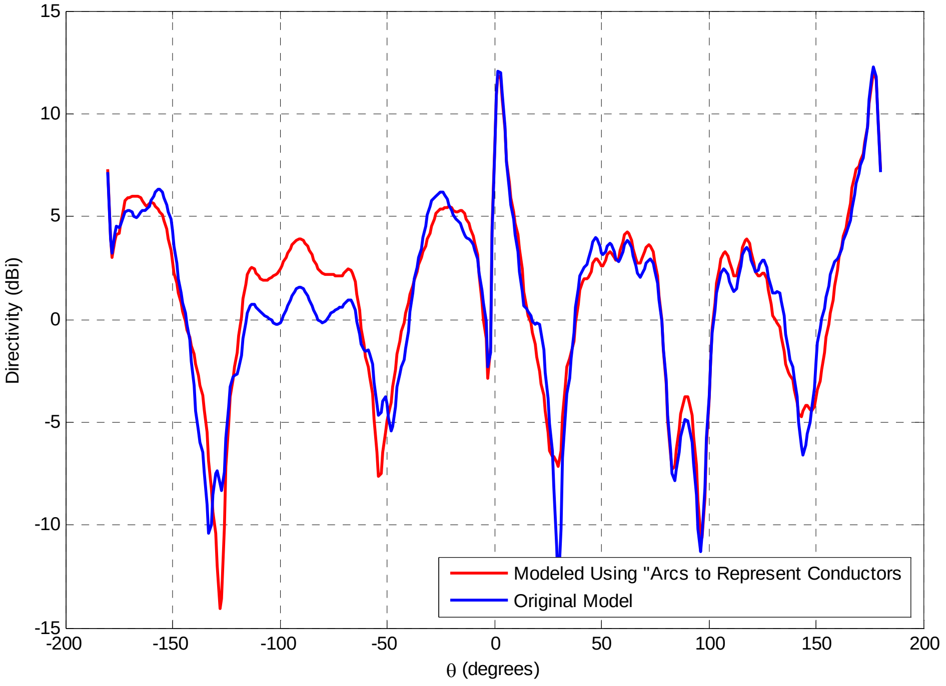

Figure 4.4-15 : Directivity pattern in the $\phi = 0^{\circ}$ cut at 31 GHz. The "original model" refers to the point-by-point method of generating the continuous circular strips.

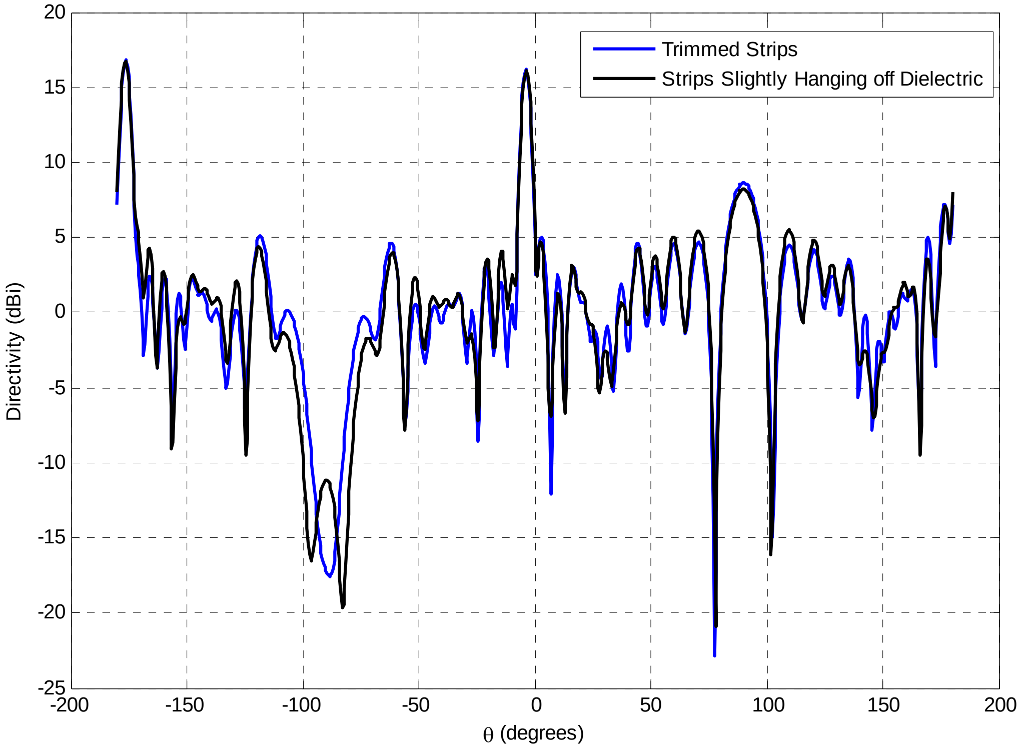

Figure 4.4-16 : Directivity pattern in the $\phi = 0^{\circ}$ cut at 29 GHz.

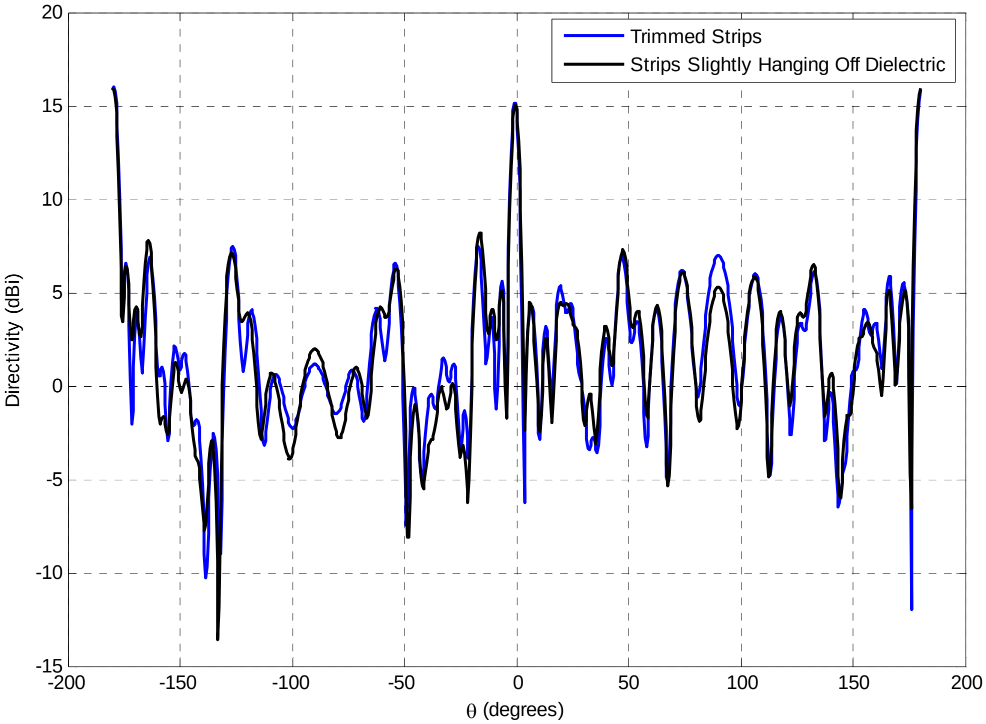

Figure 4.4-17 : Directivity pattern in the $\phi = 90^{\circ}$ at 30 GHz.

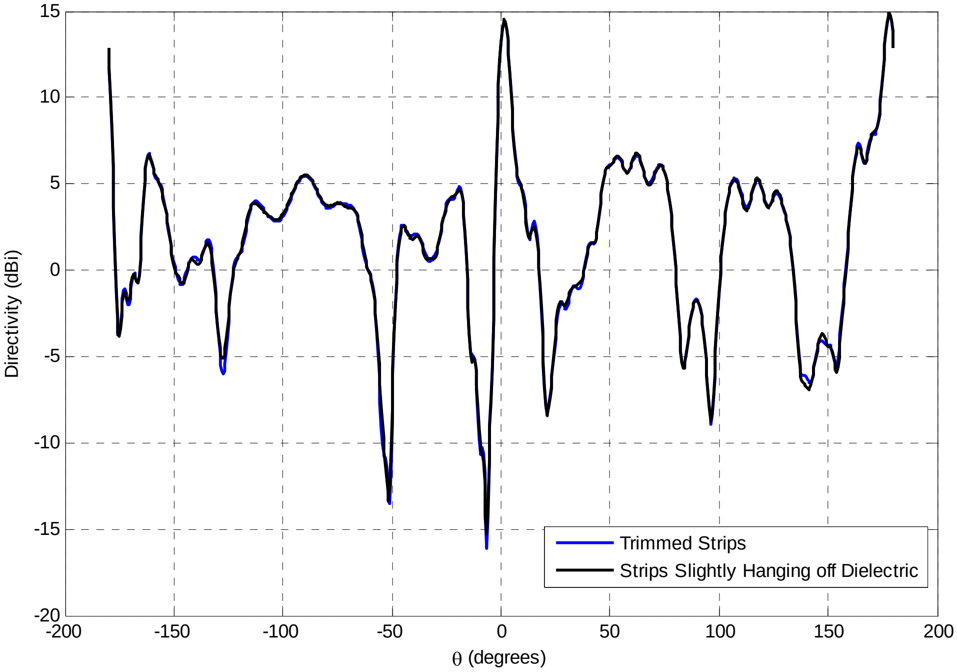

Figure 4.4-18 : Directivity pattern in the $\phi = 90^\circ$ cut 31 GHz.

4.5 CONCLUDING REMARKS

Several things have been established by the work of this chapter. We have discussed important issues related to the use of code FEKO in the modelling of planar holographic antennas, especially the careful modelling of microstrip geometries (viz. the port issues) when finite sized groundplanes and substrates need to be used. This information was not readily available and it took some computational experimentation to sort it out; it will be useful to readers who wish to use such microstrip feeding with any antenna type. In the process we have developed validated models of the Yagi and sectoral horn antennas we wish to use in Chapter 5. We have developed an algorithm (and implemented it in FEKO) to automatically lay out wire-dipole and strip-dipole holograms. These can be single- or double-layer. We have also successfully used FEKO (in Section 4.3.6) and EMPIRE (in Section 4.4.4) to model complete holographic antennas. In the next chapter we will use both of the modelling methods to examine various aspects of the operation of the planar holographic antenna.

One thing we discovered as part of the work of this chapter is that, unless one has access to unusually substantial computing resources which happen to have the FEKO or EMPIRE codes installed[15], the run times are just too long for numerical optimisation to be possible. The holographic antennas are just electrically too large.

4.6 REFERENCES FOR CHAPTER 4

[1] *FEKO*, EM Software & Systems Inc. (www.feko.info).

[2] *EMPIRE XCcel^{TM}*, IMST GmbH, Germany (www.empire.de).

[3] R.F.Harrington, *Time Harmonic Electromagnetic Fields* (McGraw-Hill, 1961)

[4] D.A.McNamara, Notes for the Course ELG7100 : *The Method of Moments in Electromagnetic Engineering*, University of Ottawa, Canada.

[5] A.Taflove and S.C.Hagness, *Computational Electrodynamics: The Finite-Difference Time-Domain Method* (Artech House, 2005).

[6] D.M.Sullivan, *Electromagnetic Simulation Using the FDTD Method* (IEEE Press, 2000).

[7] D.A.McNamara, School of Information Technology & Engineering, University of Ottawa, *Private Communication.*

---

[15] We have found that, whereas powerful parallel computational facilities are often available, the problem is that these do not usually have the FEKO and EMPIRE codes installed.

CHAPTER 5

Numerical Experimentation on the Planar Holographic Antenna

5.1 PRELIMINARY REMARKS

We begin by examining some basic assumptions made in all work on the planar holographic antenna, namely the form of the interference pattern that forms the basis for such antenna design. This is the subject of Section 5.2. Section 5.3 models, using the method of moments, a hologram fed by a sectoral horn to show the effect of spillover on holographic antenna directivity, compares the performance of holograms with continuous versus dipole elements, and computationally confirms the value of the best separation distance between the layers of a double-layer holographic antenna. In Section 5.4 we use FDTD modelling to examine the effect of feed location relative to the hologram, the effect of the hologram strip width, whether the use of interference pattern null locations based on detailed field models improves the antenna performance (or otherwise), and whether the connector and mounting blocks shown in Figure 1.2-2 (and needed pattern measurements) disturbs the measured patterns. Finally, Section 5.4 models the holographic antenna in the receive mode and shows that a "focal point" exists.

5.2 *IN SITU* INTERFERENCE PATTERNS

5.2.1 Interference Patterns for Diamond Shaped Substrate

The interference pattern obtained using a spherical primary wave (from an idealized point source) and an ideal plane wave as the secondary wave, was discussed in Section 2.4. In this section we wish to use a more rigorous electromagnetic analysis based on the FDTD method. We therefore modelled the following geometry using the EMPIRE code:

- Dielectric substrate of the same shape, dimensions, thickness and permittivity as will be used in the remainder of this chapter. No conducting strips (that is, no hologram) is present on the substrate.

- 3-Element printed Yagi antenna described in Section 2.4. This is excited in the transmit mode and provides the primary wave.

- An ideal x-polarised plane wave incident on the Yagi-substrate structure. This constitutes the secondary wave. The wave is incident in the $-\hat{z}$ direction (namely from the side of the substrate that contains the microstrip track, not that containing the groundplane of the Yagi radiator's feed line).

The geometry is shown in Figure 5.2-1. We will first present some results and then in Section 5.2.2 provide useful details on how this particular situation is described in EMPIRE. Figure 5.2-2 shows the total field E_x observed just above the substrate (in fact $0.082\,\mathrm{mm} \approx \lambda/120$ above the substrate), and the interefrence patterm dips ("nulls") are visible. Table 5-1 lists (in the second column) the interference pattern null locations obtained using the idealised analysis in Section 2.4 and (in the third column) the computationally rigorous *in situ* model results from Figure 5.2-2. These quantities are graphically compared in Figure 5.2-3. Observe that the one set is shifted with respect to the other, and that this shift is not constant. The differences are thus not simply due to a fixed factor ε_{eff}, but are appriximately so. However, the basic interference pattern idea is confirmed by this rigorous analysis. It can however be concluded that as more rings are added further away from the feed radiator the difference between the null locations will become larger.

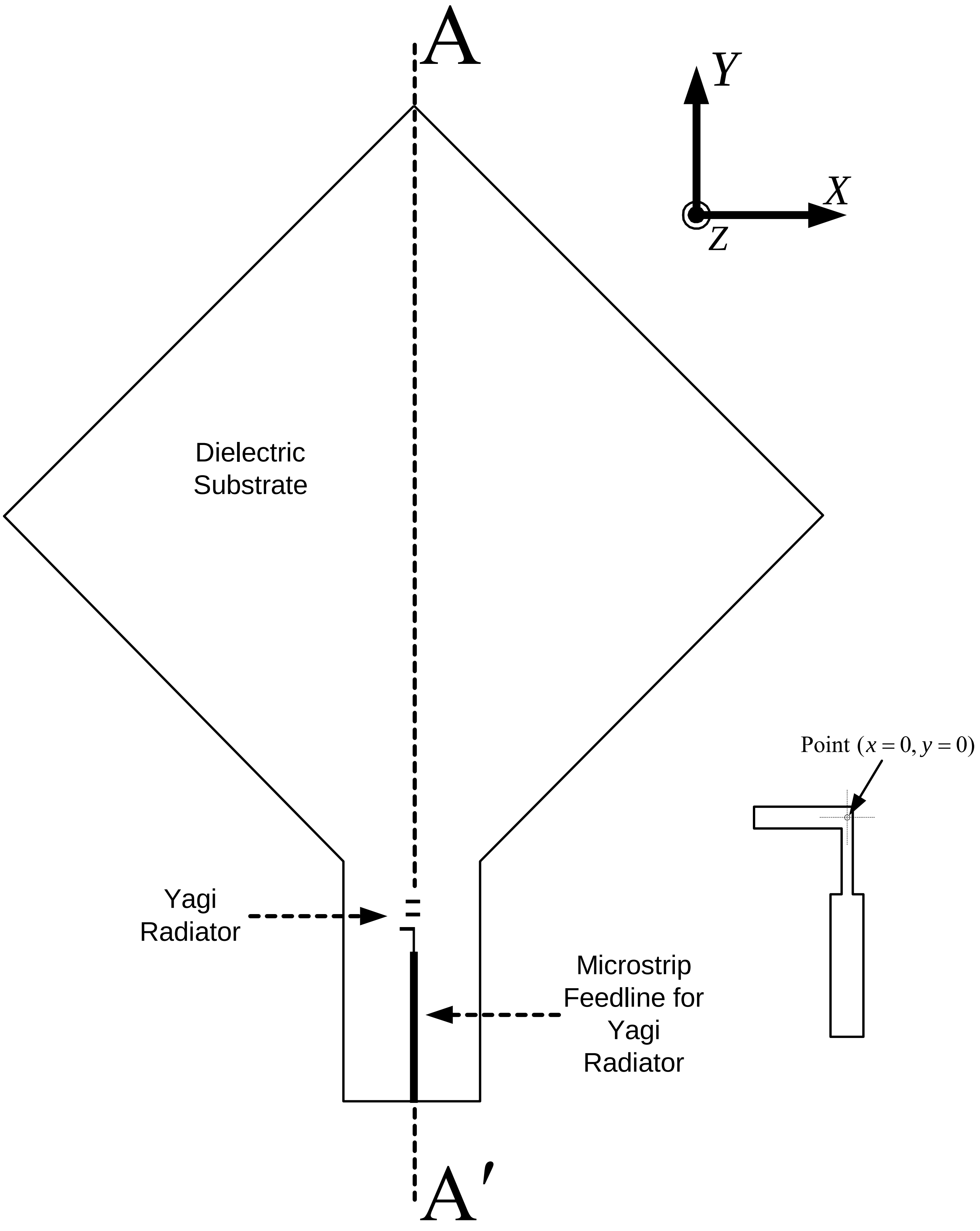

Figure 5.2-1 : Geometry used for the *in situ* computation of the interference pattern. Note that there are no hologram elements present.

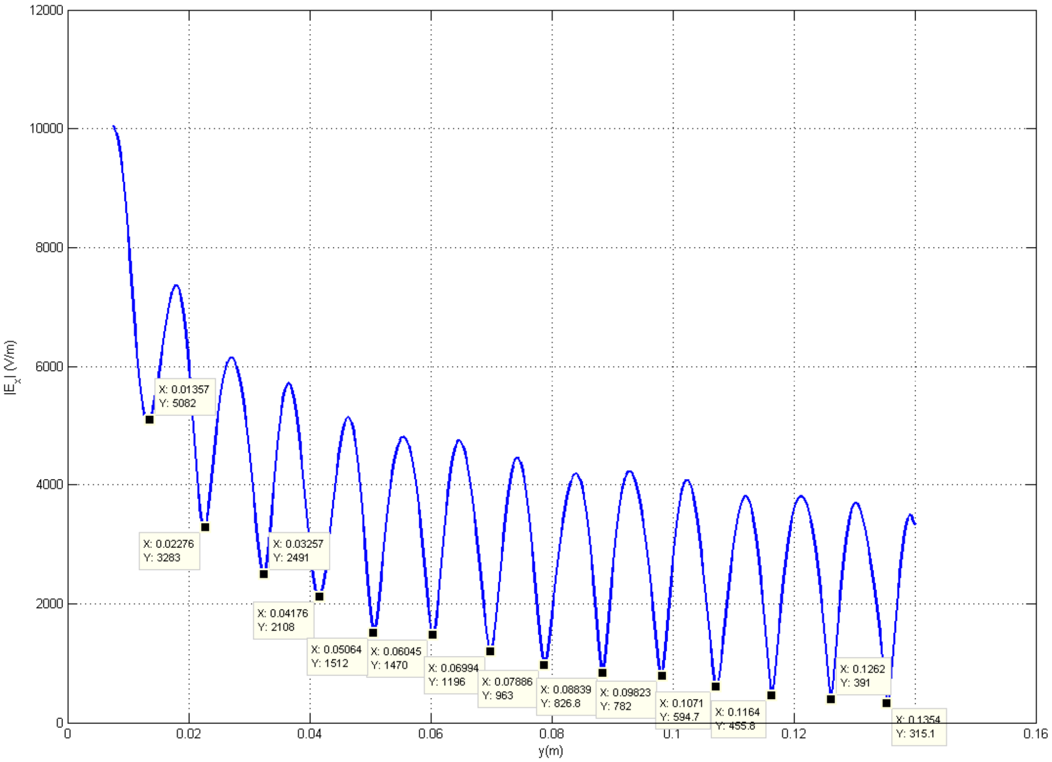

Figure 5.2-2 : Location of the Nulls along the Length of the Substrate at 30 GHz

Table 5.2-1 : Location of Nulls in Interference Pattern for Diamond Shaped Substrate[16]

Number	Null Ring Radius (m) Idealised Case (Expression 2.2-3) Hologram#1	Null Ring Radius (m) *In Situ* Case (Figure 5.2-2) Hologram#4	Null Ring Radius (m) Ref.[18] Hologram#3	Null Ring Radius (m) Idealised Case (Expression 2.2-4) Hologram#2
1	0.0162	0.0130	0.0146	0.01000
2	0.0254	0.0225	0.0240	0.02000
3	0.0356	0.0326	0.0334	0.03000
4	0.0456	0.0415	0.0428	0.04000
5	0.0552	0.0506	0.0552	0.05000
6	0.0656	0.0604	0.0615	0.06000
7	0.0756	0.0699	0.0709	0.07000
8	0.0856	0.0789	0.0803	0.08000
9	0.0958	0.0884	0.0897	0.09000
10	0.1058	0.0982	0.0991	0.10000
11	0.1159	0.1074	0.1085	0.11000
12	0.1260	0.1164	0.1179	0.12000
13	0.1360	0.1262	0.1273	0.13000
14	0.1460	0.1357	0.1367	0.14000

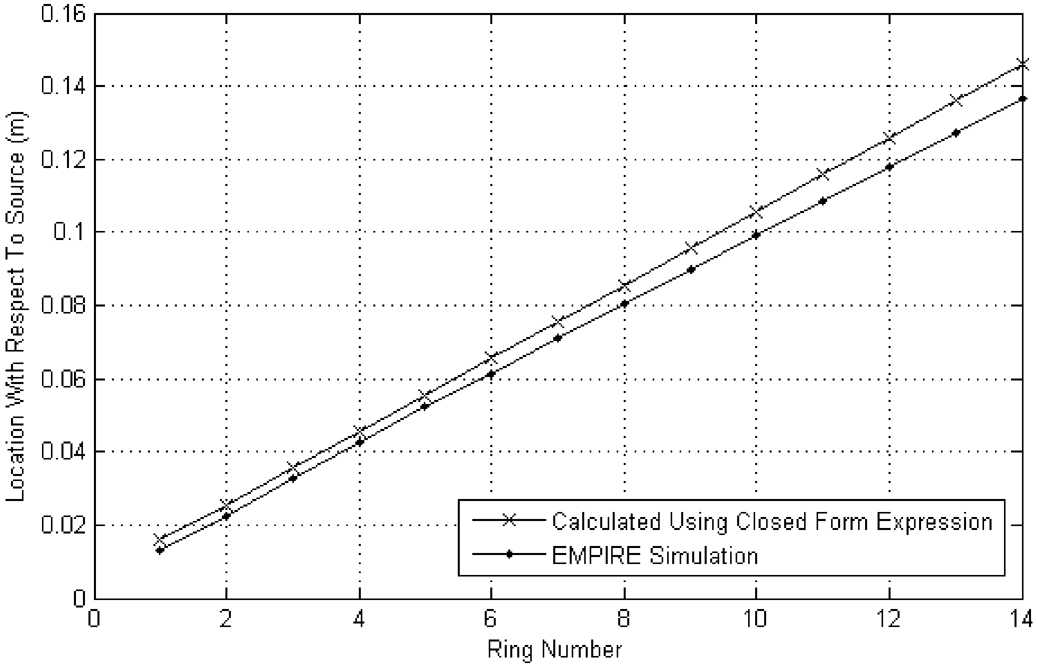

Figure 5.2-3 : Location of the Nulls along the Length of the Substrate at 30 GHz. The "closed form expression" is (2.2-3) and the "EMPIRE Simulation" values are those in Figure 5.2-2.

---

[16] This repeats some of the data already given in Table 2.5-1, for convenience.

5.2.2 Simulation Details Needed to Obtain the Interference Pattern Results

The simulation model in EMPIRE requires one to specify the magnitude and time delay of the microstrip line excitation for the Yagi radiator and that of the incident plane wave. The Yagi excitation is set using the so-called current (WC) and voltage (WV) weight factors, and the time delay (ED), in the EMPIRE microstrip port model. The plane wave wave is specified by selecting the magnitudes of the electric field components E_θ and E_ϕ, and its time-delay. The plane wave propagation direction in this case is $-\hat{z}$. In EMPIRE this direction is set by specifying the direction of a vector $\hat{k}$ in spherical coordinates, which in the present case requires a theta direction of 180° and a phi direction of 0°. The electric field of the plane wave illuminating the substrate is then E_x. The plane wave must be defined as being incident over the entire "computational box" (see Section 4.2.2) of the problem and not over some restricted region..

If these are both given unit amplitudes the interference pattern dips are not very distinct, and the plot of the total field along the central y-axis is as shown in Figure 5.2-4. By increasing the plane wave amplitude by a factor of 1000 is what provided the result in Figure 5.2-1. Changing the above amplitude may alter the depth of the dips but does not alter their location. This necessity of "playing" with the relative amplitudes of the sources of the primary and secondary sources to achieve a sufficiently distinct hologram is common in optical holography [1].

In order to actually obtain the electric field component E_x along the line indicated it is necessary in EMPIRE to request such data over a planar surface, but to define a restricted narrow output window about the y-axis in which actual data values are to be provided. If this in not done a rather unmanageably enormous dataset is output by the code.

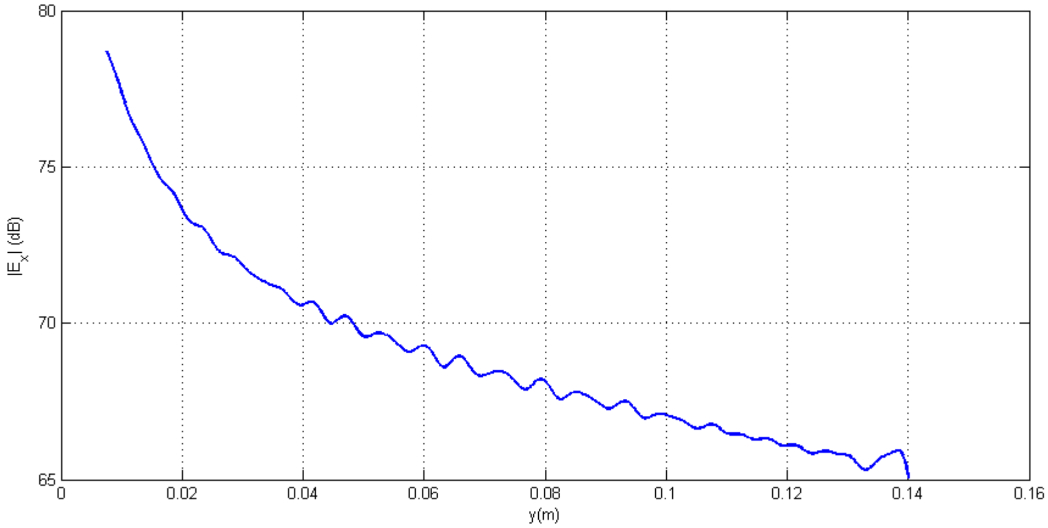

Figure 5.2-4 : Variation of the total electric field E_x along the substrate at 30 GHz

5.2.3 Interference Patterns for Substrates with Different Boundary Shapes

We wished to determine whether the shape of the substrate influences the location of the interference pattern nulls. The geometry shown in Figure 5.2-5 was therefore modelled, for three separate cases:

(a). All corners present.

(b). The top corners removed.

(c). The bottom corners removed.

Table 5.2-2 summarizes these findings. We observe that the substrate shape does not alter the null ring radii substantially.

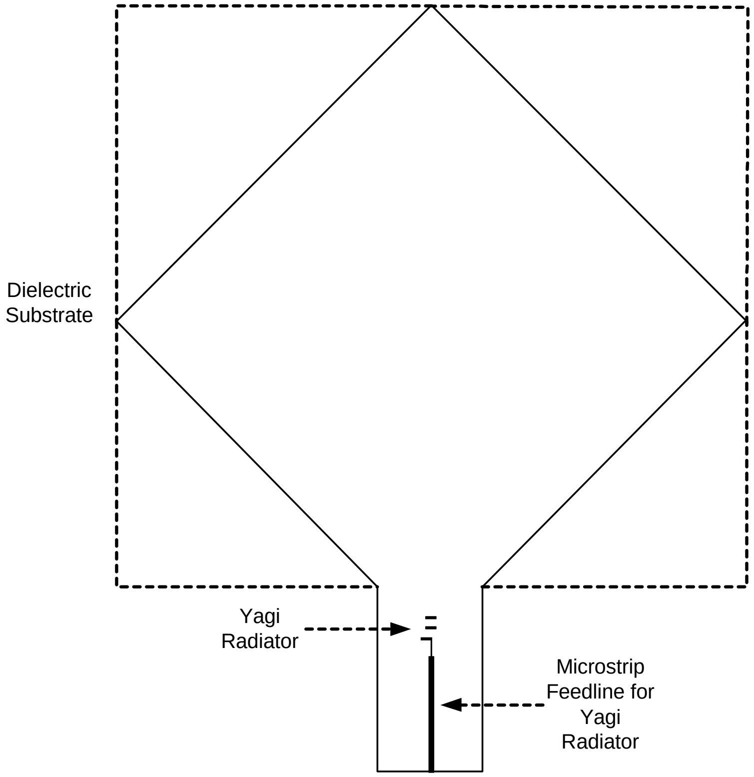

Figure 5.2-5 : Geometry used for the i*n situ* computation of the interference pattern with substrate "corners" shown

Table 5.2-2 : Location of Nulls in Interference Pattern for Various Substrate Shapes

All Four Corners Present (m)	Top Corners Removed (m)	Bottom Corners Removed (m)
0.01357	0.01512	0.01274
0.02246	0.02228	0.02228
0.03226	0.03230	0.03135
0.04115	0.04041	0.04089
0.05034	0.05043	0.04996
0.06045	0.05998	0.05950
0.06994	0.06904	0.06904
0.07855	0.07764	0.07812
0.08839	0.08767	0.08767
0.09792	0.09723	0.09675
0.10680	0.10580	0.10630
0.11610	0.11590	0.11540
0.12590	0.12540	0.12490
0.13540	0.13450	0.13450

5.3 TRANSMIT MODE ANALYSIS USING THE METHOD OF MOMENTS – THE FEED SPILLOVER PROBLEM

5.3.1 The Feed Spillover Problem

A sectoral horn such as that shown Figure 5.3-1 has been used to feed holographic antennas [2]. Its modelling in FEKO was discussed in Section 4.3.3. Figure 5.3-2 shows the H-plane plane patterns for the sectoral horn when the h_a parameter is changed and all the other parameters kept constant, using flare length $\ell = 81.53\,\text{mm}$. However, this caused the pattern to have a "flat top" for the larger values of h_a. This is due to the flare length of the horn being too small, and thus the flare rate being too large, for the higher values of h_a. The flare length was thus increased[17] to $\ell = 290\,\text{mm}$. This is quite a large horn. However, we simply wish to use it to provide us with a horn feed whose H-plane beamwidth can be controlled while keeping its E-plane beamwidth almost constant, in order to illustrate that much loss in directivity of holographic antennas is due to spillover, as was conjectured in [3].

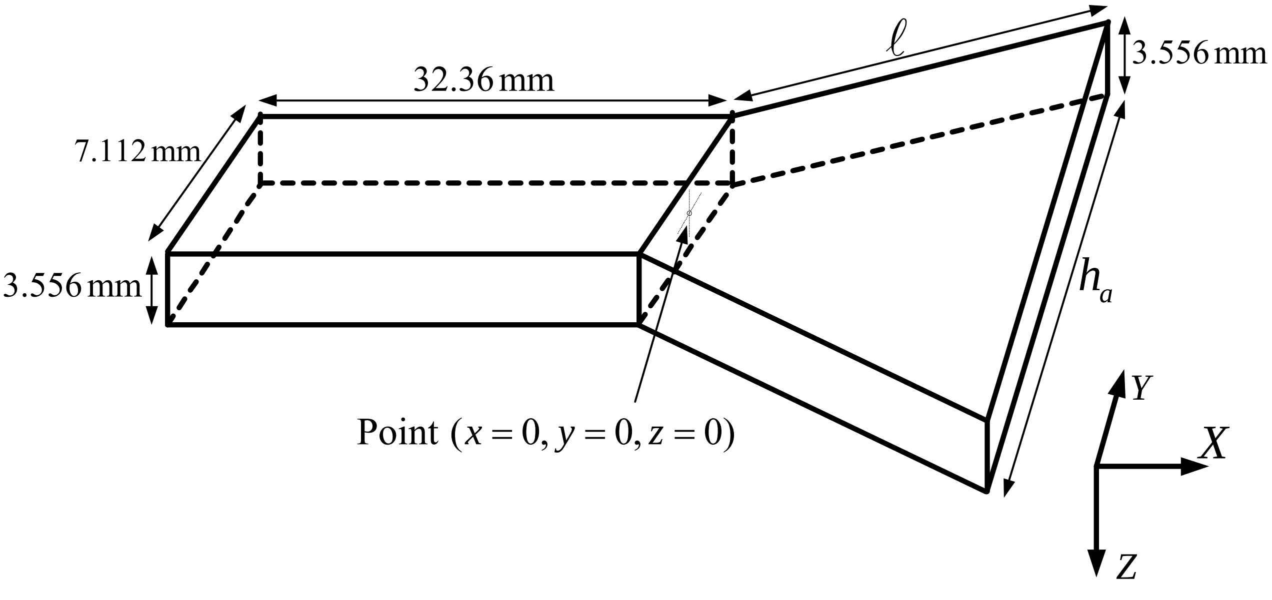

Figure 5.3-1 : Geometry of the E-plane sectoral horn antenna

Looking closely at the H-Plane cut in Figure 5.3-3 of the horn with the longer horn length it shows that as the width of the horn is increased the narrower the main beam becomes. However, the E-plane pattern beamwidths shown in Figure 5.3-4 are roughly constant. We have plotted

---

[17] Except for the largest width of h_a = 60mm where a flare length of 200mm was used to keep the number of unknowns to manageable proportions.

directivity patterns here; if we had shown these as normalised patterns these would have fallen almost on top of each other.

We next use the above horn to feed a two layer version of Hologram #2, consisting of wire dipole[18] elements. Figure 5.3-5 shows a portion of the horn-fed holographic antenna, and indicates the orientation of the sectoral horn with respect to the hologram. Only some of the dipole elements on the top layer are shown. The dipoles are situated on 14 rings whose radii differ by λ, as indicated. The separation between the dipole elements along the z-axis is seen to be $\lambda/2$. In the present case the distance between the horn aperture and the first dipole element is $h = \lambda/2$. The bottom layer of dipoles (not shown in Figure 5.3-2) is shifted a distance 0.4λ relative to the top layer along the positive x-axis direction. There are 198 dipoles on each layer[19]. The separation between the layers is $\lambda/4$; other separations were used but lead to the same conclusions, and so are not included here. There is no substrate present, for reasons mentioned in Section 4.3.7.

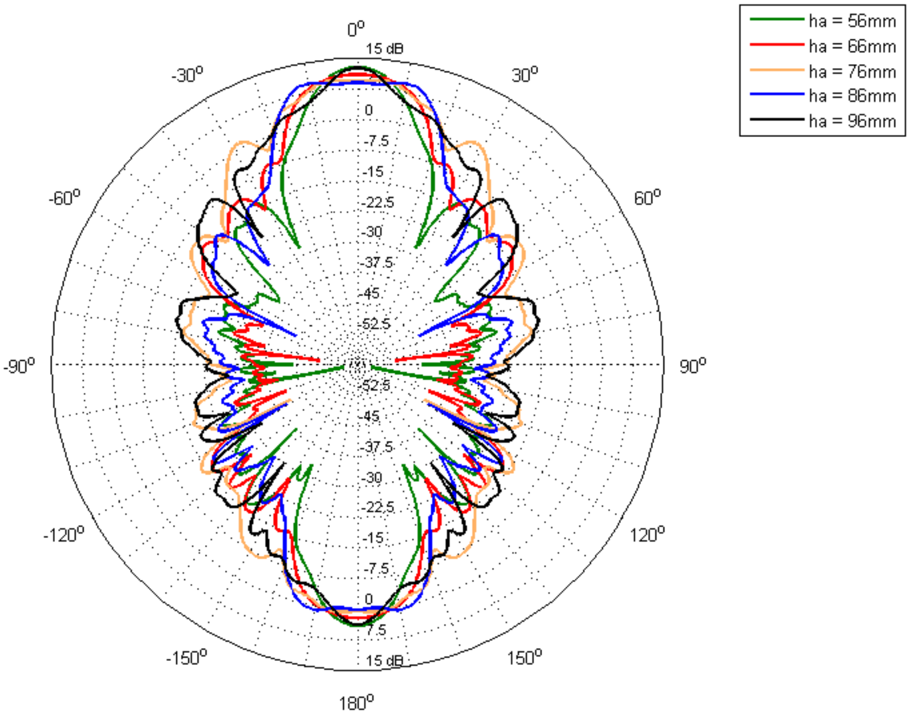

Figure 5.3-2 : Directivity patterns (dBi) of the sectoral horn with $\ell = 81.53\,mm$ in the H-plane for various values of aperture dimension h_a.

---

[18] This was done to save computer memory resources since, as noted elsewhere, the number of unknowns needed to model the horn is considerable. The number of unknowns needed for continuous wire arcs would have been more than that for the wire dipoles.

[19] The dipole closest to the horn aperture on each layer has been removed, for reasons mentioned in Section 4.36.

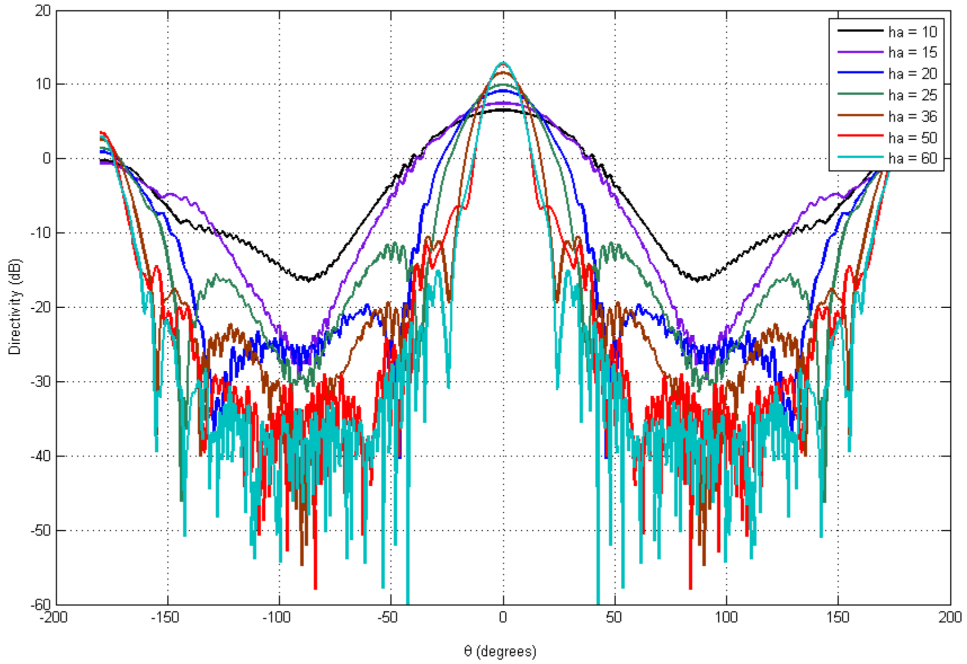

Figure 5.3-3 : Directivity patterns (dBi) of the sectoral horn with $\ell = 290\,mm$ in the H-plane for various values of aperture dimension h_a.

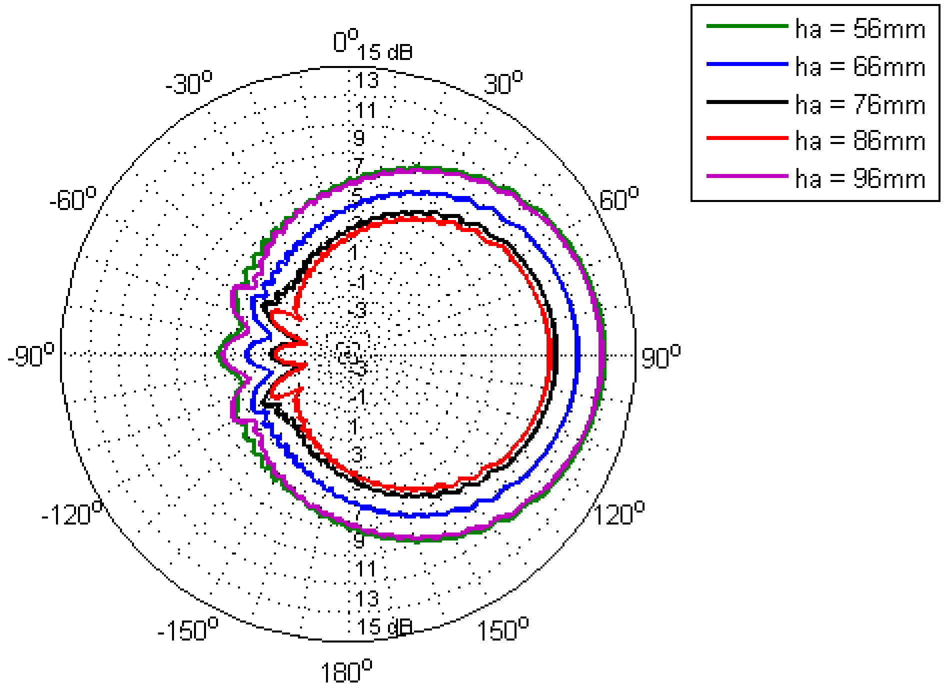

Figure 5.3-4 : Directivity patterns (dBi) of the sectoral horn with $\ell = 290\,mm$ in the E-plane for various values of aperture dimension h_a.

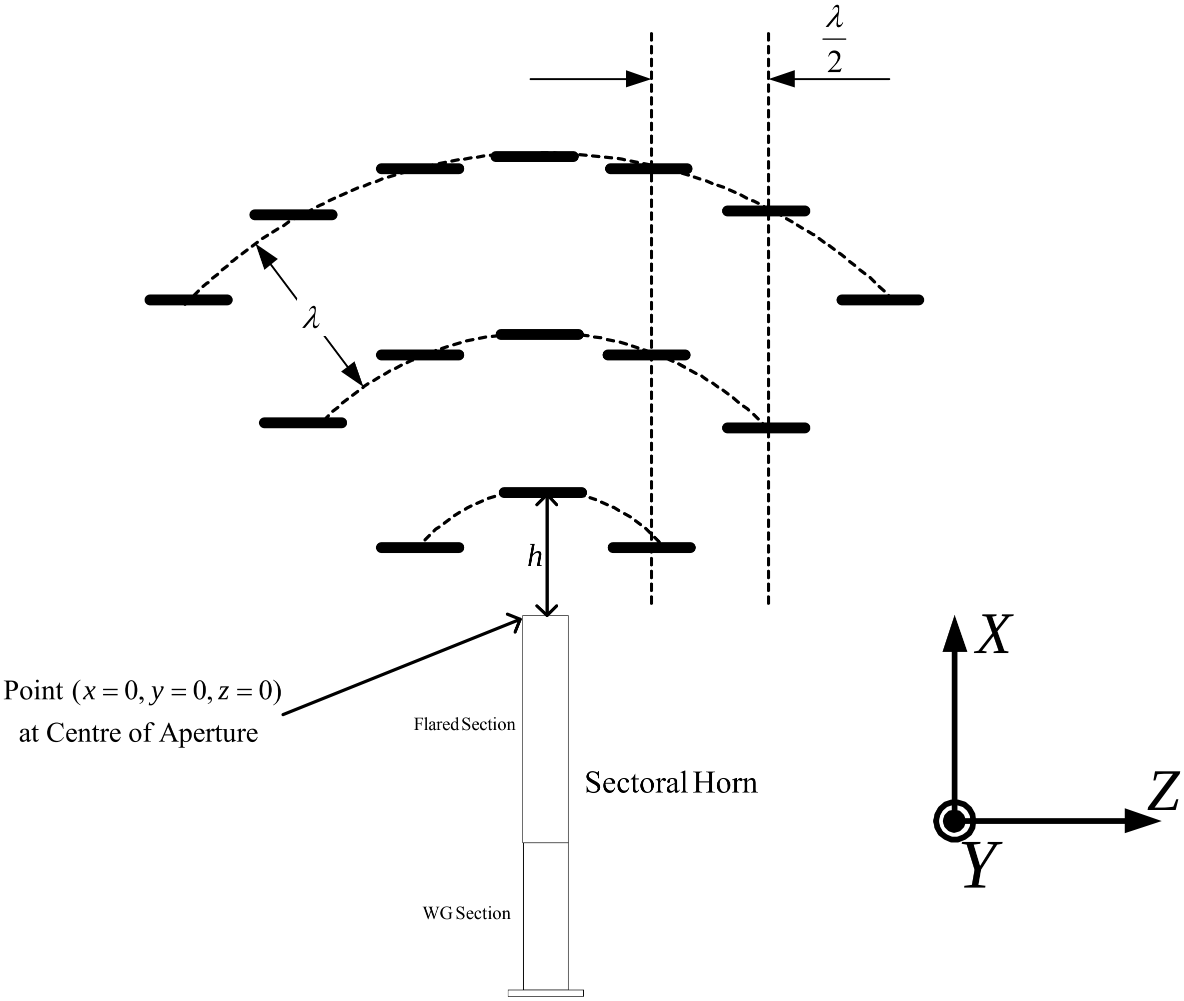

Figure 5.3-5 : Geometry of the sectoral horn fed double-layer wire dipole holographic antenna.

Figures 5.3-6 through 5.3-8 show the directivity patterns of the complete holographic antenna. Maximum directivity values in the broadside direction are summarised in Table 5.3-4 and plotted in Figure 5.3-9. As the horn H-plane beamwidth increases (for decreasing h_a) the maximum directivity of the complete holographic antenna decreases, a decrease that can be considerable. These simulations have highlighted a significant problem. When using a horn to illuminate the hologram it is possible to adjust the feed spillover in the H-plane by decreasing the horn's beamwidth in that plane through an increase in the value of h_a. If one uses a printed feed whose elements must all lie in the plane of the hologram, the feed must become very large to decrease the H-plane by similar amounts (if this is indeed at all possible). If, in order to reduce spillover, we require a feed whose directivity is close to that of the final holographic antenna, then the hologram is merely serving as a means of steering the beam by 90°.

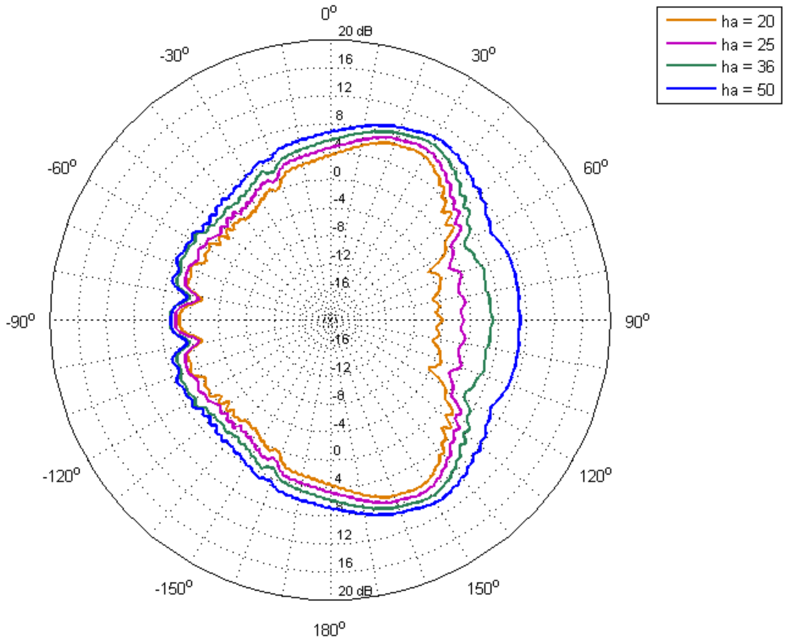

Figure 5.3-6 : Directivity pattern (dBi) at 30 GHz in the E-plane of the complete holographic antenna as the feed horn aperture width (h_a) is varied.

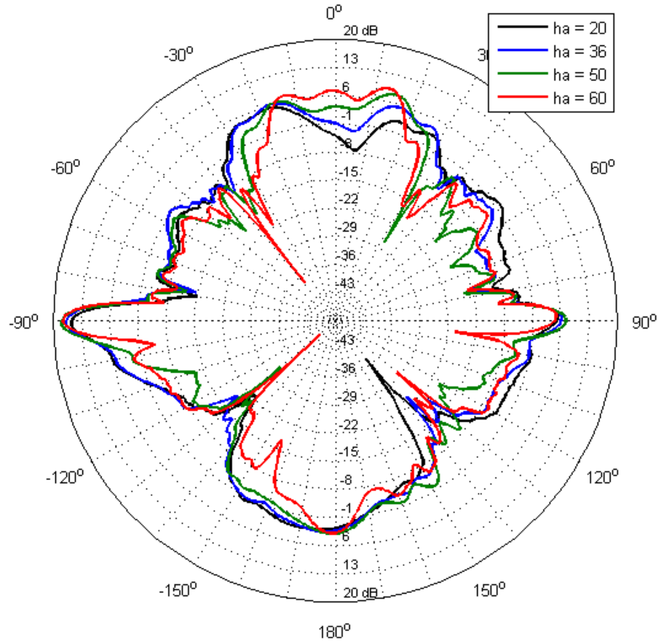

Figure 5.3-7 : Directivity pattern (dBi) at 30 GHz in the H-plane of the complete holographic antenna as the feed horn aperture width (h_a) is varied.

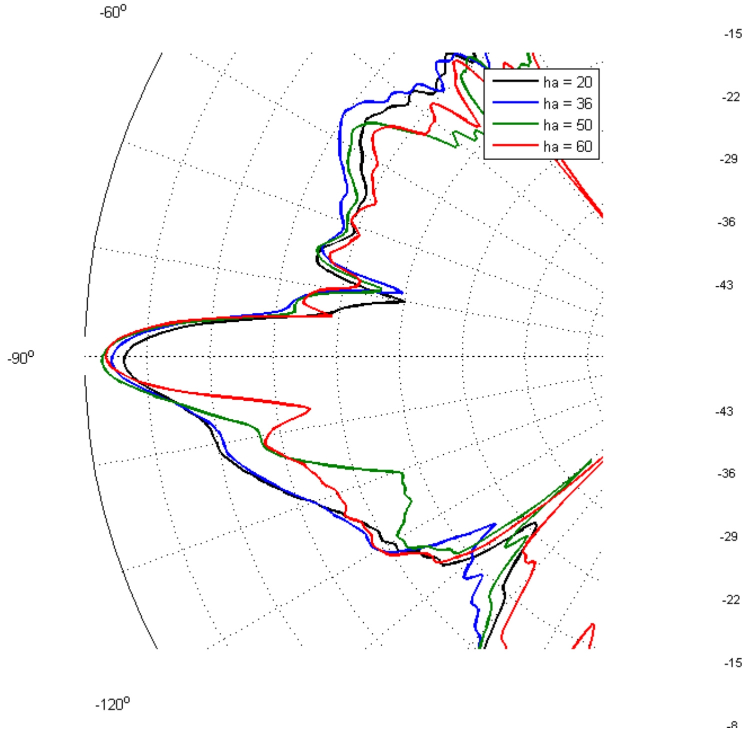

Figure 5.3-8 : Enlarged portion (in the vicinity of maximum directivity) of directivity pattern in Figure 5.3-7.

Table 5.3-1 : Maximum directivity of holographic antenna and beamwidth of feed horn versus the horn aperture dimension h_a

h_a (mm)	Maximum Directivity (dBi)	Approximate Beamwidth of Horn Alone (Degrees)
60	17.1234	50
50	18. 6358	30
36	17.6116	40
25	16.8951	70
20	15.3671	80
15	12.7437	180
10	12.7317	180

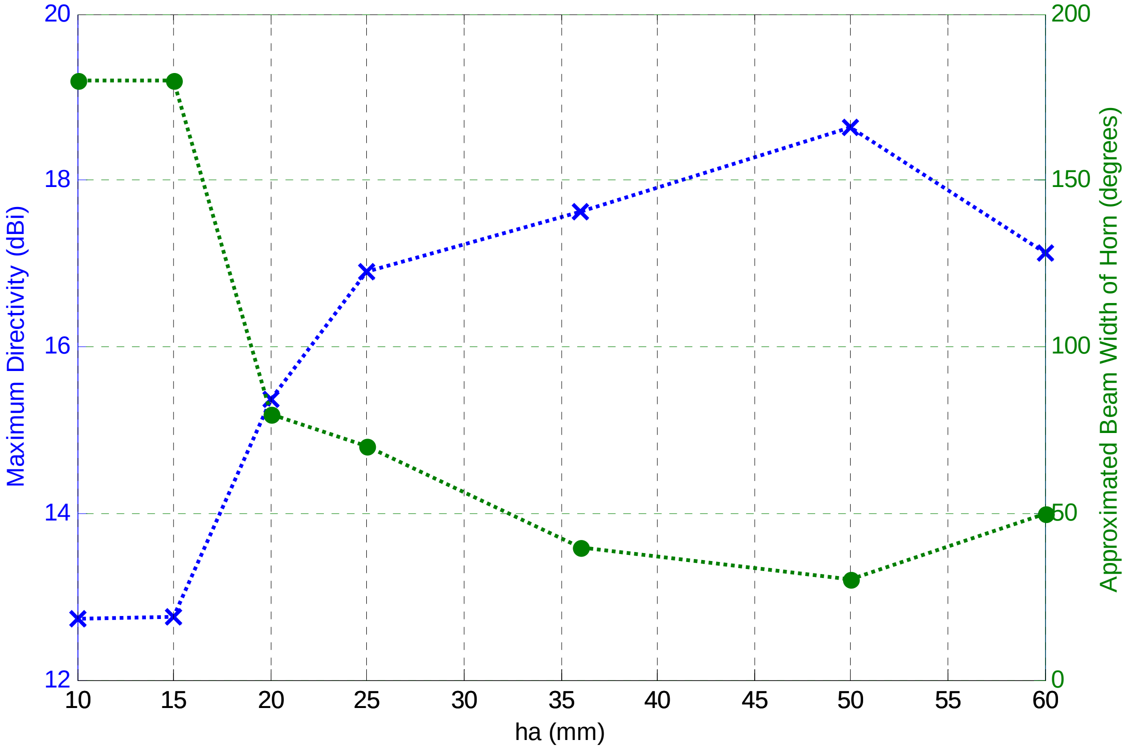

Figure 5.3-9 : Plot of the data from Table 5.3-1

We conjecture that directivity dependence on a Δh is due to a combination of the movement of the Yagi phase centre with frequency, and the interaction between the Yagi and the hologram. Being able to model it clearly allows one to determine the best location with all such effects taken into account.

5.3.2 The Effect of the Separation Between the Hologram Layers

In this section we model the same hologram as in Section 5.3.1 but use the 6-element Yagi (from Section 2.4) instead of the sectoral horn to illuminate the hologram. The FEKO model is illustrated[20] in Figure 5.3-10. The effect of the separation distance between the hologram layers is shown in Figure 5.3-11. It is clear that the best separation distance is $\lambda/4$, as argued from basic principles in [2], and that the maximum directivity indeed occurs here because of the decrease in the backlobe level.

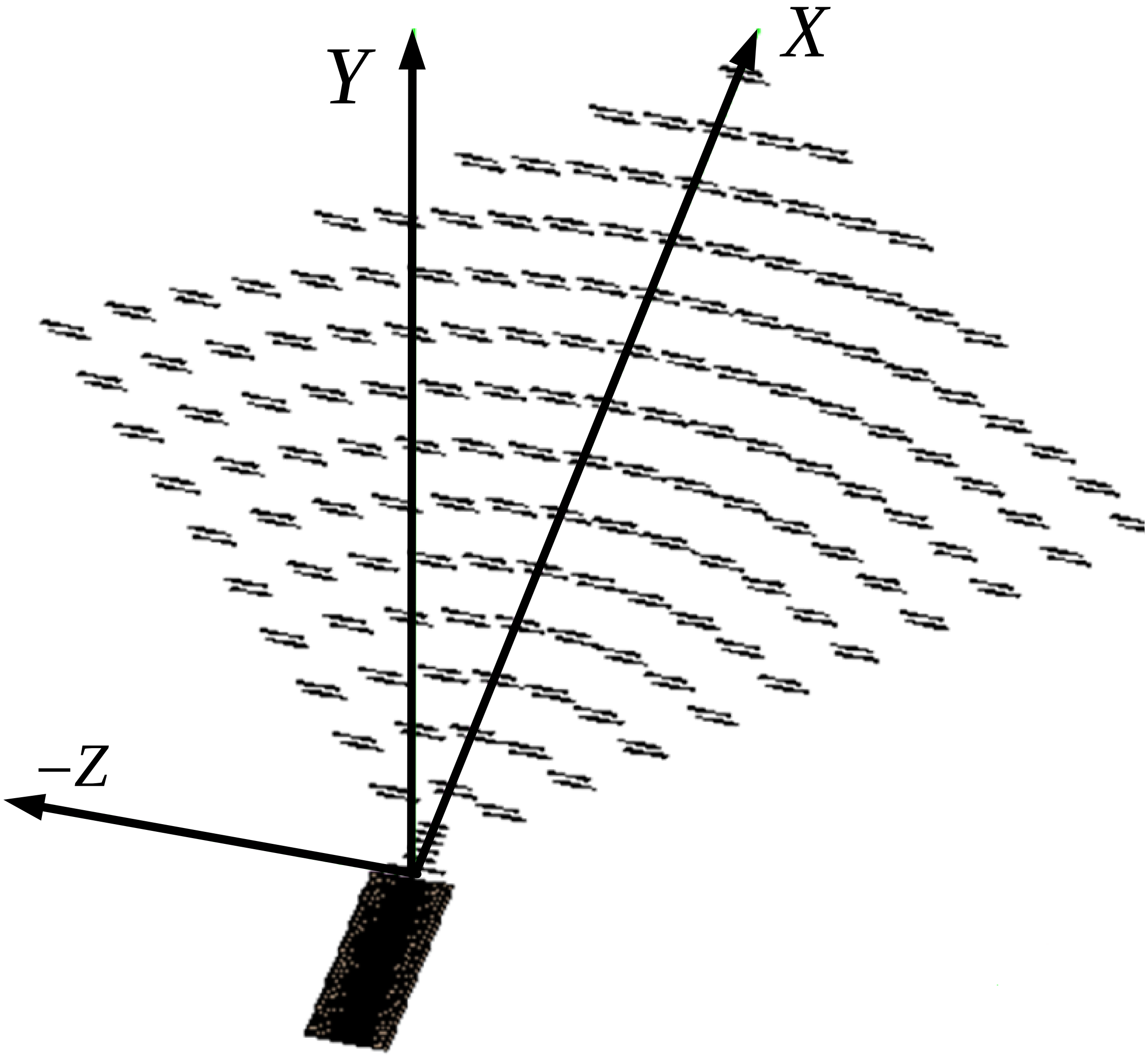

Figure 5.3-10 : FEKO model of the double-layer version of Hologram#2 with conducting strip dipoles and a 6-element Yagi feed.

---

[20] This is simply meant to provided a qualitative perspective.

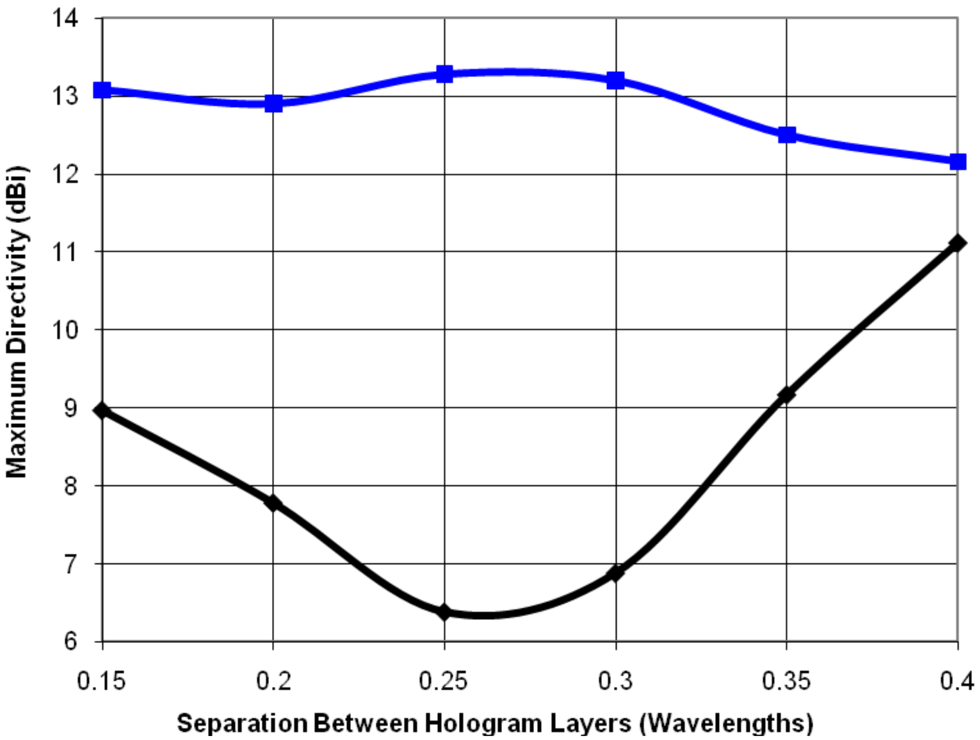

Figure 5.3-11 : Effect of separation between the layers on the maximum directivity in the favoured broadside direction (——), and backlobe level (——), of the double-layer holographic antenna.

5.3.3 Strip Dipoles Versus Continuous Conducting Strips

In this section we model the same hologram as in Section 5.3.1 but only a single layer, and use the 6-element Yagi (from Section 2.4) instead of the sectoral horn to illuminate the hologram. In addition, we replace the wire dipoles by conducting strip dipoles[21]. Furthermore, we will also model the hologram with the strip dipole elements replaced by continuous conducting strips[22]. The two types of elements can be compared by examining their computed directivity patterns shown in Figure 5.3-12. There is clearly the potential to obtain a slightly higher maximum directivity with the use of strip dipoles, in addition to the lower cross-polarisation levels observed in [2].

---

[21] The number of unknowns freed up by our not having to model the sectoral horn allows us to now use strip dipoles (each of which requires more unknowns than a wire dipole of the same length).

[22] Once again of width 0.254 mm.

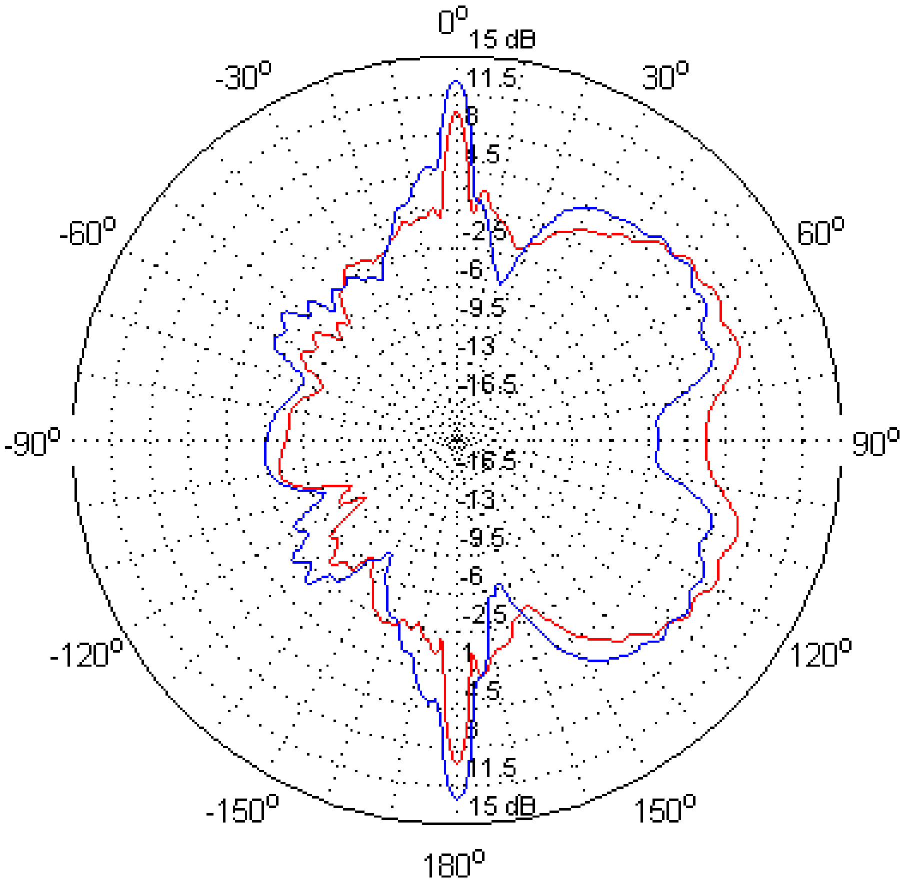

Figure 5.3-12 : Computed directivity patterns of the complete holographic antenna with strip dipoles (▬) and continuous strips (▬).

5.4 TRANSMIT MODE ANALYSIS USING THE FDTD METHOD

5.4.1 Immediate Goals

In this section we will use EMPIRE to model a single-layer version of Hologram#3 with continuous conducting strips (initially of width 0.254mm), fed using the 3-element Yagi radiator, and taking into account the substrate of thickness 0.508mm and relative permittivity 3.38. This is illustrated in Figure 5.4-1, and is in fact that shown in the photo in Figure 1.2-2, which was taken from [4]. We wish to use this model in order to examine (a). the effect of feed location relative to the hologram, (b). the effect of the hologram strip width, (c). whether the use of *in situ* null locations improves the antenna performance (or otherwise), and (d). whether the connector and mounting blocks shown in Figure 1.2-2 (and needed for pattern measurements) are deleterious to such measurements.

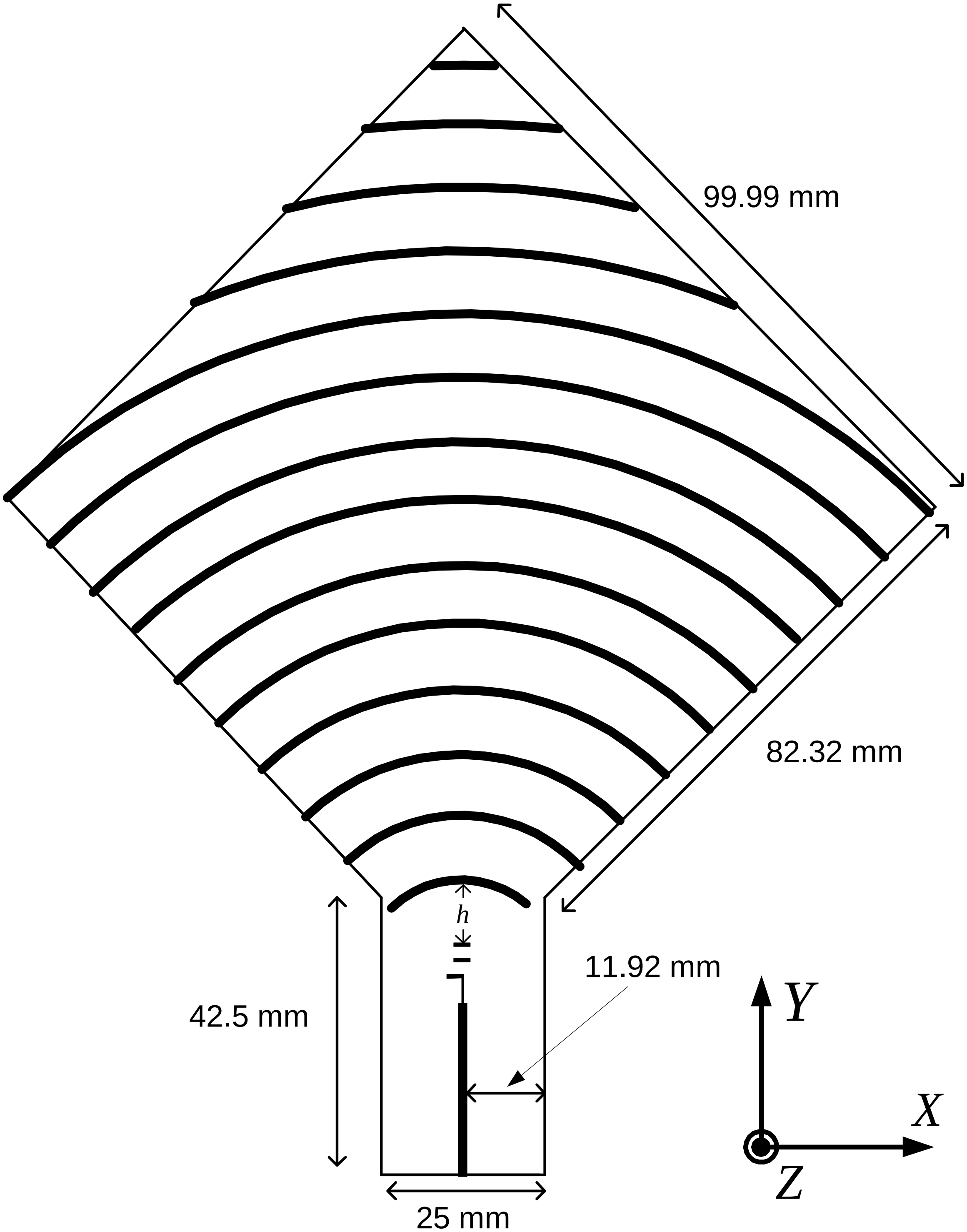

Figure 5.4-1 : Illustration of the holographic antenna modelled in Section 5.4.

5.4.2 The Effect of the Location of the Printed Feed Relative to the Hologram

The reference location of the Yagi feed is that when the point $(x = 0, y = 0)$ shown in Figure 5.2-1 coincides with the origin of the rings of the hologram. Directivity pattern information to be given can be understood with reference to the origin of the coordinate axes shown as an inset to Figure 5.4-1. The movement of the Yagi relative to the hologram can be described in terms of the change in the value of distance h. Figure 5.4-2 summarises the maximum directivity changes as the value of h increases[23]. Movement of the Yagi away from the reference position by 6mm increases the maximum directivity by as much as 1dB. Observe that the directivity is not the same in the two possible broadside directions, and differ by as much as 1dB. This asymmetry can only be due to two things : (a). the fact that the hologram elements are on one side of the substrate and, (b). the inherent asymmetry of the Yagi radiator if we wish it to be microstrip fed. Moving the Yagi closer to the hologram was found to decrease the maximum directivity.

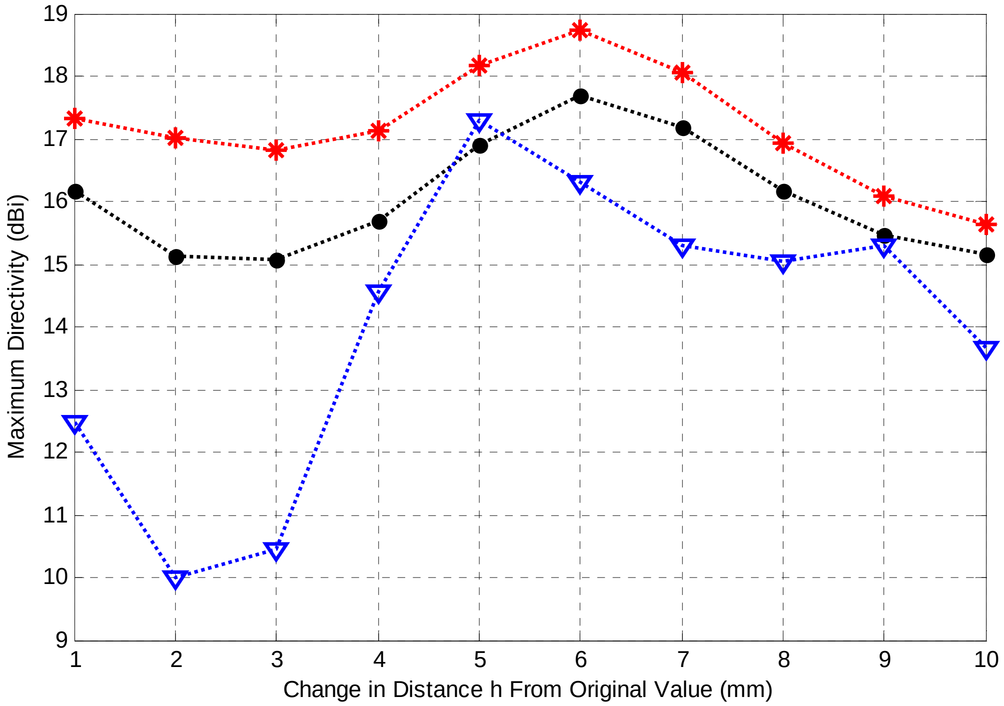

Figure 5.4-2 : Maximum directivity as source is moved away from its original position, in the θ = 0° direction at 29 GHz (∗∗∗∗), in the θ = 180° direction at 29 GHz (●●●●), and lastly the largest value in the θ = 0° or θ = 180° at 30 GHz (∇∇∇∇).

---

[23] As the Yagi is moved away from the hologram we extend the lower portion of the substrate (that is, more dielectric material is added) in the EMPIRE model.

5.4.3 The Effect of the Hologram Strip Width

The width of the continuous conducting strips of the hologram was taken as 0.254mm (254 μm), which is the narrowest that can usually be etched with standard etching facilities. We investigated what the effect would be if this width were actually increased. The outcome of these simulations are summarised in Table 5.4-1. This tabulated data shows that with a slight change combination of both increasing the strip width by 200 μm and shifting the Yagi 6mm away from its original position, a 18.96 dBi maximum directivity is achieved at 29 GHz. However, this is only a 0.2 dBi increase over the directivity shown in Figure 5.4-2 for the 254 μm width and 6mm translation of the Yagi. Firm conclusions cannot be drawn in any general sense.

Table 5.4-1 : Effect, on maximum directivity, of increasing the conducting strip width

Additional[24] Strip Width Added (μm)	At 29 GHz		At 30 GHz	
	Original Source Position	Yagi Moved 6mm Away from Original Position	Original Source Position	Yagi Moved 6mm Away from Original Position
100	17.74 dBi	18.83 dBi	16.88 dBi	17.08 dBi
200	17.8 dBi	18.96 dBi	16.61 dBi	16.94 dBi
400	17.82 dBi	18.85 dBi	17.17 dBi	17.68 dBi
600	17.71 dBi	18.83 dBi	17.84 dBi	18.22 dBi
800	17.47 dBi	18.75 dBi	17.98 dBi	18.86 dBi
1000	17.23 dBi	18.63 dBi	17.85 dBi	18.91 dBi

5.4.4 Utilisation of the *In Situ* Null Locations

The question arises as to whether use of the null locations determined in Section 5.2 make any significant difference to the performance of the holographic antenna. We therefore modelled the following continuous strip holographic antennas (both using the 3-element Yagi feed radiator):

(a). Continuous strips placed in the null locations of Hologram#3 of Table 5.2-1.

(b). Continuous strips placed in the *in situ* null locations of Hologram#4 of Table 5.2-1.

The computed directivity patterns are compared in Figure 5.4-3. The beamwidth of the broadside main lobes for case (b) are narrower and more symmetrical. However, the actual maximum

---

[24] That is, adding the amount in this column to the existing width of 254 μm.

directivity is slightly higher for case (a). It would appear that use of in situ null locations does not drastically improve the holographic antenna performance.

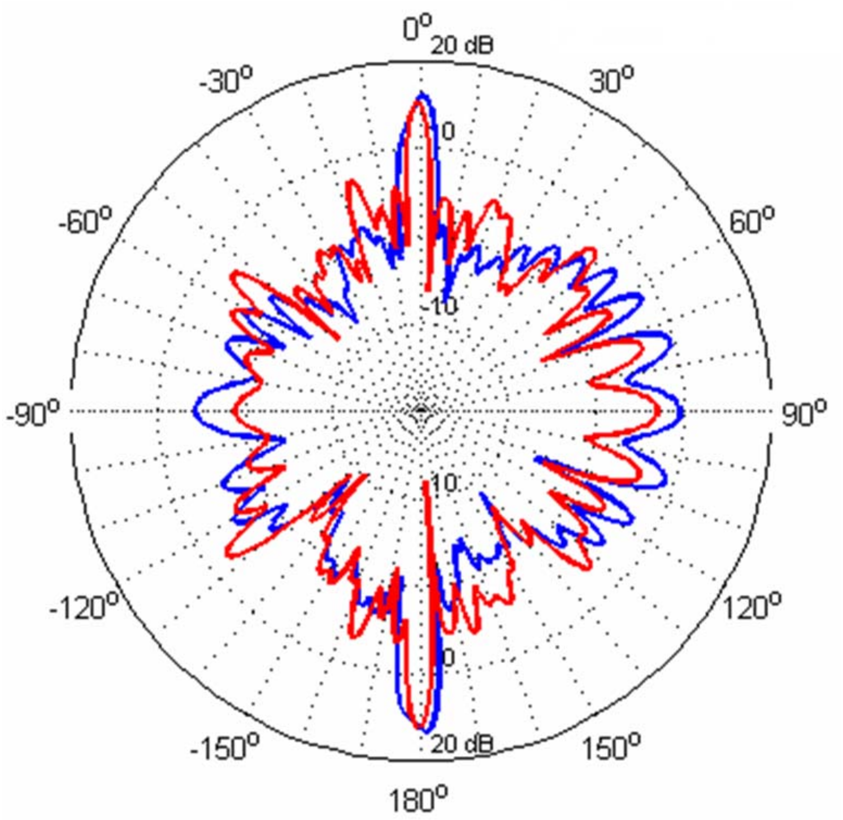

Figure 5.4-3 : H-plane directivity pattern (dBi) comparison between hologram#2 (—) and the hologram with conducting strips placed in the null locations from Section 5.2 (—). In both cases the hologram is fed by the same 3-element Yagi radiator.

5.4.5 The Effect of Connector and Mounting Blocks on the Radiation Pattern

A glance at Figure 1.2-2 shows that a connector and mounting block is needed when radiation pattern measurements are done on holographic antenna hardware. There is always the nagging doubt as to how this influences the measured patterns. We have therefore added these conducting blocks to the EMPIRE model that has been used thus far in this Section 5.4. Without these conducting blocks added to the model we obtain the directivity patterns in Figure 5.4-4 and Figure 5.4-5. When we add the conducting blocks there is negligible change to the patterns in the cut shown in Figure 5.4-4. There are slight changes to the pattern cut of Figure 5.4-5. These changes are shown in Figure 5.4-6 for three slightly different block sizes; they are noticeable but not significant. We can take this opportunity to compare our predicted patterns in Figure 5.4-4 to the measured patterns of the same antenna shown in Figures 5.4-7 and 5.4-8; these are taken[25] from [4]. The similarity of the directivity patterns (and their dBi levels) is encouraging[26]. We observe that the best agreement between predicted and measured patterns is not always between patterns at the same frequency. This frequency shift in the measured performance compared to the designed performance has been observed by others.

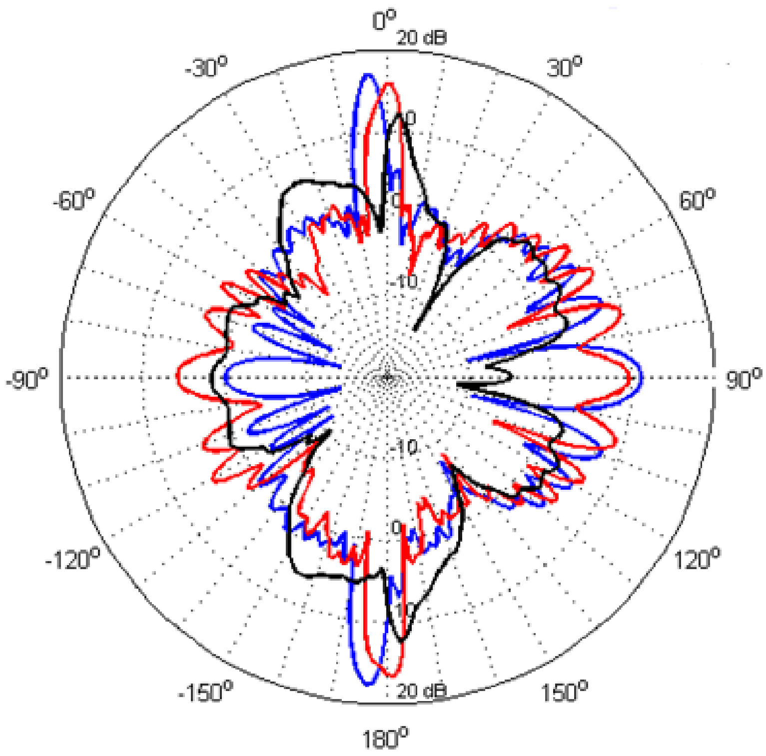

Figure 5.4-4 : Predicted directivity pattern (dBi) in the H-plane, with $\phi = 90^\circ$ at 29 GHz(——), 30 GHz (——) and 31 GHz (——)

---

[25] The predicted and measure polar plots have the same orientation, even though the numerical values of the angles shown are different. Unfortunately the raw numerical data was not available.

[26] Including the beam squint as the frequency changes.

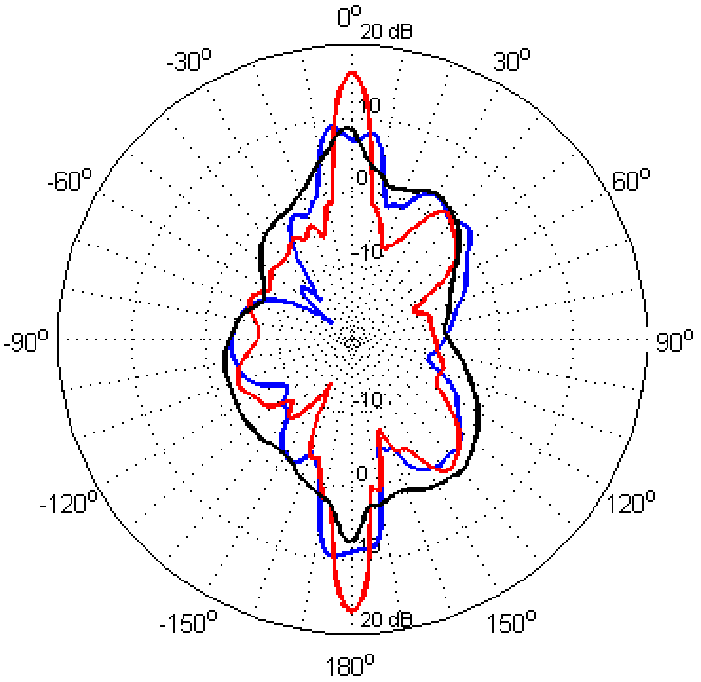

Figure 5.4-5 : Predicted directivity pattern (dBi) in the H-plane, with $\phi = 0^\circ$ at 29 GHz(——), 30 GHz (——) and 31 GHz (——)

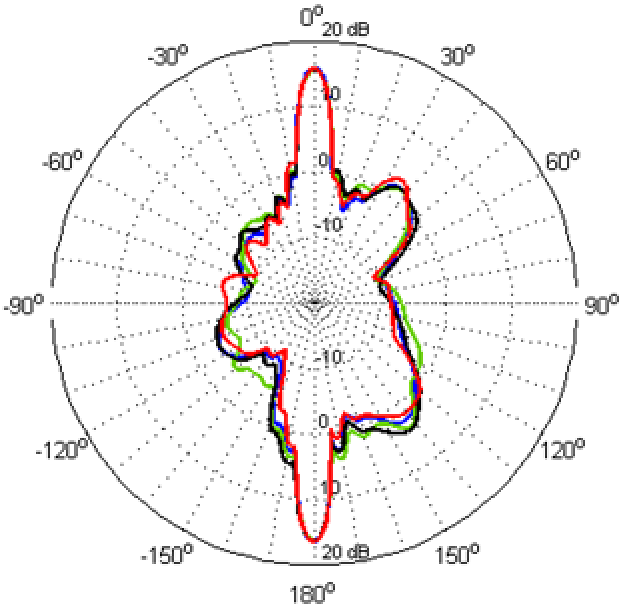

Figure 5.4-6 : Predicted directivity pattern (dBi) in the H-plane at 30 GHz , with $\phi = 0^\circ$, for various conducting block sizes.

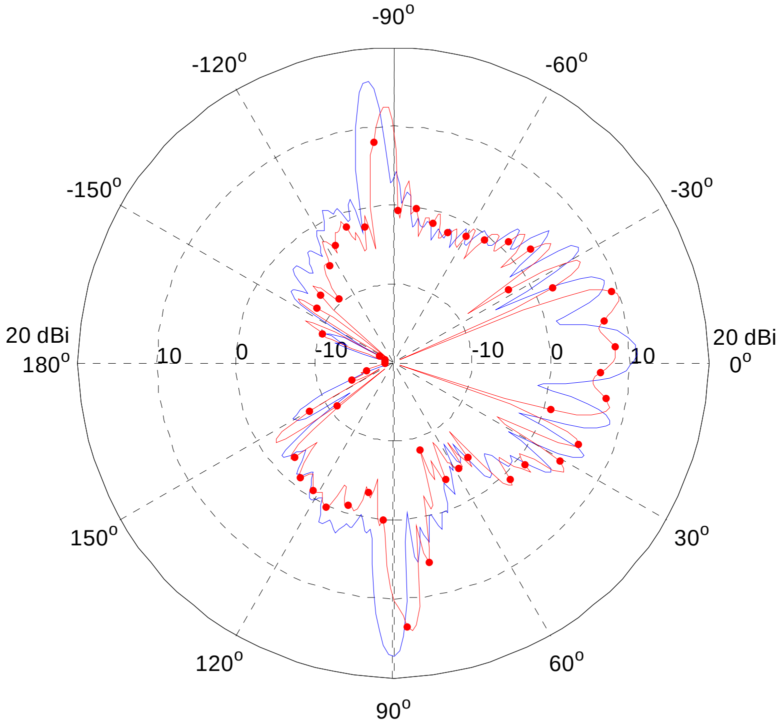

Figure 5.4-7 : Measured gain at 28.3 GHz (—) and 29.5 GHz (—) (After [4])

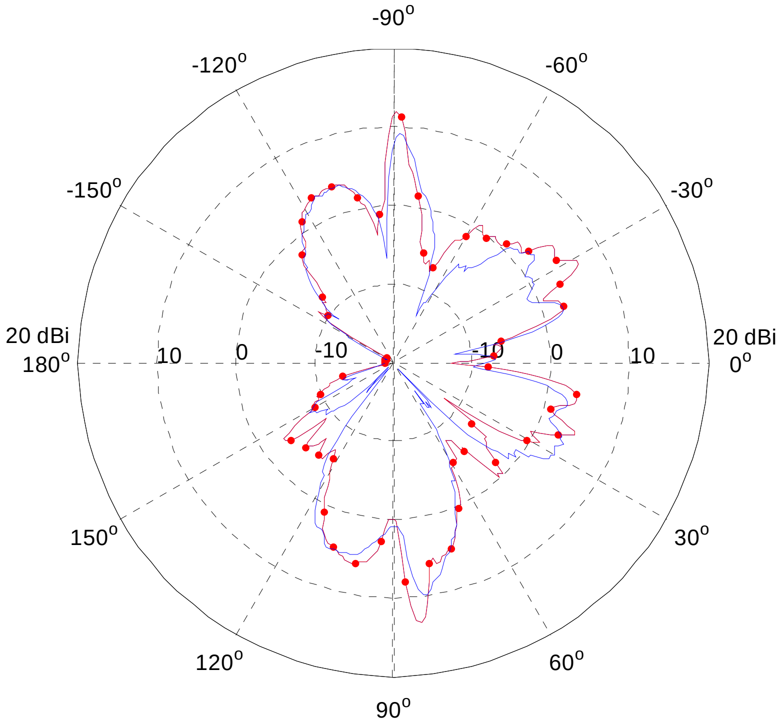

Figure 5.4-8 : Measured gain at 31 GHz (—) and 30 GHz (—) (After [4])

5.5 RECEIVE MODE ANALYSIS

5.5.1 The Receive Mode Analysis Idea

It is known that with conventional paraboloidal reflector antennas there are situations when maximum directivity is achieved with the feed displaced from the expected geometrical focal point, either slightly toward or away from the reflector [5]. This apparent shift of the true focal point is informatively revealed by considering the reflector in a receive-mode analysis. A plane wave is considered incident on the reflector along its axis, and the scattered field is computed as a function of position on the reflector axis [5]. A knowledge of the true location of the focal point provides information on where the feed should be positioned [6,7,8,9,10]. Similar work has been done for lens antennas [11] and reflectarray antennas [12].

We noted in Chapter 2 that the basis of holography is the recording of the interference pattern between the wave fields of two sources, and that the one wave field can be obtained (at least in principle) by illuminating some form of recording of the interference pattern with the other wave field. Throughout the thesis thus far we have considered the holographic antenna to be operating in the transmit mode, with the horn or Yagi feed acting as the source of the wave field that illuminates the hologram. In this section we will instead consider the operation of the holographic antenna in the receive mode. The EMPIRE model described in Section 5.4 and illustrated in Figure 5.4-1, was altered by removing the Yagi antenna completely. All that remains is the substrate and the single layer of continuous conducting strips. This is shown in Figure 5.5-1.

5.5.2 Receive Mode Fields of a Planar Holographic Antenna

Figure 5.5-2 plots various parts of the electric field along the line AA'. The incident wave is a plane wave with a magnitude of 1 as shown. The FDTD simulation outputs the total field, as shown. The effect of the conductor strips can easily be seen as the magnitude of the total electric field is driven to zero at the location of each conducting ring. It is also interesting to observe that there are discontinuities in the total electric field E_x^{total} in the vicinity of $x = \pm 0.03m$. This is physically correct, since these points are at the edge of the finite thickness substrate, and so E_x^{total} is normal to the dielectric-air interface there. The physical boundary conditions require that it be discontinuous there. The subtraction of the incident field from the total field provides the field scattered by the hologram structure, namely

$$E_x^{scat} = E_x^{total} - E_x^{inc} \tag{5.5-1}$$

which is also plotted in Figure 5.5-2. Observe that the total electric field E_x^{total} has its maximum at the point $(x = 0, y = 0)$. This is where we expect it to be, and it can be viewed as a "focal point" of the holographic antenna. However, depending on the type of feed used, it is the location of the maximum of E_x^{scat} that might be most important. In such a case the "focal point" can then be interpreted as being shifted away from the hologram strips along line AA'. The fact that the maximum is indeed at a point can be deduced from the fact the plot along line BB' also peaks at $(x = 0, y = 0)$.

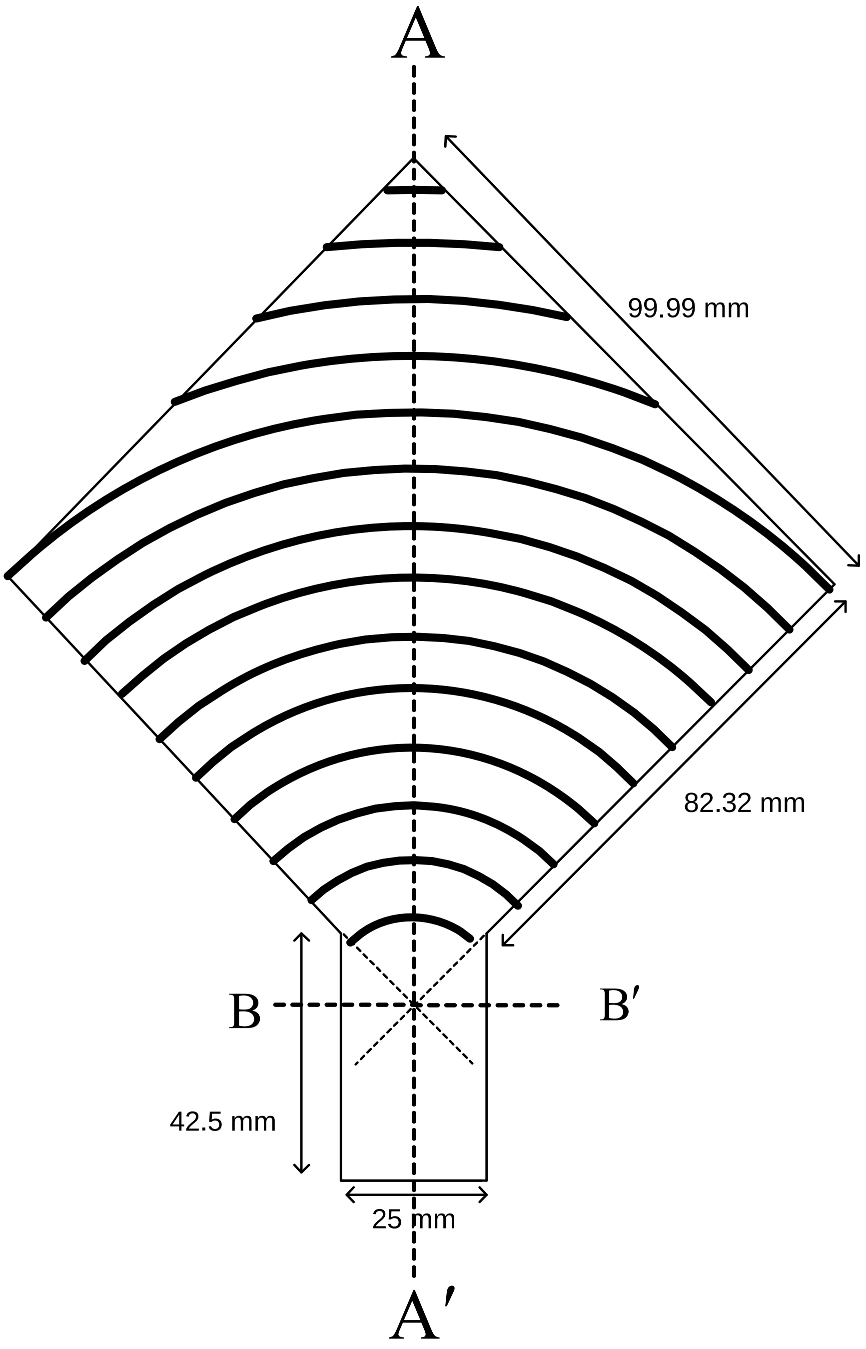

Figure 5.5-1 : Holographic antenna model for receive mode analysis.

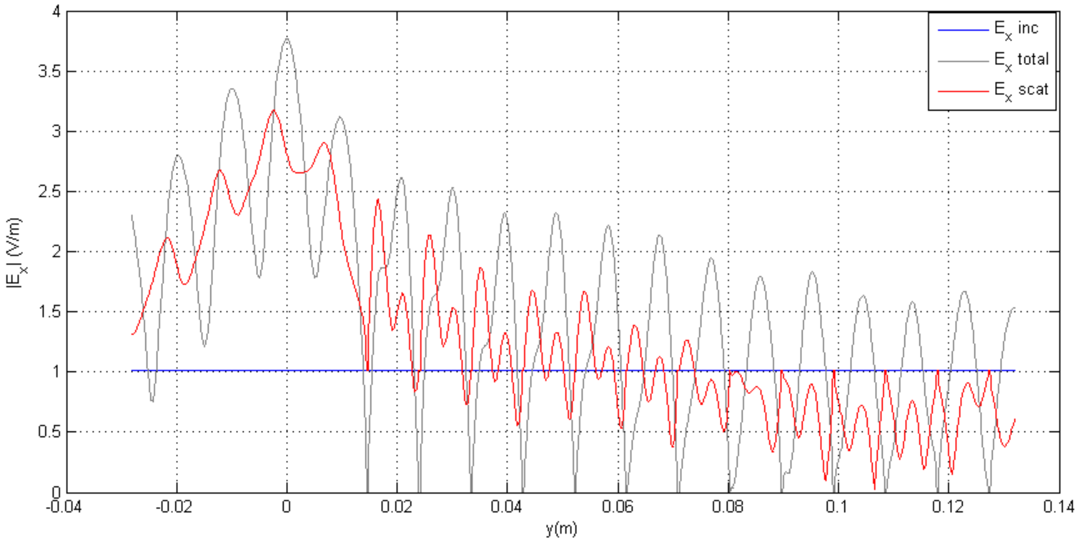

Figure 5.5-2 : Plot of the near-field E_x along line AA'. This was done using the "medium resolution mesh (15/4)" in EMPIRE.

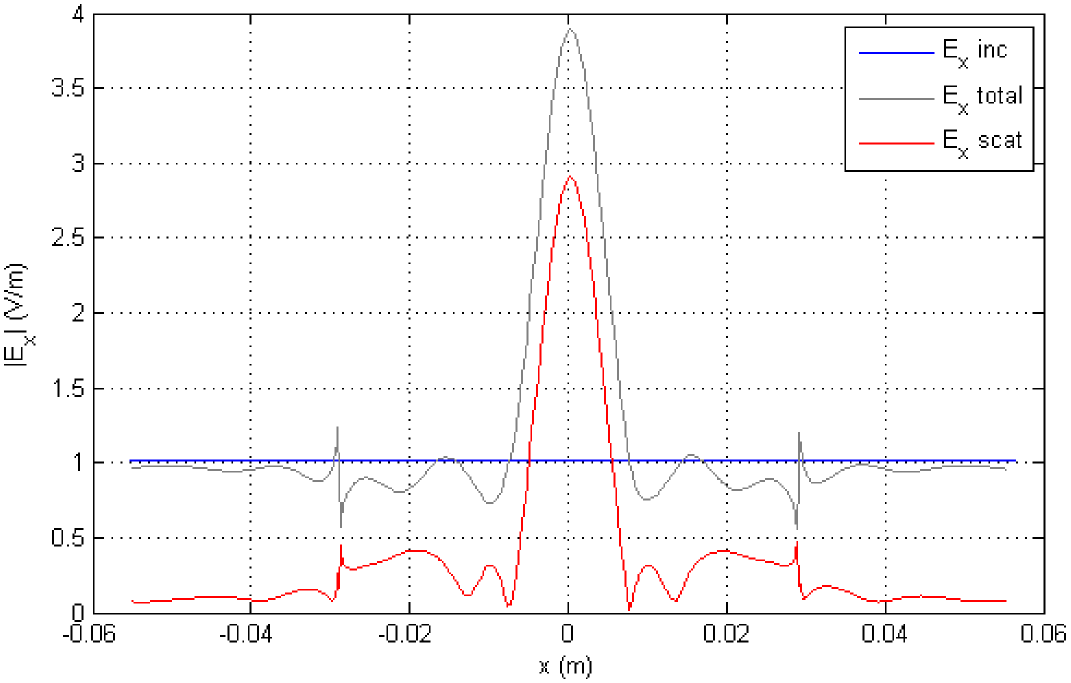

Figure 5.5-3 : Plot of the near-field E_x along line BB'. This was done using the "medium resolution mesh (15/4)" in EMPIRE.

5.6 CONCLUSIONS

Comprehensive computational electromagnetics modelling of planar holographic antennas has been done here for the first time. We have been able to observe and confirm several aspects of holographic antenna behaviour. It has been shown that spillover is indeed a major contributor to the low aperture efficiency of current holographic antennas. We have found that by shifting the feed location with respect to the hologram the directivity can be improved by up to 1dB. Through use of the proper null locations the broadside beam shape can be made more symmetrical, although there is little change in maximum directivity. However, even the predicted behaviour shows that the best performance often occurs at a frequency different from the nominal centre frequency at which the "paper design" based on basic holographic ideas was performed. This is where an ability to perform numerical optimisation using computational electromagnetics models we have used would provide a great design advantage. We believe increased computer resources, proverbially becoming more accessible, will likely make such optimisation feasible in the future.

5.7 REFERENCES FOR CHAPTER 5

[1] G. Saxby, *Manual of Practical Holography* (Focal Press, 1991).

[2] S.R. Thingvold, A. Ittipiboon, A. Sebak, and A. Petosa, “Holographic antenna efficiency”, IEEE Int. Antennas Propagat. Symp. Digest, Vol.3, pp. 721 – 724, July 2003.

[3] K.Lévis, A.Ittipiboon, A.Petosa, L.Roy and P.Berini, "Ka-band dipole holographic antennas", *IEE Proc., Microw. Antennas Propagat.,* Vol.148, No.2, pp. 129-132, April 2001.

[4] T.Quach, “Holographic Antennas Realized from Interference Patterns Determined in the Presence of the Dielectric Substrate”, *M.A.Sc Thesis*, University of Ottawa, Ottawa, ON, Canada, 2005.

[5] D.Midgley, "A theory of receiving aerials applied to the reradiation of an electromagnetic horn", IEE Proc., pp.645-650, Nov.1961.

[6] A.W.Rudge, "Focal-plane field distribution of parabolic reflectors", Electron. Lett., Vol.5, No.21, pp.510-512, Oct.1969.

[7] A.W.Rudge and M.J.Withers, "Design of flared-horn primary feeds from parabolic reflector antennas", Proc. IEE, Vol.117, No.9, pp.1741-1749, Sept.1970.

[8] W.M.Truman and C.A.Balanis, "Optimum design of horn feeds for reflector antennas", IEEE Trans. Antennas Propagat., pp.585-586, July 1974.

[9] H.Ling, S.W.Lee, P.T.C.Lam & W.V.T.Rusch, “Focal shifts in parabolic antennas”, IEEE Trans. Antennas Propagat., Vol.33, pp.744-748, July 1985.

[10] T.S.M.MaClean, *Principles of Antennas : Wire and Aperture* (Cambridge University Press, 1986).

[11] K.K.Chan, M.Gimersky and R.Pokuls, "Focal plane beam synthesis method for dielectric lens antennas", IEEE Int. AP-S Symp. Digest, pp.836-839, Montreal, Canada, July 1997.

[12] F.Arpin, D.A.McNamara, J.Shaker and A.Ittipiboon, “A Receive-Mode Analysis of Reflectarray Antennas”, Proc. 10th Int. Symp. Antenna Technology & Applied Electromagnetics (ANTEM′2004), pp.569-572, Ottawa, Canada, July 2004.

CHAPTER 6

General Conclusions

The principal contributions of this thesis are:

- The demonstration that it is not possible to remove the unwanted grating lobes from the planar holographic antenna at the fundamental level.
- The comprehensive computational electromagnetics modelling of planar holographic antennas for the first time. A discussion of the problems (and for some of these, their solutions) associated with such rigorous electromagnetic modelling.
- A demonstration that much of the loss in directivity of the planar holographic antenna is due to spillover of the feed radiation past the hologram in the H-plane.
- An examination, using numerical experimentation, of ways that could be used to "tweak" the directivity performance of planar holographic antennas.
- An exposition of the fact that, for a given configuration (that is, feed-type/hologram-type combination) there is an optimum feed location with respect to the hologram that provides maximum directivity. The best directivity is usually no more than about 1dB better than the sub-optimum.
- A receive mode analysis of the planar holographic antenna has been done for the first time, and a "focal point" has been shown to exist.

There remain some issues whose investigation in the future would prove useful. Firstly, although we have used the commercial codes FEKO (based on the method of moments) and EMPIRE (based on the FDTD method) to their limits, it might be fruitful to use the commercial code HFSS (based on the finite element method) as a modelling tool for this antenna. All these codes have upgraded versions for use on multi- and parallel-processor computers, and these should be used in the analysis of holographic antenna since even the smallest of these antennas are quite large (electrically speaking) geometries. Nevertheless, the fundamental issues of the grating lobes remain, and further optimization might only provide improved partial fixes to this problem. The devising of a printed feed that can ensure much lower spillover would allow holographic antenna performance to be greatly improved.